ASSEMBLY AND PROPERTIES OF 2D MATERIAL-MOLECULE SUPERLATTICES

Duncan Peterson

A dissertation submitted to the faculty at the University of North Carolina at Chapel Hill in partial fulfillment of the requirements for the degree of Doctor of Philosophy in the Department of Chemistry.

Chapel Hill
2025

Approved by:

Scott Warren

Megan Jackson

James Cahoon

Daphne Klotsa

Orlando Coronell

© 2025
Duncan Peterson
ALL RIGHTS RESERVED

ABSTRACT

Duncan Peterson: Assembly and Properties of 2D Material-Molecule Superlattices
(Under the direction of Scott C. Warren)

The fabrication of atomically precise hybrid materials is one of the core goals of materials science. By carefully combining different material building blocks, specific properties can be targeted for a variety of chemical, electronic, or physical uses. Layered and 2D materials are a particularly interesting class of building block, as they exhibit many interesting quantum properties when they are exfoliated into individual monolayers. However, unlike quantum dots, there does not exist a good way to assemble individual 2D monolayers into 3D solids, thus making their practical use in devices quite difficult. In this work, I demonstrate a generalizable method to assemble 3D solids from 2D semiconductors and molecules. By using a combination of simulation and experimentation, I propose a mechanism, and show the fabrication of a variety of molecule containing thin films, including novel structures predicted by our mechanism. After fabricating these novel superlattices, I perform a variety of characterization to show that the resulting superlattices maintain the interesting quantum properties of the 2D material, while still assembling into a 3D solid.

After characterizing the 2D material component of the lattice, I perform a combination of MD simulations and experimentation to reveal the increased dynamic potential offered to this material by the molecular phase. Our simulations reveal that the liquid phase trapped inside of the superlattice is quite mobile; in some cases more so than a bulk liquid. I show that this increased mobility is a direct result of decreased intermolecular forces, and in that way present

the beginnings of a model for intelligently designing novel hybrid materials. After demonstrating the increased mobility from a standpoint of simulation, I next utilize this increased dynamic potential to intercalate ions into the system in mild, aqueous conditions. I demonstrate that the intercalation is unique to the superlattice system, and further show that the superlattice system can be leveraged to intercalate ions that typically do not intercalate. By demonstrating the increased dynamic potential of our superlattice system, this work provides exciting opportunities to develop new hybrid materials for a variety of interesting optical, electrochemical, and physical purposes.

To all my friends, all of you truly made graduate school special and you're the best friends I could have asked for.

ACKNOWLEDGEMENTS

First and foremost, I would like to thank my advisor Scott Warren for his mentorship and support over the course of my PhD. He has helped me to improve my scientific and critical thinking skills to beyond what I ever thought possible. He was a wonderful mentor and really made my graduate school experience special.

I would also like to thank the members of the Warren lab. Beyond the scientific discussions we've had and the wonderful input you have had on my project, you have also all been such good friends. You made Chapel Hill a fun place to be for the past five years, and the importance of that cannot be understated. Special thanks to my cohort, Connor, Karen and Becca, you were my friends since the start of COVID (even when we weren't supposed to see other people), and it's always a pleasure to see you around or outside of lab. Additionally, I would like to thank the multiple undergraduates who put so much work into this project. Sydney, Andrew, Jackson and Lindsey, you all helped me to improve as a mentor and always challenged my understanding of the chemistry, and I see a bright future ahead for all of you no matter where you end up.

Finally, I would like to thank my family and my friends from outside of the Warren Lab. No matter how I met you, you helped to make UNC a much more entertaining place and I probably would have gone crazy without all of your support. Whether we would talk sports, play chess, or just hang out at the bars, I always appreciated having non-chemistry interactions. You all mean the world to me, and I hope to stay in touch as friends and colleagues.

TABLE OF CONTENTS

LIST OF TABLES…….. xiii

LIST OF FIGURES……. xiv

LIST OF ABBREVIATIONS…….. xvi

CHAPTER 1: INTRODUCTION…… 1

1.1 Uses and applications of 2D nanomaterials……...……... 1

1.2 Strategies to assemble 2D material structures from exfoliated materials…….. 2

1.3 Strategies to assemble hybrid structures from 2D materials and guest species……..4

1.3.1 Understanding the surface functionalization of layered materials……..6

1.3.2 Intercalation of layered materials……. 7

1.3.3 Other methods for assembling superlattices……..... 9

1.4 Outstanding questions ……. 11

1.5 Research overview …….. 14

References …… 15

CHAPTER 2: MATERIALS AND METHODS…… 21

Introduction …….. 21

2.1 Chemical exfoliation of MoS_2…….……. 21

2.1.1 Generation of a metallic (1T) monolayer solution…….…….. 22

2.1.2 Conversion from the metallic (1T) to semiconducting (2H) phase……... 27

2.1.3 Annealing procedure to generate solutions of 2H monolayers…….. 28

2.1.4 Analysis of solvent and annealing parameters…….……. 29

2.2 Assembly of ordered superlattices from a solution of monolayers…….. 32

2.2.1 Vacuum filtration for the assembly of thin films…….. 33

2.2.2 Doctor blading of superlattices……. 34

2.2.3 Langmuir–Blodgett (LB) interfacial assembly……. 35

2.2.4 Characterization techniques…….. 37

2.3 Electrochemical intercalation of the superlattice……. 41

2.4 Molecular dynamics simulations of the superlattice system……..... 42

2.4.1 MD simulation parameters…… 43

2.4.2 Simulation box setup……. 45

2.4.3 Simulations to calculate potential energy surfaces…… 46

2.4.4 Simulations to calculate diffusion coefficients……. 47

2.4.5 Simulations to calculate solvation energies…….. 49

References……. 54

CHAPTER 3: ASSEMBLY, MECHANISTIC INVESTIGATION, AND PROPERTIES OF 2D MATERIAL-MOLECULE SUPERLATTICES……... 57

Introduction……... 57

3.1 Simulations of MoS_2 aggregation in liquid……..…… 60

3.1.1 Joining the free energy surfaces…… 65

3.2 Experimental assembly of a semiconducting superlattice…… 71

3.3 Generalizability of molecule-semiconductor superlattices…….. 78

3.4 Quantum-confined but electrically conductive superlattices……... 82

Conclusions and outlook……..... 86

Reference……...95

CHAPTER 4: CHARACTERISTICS AND PROPERTIES OF 2 DIMENSIONALLY CONFINED LIQUIDS……. 96

Introduction……..... 96

4.1 Understanding 2D confined diffusion…….. 97

4.1.1 Solid-liquid phase transitions in confined systems……..... 98

4.2 Understanding the confinement in the superlattice system……. 100

4.2.1 Two case studies demonstrating different types of confined diffusion..... 101

4.2.2 Solvation energies of DMPU and resorcinol……... 105

4.3 Shape effects on confined liquids……... 109

Conclusions and Outlook……. 110

References……... 112

CHAPTER 5: SUPERLATTICE AS ION STORAGE DEVICES AND MEMBRANES……. 115

Introduction……..... 115

5.1 Aqueous batteries…….. 115

5.2 Electrochemical intercalation of the superlattice……... 119

Conclusions and Outlook……. 126

References……... 128

APPENDIX 1: SUPPORTING INFORMATION FOR CHAPTER 2 ……..…….. 129

APPENDIX 2: SUPPORTING INFORMATION FOR CHAPTER 4 ……..…….. 132

APPENDIX 3: SUPPORTING INFORMATION FOR CHAPTER 5……...…….. 135

LIST OF TABLES

Table 3.1 Quant table of superlattice XPS ……..……. 80

Table 4.1 Solvation energies of DMPU and resorcinol ……. 105

LIST OF FIGURES

Figure 1.1: Generic structure of confined but conductive material …… 6

Figure 2.1: Generic structure of confined but conductive material ……. 33

Figure 2.2: Ruby calibration spectrum for DAC pressure ……... 41

Figure 2.3: Convergence of solvation energies based on different packing densities ……. 53

Figure 3.1: Setup and potential energy surfaces of MoS_2 in NMP ..…… 64

Figure 3.2: Solvent density plot of NMP between MoS_2 layers …….. 65

Figure 3.3 Simulation setup for PMF calculation …… 66

Figure 3.4 Schematic of how the potential energy surfaces were joined ……. 67

Figure 3.5 Decoupling approach explained …….. 70

Figure 3.6 Potential energy surface of MoS_2 in DMPU …… 71

Figure 3.7 Structural analysis of MoS_2-molecule superlattice ……. 74

Figure 3.8 TEM of semiconducting monolayers ……. 76

Figure 3.9 Cross-sectional TEM of MoS_2-PEG superlattice ……... 77

Figure 3.10 UV-Vis spectrum of superlattice …….. 78

Figure 3.11 Simulation of DMPU-MoS_2 superlattice …….. 79

Figure 3.12 Angle distribution of molecules in the superlattice …….. 80

Figure 3.13 Generalizability of superlattice assembly ……. 81

Figure 3.14 Diffraction patterns of the superlattice ……. 82

Figure 3.15 XPS of a fluorine containing superlattice ……. 83

Figure 3.16 Quantum confined and electrical properties of the superlattice …….…….. 85

Figure 4.1 Schematic of bulk vs 2D melting …….….. 99

Figure 4.2 Structures of DMPU and resorcinol ……. 101

Figure 4.3 Arrhenius plot of DMPU diffusion ……..…….. 103

Figure 4.4 Arrhenius plot of resorcinol diffusion …….. 105

Figure 4.5 Crystal structures of DMPU and resorcinol ……. 108

Figure 5.1 LSV of NMP superlattice in $NaHSO_4$…….…….. 120

Figure 5.2 LSV comparisons between SO_4 and PO_4 systems …… 121

Figure 5.3 LSV and CP of PO_4 system …….. 122

Figure 5.4 Cation dependence of intercalation features ……. 123

Figure 5.5 CV of PO_4 system ……. 124

Figure 5.6 pH dependence of intercalation …… 124

Figure A1.1 XPS of unannealed MoS_2 ……... 129

Figure A1.2 XPS of annealed MoS_2 …….. 130

Figure A2.1 Screenshot of simulation showing 2D resorcinol …….. 131

Figure A2.2 Diffusion plots of increasingly bulky benzene derivatives …….…….. 132

Figure A3.1 P 2p XPS spectra of intercalated and unintercalated films …… 134

Figure A3.2 S 2s XPS spectra of intercalated and unintercalated films ……..... 135

LIST OF ABBREVIATIONS

LAMMPS = Large-scale Atomic/Molecular Massively Parallel Simulator

MD = Molecular Dynamics

TMDC = Transition Metal Dichalcogenide

NMP = N-methylpyrrolidone

DMPU = N,N'-Dimethylpropyleneurea

PC = Propylene Carbonate

n-buLi = n-Butyl Lithium (1.6M in hexanes unless stated otherwise)

Py-Li = Pyrene Lithium

LB = Langmuir-Blodgett

PMF = Potential of Mean Force

FEP = Free Energy Perturbation

WHAM = Weighted Histogram Analysis Method

MSD = Mean Squared Displacement

FEP = Free Energy Perturbation

LSV = Linear Sweep Voltametry

CP = Chronopotentiometry

CHAPTER ONE – INTRODUCTION

1.1: Uses and applications of 2D nanomaterials

Layered and 2D materials are a relatively new class of nanomaterials that encompass a wide variety of chemistries and structures. Since the isolation of monolayer graphene in 2004[1], these materials have been of particular interest because of the combination of high mechanical strength and interesting optical and electronic properties that are unique to the monolayer form. Like quantum dots, these unique optical and electronic properties are due to quantum confinement of the nanosheets[1–3]. Due to the effects of quantum confinement, materials of identical compositions can have radically different properties solely based on the size of the particle. For example, CdSe quantum dots can be tuned to emit across the entire visible spectrum simply by changing the size of the dot[4,5]. This has led to their incorporation into modern electronic devices, such as many displays and LEDs. Layered and 2D materials also become quantum confined as they are exfoliated from the bulk crystal down to a single monolayer, although the confinement geometry is planar rather than a single point.

While the origin of the interesting optical and electronic effects is the same, the specific properties of each 2D material system vary greatly depending on the chemical composition of the components. This great variety is one of the unique advantages of 2D material systems, as it is possible to select from a wide range of properties for a specific application. For example, monolayer graphene has an exceptionally high carrier mobility of 100,000 $cm^2\ V^{-1}\ s^{-1}$ while also having no band gap[6]. This leads to the observation of ballistic conduction over micron scale distances, as a relatively defect free monolayer is easily able to conduct carriers over the entirety

of its area. In addition to its interesting electronic properties, when it was first measured in 2008, the mechanical properties of monolayer graphene made it the strongest material ever discovered with a tensile strength of 130 GPa; more than 100 times greater than most types of steel[7]. This combination of high electrical conductivity and incredible mechanical strength has led to the incorporation of graphene into a variety of modern devices, particularly battery electrodes.

Interestingly, isoelectronic monolayer hexagonal boron nitride has nearly opposite properties, where the monolayer material has a bandgap of 6 eV due to the strong covalent nature of the B–N bonds[8,9]. This, combined with the high mechanical strength[10] and low reactivity[11], makes hexagonal boron nitride an ideal protective component in many electronics. Owing to their nearly identical structure but divergent electronic properties, graphene and hexagonal boron nitride heterostructures are good matches for developing complex electronics. In some reports, CVD grown graphene has reported carrier mobilities on the centimeter scale of 5,000 $cm^2\ V^{-1}\ s^{-1}$ [12]. In contrast, graphene and hexagonal boron nitride heterostructures report exceedingly high carrier mobilities of 500,000 $cm^2\ V^{-1}\ s^{-1}$ [6], 2 orders of magnitude greater than that of pristine graphene.

In addition to metallic and insulating 2D materials, other materials, such as many transition metal dichalcogenides (TMDCs) and black phosphorous, are semiconductors with complex, thickness dependent behavior. For example, the bandgap of black phosphorous increases from 0.3 to 1.8 eV when it is exfoliated from a bulk crystal to an individual monolayer[13,14]. Other materials, such as MoS_2, are in the bulk form an indirect bandgap semiconductor (bandgap = 1.2 eV), which transitions to a direct bandgap semiconductor (bandgap = 1.8 eV) when isolated as a monolayer[15]. This results in thickness dependent photoluminescence where the monolayer photoluminesces strongly and bilayer and thicker crystals do not[3,15]. This gives these materials great tunability even when the devices are composed of just one type of material, which makes them ideal for many

upscaling applications where only one type of processing is needed to make a variety of different devices.

1.2: Strategies to assemble 2D material structures from exfoliated materials

Despite the great variety in properties of 2D materials, similar assembly methods work with different types of materials as the underlying geometry is quite similar; independent layers held together by Van der Waals interactions. Bottom up synthetic methods, such as chemical vapor deposition (CVD), are some of the primary methods to assemble devices out of 2D materials. By using CVD, almost any combination of 2D materials can be grown with extremely high precision in terms of area and thickness. In addition to the ability to grow pristine monolayers of a single material, CVD can also be used to grow heterostructures, where one type of 2D material is grown on top of or in direct contact with another. One of the main advantages of CVD grown 2D heterostructures is the ability to form atomically sharp interfaces without dangling bonds or many surface defects. This has led to a great variety of interesting materials, such as MoS_2/WS_2 lattices, which are natural type II semiconductors due to the mismatch in band structure between MoS_2 and WS_2[16]. Additionally, due to the atomically sharp interfaces, these heterostructures are also interesting for basic research purposes, as a variety of physical phenomena can be studied under highly controlled conditions. In one study, a topological field effect transistor composed of hexagonal boron nitride and WTe_2 was proposed, where the conductivity of the transistor could be shut off by the application of even minimal strain to the device[17].

However, CVD can only be performed with certain setups, which limits the general use of this technique. The fact that 2D materials can naturally be found as bulk crystals, however, makes them amenable to both top down and bottom up synthetic strategies. One such top down method is mechanical exfoliation and subsequent restacking of the exfoliated materials. This process has

been extensively demonstrated by the Nobel prize winning scotch tape exfoliation method. By using scotch tape to mechanically peel apart graphite, Geim and Novoselov first isolated monolayer graphene in 2004[1]. Since then, mechanical exfoliation and layer by layer assembly have been used to develop a variety of devices, such as the previously mentioned highly conductive graphene/hexagonal boron nitride structure[6]. In contrast to CVD based methods, these mechanical exfoliation methods are quite accessible and straightforward to perform without a specialized set up. More advanced mechanical exfoliation methods rely on using an interface, such as gold or a polymer, to increase both the area and yield of the exfoliated monolayers[18,19].

With the emergence of tools for micromanipulation and restacking 2D materials, it has become possible to carefully restack mechanically exfoliated materials. This has led to studies where control over the twisting angle and orientation of layers is used to tune the electronic properties of the resulting material. For example, studies show that the bandgap and photoluminescence of a MoS_2 bilayer could be controlled by varying the twist angle of the two layers, as twisting the layers relative to each other caused a lattice mismatch which changed the ability of the two monolayers to electronically couple[20,21]. Other studies have used micromanipulation tools to generate heterostructures of 2D materials and 2D polymers via highly controlled mechanical stacking[22,23]. In recent work from Park et al., it was found that different porphyrins could be stacked with MoS_2 to generate heterostructures with carefully tuned transmission profiles and interesting capacitive behavior. However, these methods are labor intensive and often are not amenable to scaling or generalization; layer-by-layer assembly is time consuming, and only certain molecules can be manipulated and stacked in a controlled way.

In addition to mechanical layer-by-layer assembly, the other main type of top-down assembly method is a strategy involving liquid exfoliation and ultrasonication to generate a

suspension of 2D semiconductors. This method was popularized by Coleman, who sonicated a variety of 2D materials in highly polar organic solvents and generated suspensions of few-layer 2D materials[24–26]. This solution processing method has the distinct advantage of yielding solutions of 2D materials, which are far easier to process on a large scale than mechanically exfoliated monolayers. While CVD and mechanical methods are typically performed on the monolayer scale, liquid exfoliation is scalable to at least the 100 gram scale. This method has been used to prepare free-standing, centimeter-scale films of both pure 2D materials and heterostructures via vacuum filtration and 3D printing[24,27]. However, these methods of sonication-based liquid exfoliation are imprecise and tend to provide a distribution of thicknesses, making the development of atomically precise materials difficult. Additionally, the actual monolayer yield of these exfoliation methods can be quite low, which means that many properties unique to monolayers cannot be realized in devices assembled from these solutions.

However, the ability to generate solutions of 2D materials still unlocks a large variety of solution processing methods to assemble solids. In addition to the vacuum filtration method, spin and spray coating methods have been used to produce wafer-scale graphene films. These films have been demonstrated to transmit 95% of the light in the visible region while maintaining conductivities as high as 0.45 S/cm[28]. The Langmuir–Blodgett (LB) technique, which involves assembly at the air–water interface, has improved upon spin-coating methods to generate graphene films that are an order of magnitude more conductive while transmitting 90% of visible light[29]. In addition to the advantages in scalability that solution processing provides, working with these materials in solution also offers opportunities to use the well-studied methods of assembling quantum dot solids. These techniques are therefore the best chance to generate a 3D structure which is composed of quantum-confined components.

1.3: Strategies to assemble hybrid structures from 2D materials and guest species

Similar to quantum dot solids, one of the main challenges of assembling 2D monolayers into solid-state assemblies is preserving the quantum confined properties. Quantum confinement in quantum dot solids is typically achieved via ligand functionalizing solutions of quantum dots, where nonconductive ligands on the surface of the dots are used to separate individual dots from neighbors[30,31]. This results in solids where the individual dots are close enough to electronically communicate but far enough apart that they remain quantum confined. The analogous structure for 2D materials is a guest-host structure where host 2D monolayers are separated by a guest species such that the monolayers are far enough apart that they remain quantum confined (Fig. 1). Except for the example with porphyrins, bottom-up and mechanical assembly methods do not incorporate other species in addition to 2D materials into an ordered lattice. This means that the great variety of molecular chemistries are not accessible via these highly controlled assembly methods. Therefore, many different top-down strategies have emerged to process 2D materials and guest species into devices, although this leads to different challenges in controlling the properties of the resulting material.

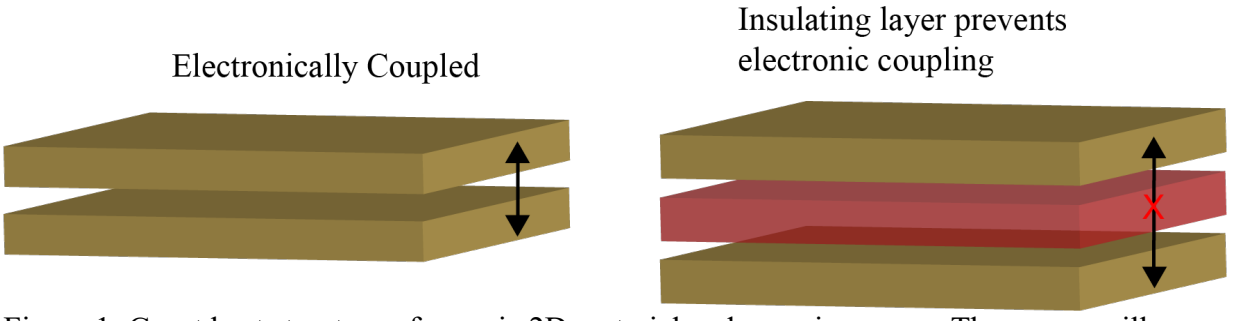


Figure 1: Guest host structure of generic 2D material and generic spacer. The spacer will ideally be an insulator with a large enough radius to precent electronic coupling between the 2D material layers.

The specific strategy of surface functionalization, which works well with quantum dots, does not work as well with 2D materials as the surface makes up a much greater fraction of the material than in quantum dot systems. Because of this, surface functionalizing 2D monolayers often results in a much greater change in the chemistry of the individual component. For example, when graphene is processed in water, the resulting graphene oxide is not a zero bandgap material but rather a semiconductor with much lower electrical conductivity[32,33]. Other 2D material systems also exhibit equally large changes, such as monolayer MoS_2, where the emergent photoluminescence is often quenched by surface functionalization due to changes in the electronic structure of the material[34,35].

1.3.1: Understanding the surface functionalization of layered materials

Surface functionalization, however, is not necessarily always detrimental to the properties of a 2D material system. In the example of graphene oxide, the properties of the pristine graphene monolayer are lost, but different properties are gained[32,33]. In addition to becoming a semiconductor, the -OH groups give it much greater dispersibility in water, which means that further processing and therefore scalability is much easier. The dangling -OH groups are also much easier to functionalize than a carbon surface, so specific functionalization for specialized applications is also more straightforward[36]. For example, graphene oxide functionalized with crosslinking carbon chains have been shown to have filtration efficiencies that are orders of magnitude higher and lifetimes that are up to 10 times longer than those of comparable unfunctionalized membranes[37].

Another example of surface functionalization being used to generate new and interesting materials is in the MXene systems. To generate the layered MXene structure, the A metal phase is typically etched away from a MAX structure (M = transition metal, A = group A element, X =

C or N), leaving behind an MX layer functionalized with some terminating group (e.g., -OH, -F, etc.)[38,39]. These surface groups are abundant and highly reactive, and further reactions with these groups have led to many interesting new materials. For example, Nb_2C with a variety of surface terminations are superconductors with critical temperatures of up to 7.1 K[40]. Additionally, changing the surface groups greatly changes the critical temperature, suggesting that the properties of bulk MXenes are impacted by the electronic structure of the surface groups. Other studies have shown that the bandgap of MXenes can be tailored by varying the surface functionalization, changing metals into semiconductors with bandgaps of up to 2 eV[41]. However, because the properties are heavily influenced by surface groups, capturing the properties of pristine monolayers is still an outstanding challenge.

1.3.2: Intercalation of layered materials

To generate lattices composed of pristine monolayers and spaced interlayer species, strategies that avoid surface functionalization must therefore be explored. One such strategy that has emerged to make ordered materials without surface functionalization is the intercalation of strongly interacting species, which typically generates lattices where each 2D layer is separated from its neighbor by an intercalant. In these strategies, the driving force behind the intercalation is a charge transfer reaction, where the intercalating species donates an electron and reduces the host 2D lattice.

These intercalation reactions have been leveraged in many interesting ways, perhaps most famously in the creation of the lithium-ion battery. Lithium intercalation reactions have been known since the 1970s, where lithium was electrochemically intercalated into TiS_2[42,43]. In the early 1980s, this intercalation was shown to be reversible when Goodenough and coworkers discovered a material capable of uptaking and releasing lithium at high potentials[44]. Graphite was

introduced as an anode material in the 1990s because of its high stability[45], leading to the creation of modern lithium-ion batteries, a ubiquitous way to store energy in electronic devices that now comprises a market share of ~65 billion dollars. In addition to the financial success of lithium based batteries, this technology has also generated many basic research opportunities to understand the processes of intercalation reactions which often involving understanding how the diffusion is impacted by the confined spaces of the electrodes.

In addition to the intercalation of lithium, other small molecules have also been intercalated into other layered materials, such as with the TMDCs TaS_2 and NbS_2, where the resulting metallic structures become superconductors at low temperatures[46–48]. These materials span a large range of chemistries and geometries, with interlayer expansions ranging from 4 Å to 60 Å depending on the chemical structure of the intercalant. Inorganic salts, long-chain amines, and small organic molecules were all found to intercalate and impart similar superconductivity despite the variety in interlayer spacing and dielectric constants, suggesting that the 2D material layer alone is responsible for the electronic properties. More modern work on the intercalation of ions has led to the development of many interesting materials that attempt to combine features from both intercalated ions and layered materials[49,50]. In 2022, chiral molecules were intercalated into TMDCs, and the resulting superlattices had high spin polarization ratios corresponding to the chirality of the intercalated ion[51]. This study highlights the potential of hybrid materials, where the interesting chemistry of the guest species can be used to generate new and interesting properties in the resulting superlattice.

Despite much of this earlier work on intercalation, two broad challenges for the design of superlattices exist. First, many chemically interesting molecules cannot be intercalated. Because intercalation into layered materials is driven by charge transfer, nearly always the intercalating

species is an ion[46,48]. Even in initial studies where it seemed that uncharged small molecules had intercalated, it was later revealed that the intercalation conditions (often >150 °C) caused decomposition reactions that yielded ammonium or phosphonium ions and that these or related ions were intercalated[52,53]. Indeed, when interesting properties such as superconductivity are observed, they are often a result of charge transfer doping via intercalated ions. The second broad challenge is that, across nearly all of the earlier work, intercalation causes the layered material to become metallic. This is noted, for example, in the widely studied conversion of MoS_2 from its 2H (semiconducting) to 1T (metallic) form upon intercalation of a metallic ion[42,54]. In general, when an ion intercalates, the layered material becomes highly reduced or oxidized, causing the semiconducting material to either become degenerately doped or metallic[55,56].

1.3.3: Other methods for assembling superlattices

To create a general strategy for incorporating molecules into a 2D material lattice, the first step is to break the van der Waals interactions holding the 2D materials together so that another species can sit in the interlayer. Typically, this is done in solution, such as with Coleman's liquid exfoliation method, although certain 2D materials can also be chemically exfoliated. By first intercalating lithium into a TMDC crystal such as MoS_2 or WS_2, it is possible to fully intercalate the lattice with lithium cations[42]. However, the lithium is still extremely reactive, and when the Li-TMDC powder is added to water, the lithium reacts and generates H_2 gas, which provides a driving force to separate the layers[57]. Because the lattice is fully intercalated with lithium, this chemical exfoliation method results in a high yield of single monolayers. These solutions provide a unique opportunity to work with true monolayers in a way that solutions produced by sonication do not.

In the 1980s, a simple and intriguing strategy for combining uncharged molecules with these monolayer solutions was discovered. It was found that 1T (metallic) MoS_2 monolayers could self-assemble with uncharged molecules at the oil–water interface, yielding periodic superlattices[58]. These superlattices have since been demonstrated with a small variety of molecules and similar 2D materials, such as WSe_2 and $MoSe_2$. However, these systems have not been widely studied, as the process used to generate these materials often results in the creation of metallic TMDC monolayers, which are much less interesting from a device perspective than a semiconductor. Additionally, assembly at an oil–water interface results in a much lower degree of control over the final structure than bottom-up synthetic methods or assembly on a vacuum filter.

The other method to incorporate molecules into a superlattice is via direct vacuum filtration. Using solutions of chemically exfoliated TMDCs, reports have shown that filtering saturated metallocene solutions over a film assembled on a vacuum filter results in the inclusion of the metallocene species in a TMDC superlattice[59]. This is most likely a result of the solution processing method, as chemical exfoliation yields highly polar monolayers that are hydrophilic and tend to trap water which stops the material from restacking. This is corroborated by studies show that hydrated 2D materials do not turn into bulk assemblies until they are dried, but upon drying, they irreversibly restack into bulk crystals[58]. While these materials are still wet, however, it is possible to replace the water trapped inside the lattice with a high boiling point molecule (such as a metallocene), which does not evaporate as the 2D materials dry.

However, the method of chemical exfoliation has a major limitation: the lithium intercalation reaction induces a phase transition where the TMDC converts from a semiconducting phase to a metallic phase. This is problematic, as many of the interesting properties are unique to

the semiconducting phase, and these processing methods have only been demonstrated with metallic species. The metallic phase is meta-stable, and therefore annealing at relatively low temperatures can restore the material to a semiconducting phase[3,60]. Previous work has demonstrated the successful phase restoration of the semiconducting phase, but these studies run into one of two problems when device fabrication is attempted. The first major problem is that solid-state annealing results in restacking and irreversible reversion of the material to a bulk crystal, so while semiconducting properties are improved, quantum confinement properties are lost[61]. The second major problem is that solution-based annealing methods simply have not worked because of the low dispersibility of the monolayers in appropriately high boiling solvents[60]. To increase dispersibility, surface functionalization strategies have been used, although this runs into the problem of surface reactions with 2D materials which greatly changes their properties. To date, no work has been able to generate stable solutions of high-quality, monolayer semiconductors.

1.4: Outstanding questions

When 2D monolayers are restacked into a solid film, many interesting properties are typically lost, and the resulting solids have properties similar to those of the bulk material. To counteract this problem and maintain the interesting quantum confinement properties of monolayers, it is necessary to spatially separate the layers, suggesting a superlattice structure where monolayers of 2D materials alternate with layers of other molecular or ionic interlayer species. However, there is not a good, general strategy to achieve this structure. Intercalating an interlayer species, due to the charge transfer between the intercalant and 2D material, leads to changes in the optical and electronic structure of the 2D monolayers, which means that metallic ions and charged species are not good interlayer targets. Directly bonding ligands to the surface

of 2D materials has a similar effect, where the interesting optical and electronic properties of a pristine monolayer are impacted by changes in surface chemistry. Therefore, the most promising method to achieve this guest host structure is without strong interactions, most likely via a self-assembly method that incorporates weakly interacting, uncharged molecules.

Because the most commercially successful systems of layered systems are intercalation materials, much of the prior research has been dedicated to understanding and developing those systems. The self-assembly procedure described by Morrison and coworkers is promising for the potential of a self-assembly technique, although the limitations of this method and the mechanisms of how 2D materials and molecules self-assemble are not well understood. Typically, self-assembly processes are entropically driven rather than enthalpically driven, which means that the specific chemical interactions required for intercalation reactions are not required for self-assembly. Additionally, the entropic driving force suggests that, by understanding the mechanisms of self-assembly procedures, many new types of chemistries can be combined into ordered solids. However, due to the lack of understanding of the specific mechanisms of self-assembly, it remains unclear whether this method is truly generalizable to any type of 2D material or guest species. As these systems have been demonstrated with only metallic 2D materials, it is also unclear whether the interesting optical and electronic properties of the semiconducting forms persist when these materials are assembled into the solid state. It is possible that one molecular layer (~3–4 Å) is not large enough to electronically decouple the monolayers or that more complicated effects involving electronic coupling to the molecular phase persist.

Additionally, this structure also leads to interesting questions about how the molecular phase trapped between the 2D monolayers will behave, as it will interact much more weakly than previously made intercalation compounds. In similar confined systems, such as water in carbon

nanotubes, confined water is observed to diffuse much faster than bulk water[62,63]. Liquids confined in 2 dimensions are much less studied, but it could be that this weakly interacting 2D liquid phase could have additional dynamic potential, certainly more than a strongly interacting or bonded interlayer species. In particular, these weakly interacting systems could have potential as ionic storage devices, where the dynamic properties of the interlayer can be exploited to achieve intercalation under previously impossible conditions.

1.5: Research overview

In this dissertation, I perform a combination of molecular dynamics (MD) simulations and experimentation to understand how superlattices assemble in solution **(Chapter 3)**. I generate a potential energy surface and demonstrate that the superlattice assembly process is not the product of unique chemical interactions and should therefore be generalizable to many different 2D material and molecule systems. I then use this generalizability to assemble superlattices from different 2D materials, molecules, and even stacking sequences (e.g., trapping a bilayer of molecules). Additionally, using the mechanism generated from the MD simulations, I propose a general strategy to assemble solutions of 2D materials and molecules into superlattice structures that contain alternating layers of molecules and 2D materials. Using MoS_2 as a model system, we performed a variety of characterization techniques to determine that, despite being assembled into a solid film, MoS_2 behaves as an electronically isolated monolayer. I found that the molecular layer is critical for maintaining quantum confinement in the bulk assembly and that removal of the molecular layer leads to the recovery of bulk MoS_2.

After I demonstrate the generalizability of the mechanism, I perform MD simulations to look at the physical properties of the confined liquid in the superlattice **(Chapter 4)**. From the MD data, I find that some liquids diffuse faster than bulk when confined in 2 dimensions between

the 2D material layers. To understand this observation, I then perform solvation energy calculations to relate these diffusion coefficients to molecular structures, and I find that faster diffusing molecules lose interactions when confined in 2 dimensions compared with the bulk liquid. Similarly, I find that molecules that diffuse slower under 2D confinement tend to have similar or stronger interactions than in the bulk.

Because the liquid phase is more mobile than typical intercalants, I then demonstrate that the molecular layer makes the superlattice material uniquely suited as a host for ion intercalation **(Chapter 5)**. Because the 2D liquid phase has a dynamic potential, I show that it is possible to intercalate ions into a superlattice when the bulk material is electrochemically inactive. Additionally, I demonstrate through electrochemical experiments that we are most likely intercalating a combination of cations and ions, and that the electrochemical process most likely damages the superlattice upon intercalation.

REFERENCES

(1) Novoselov, K. S.; Geim, A. K.; Morozov, S. V.; Jiang, D.; Zhang, Y.; Dubonos, S. V.; Grigorieva, I. V.; Firsov, A. A. Electric Field Effect in Atomically Thin Carbon Films. *Science* **2004**, *306* (5696), 666–669. DOI: 10.1126/science.1102896.

(2) Brus, L. Electronic Wave Functions in Semiconductor Clusters: Experiment and Theory. *J. Phys. Chem.* **1986**, *90* (12), 2555–2560. DOI: 10.1021/j100403a003.

(3) Eda, G.; Yamaguchi, H.; Voiry, D.; Fujita, T.; Chen, M.; Chhowalla, M. Photoluminescence from Chemically Exfoliated MoS2. *Nano Lett.* **2011**, *11* (12), 5111–5116. DOI: 10.1021/nl201874w.

(4) Hodes, G. Size-quantized Nanocrystalline Semiconductor Films. *Isr. J. Chem.* **1993**, *33* (1), 95–106. DOI: 10.1002/ijch.199300015.

(5) Rossetti, R.; Hull, R.; Gibson, J. M.; Brus, L. E. Excited Electronic States and Optical Spectra of ZnS and CdS Crystallites in the ≅15 to 50 Å Size Range: Evolution from Molecular to Bulk Semiconducting Properties. *J. Chem. Phys.* **1985**, *82* (1), 552–559. DOI: 10.1063/1.448727.

(6) Mayorov, A. S.; Gorbachev, R. V.; Morozov, S. V.; Britnell, L.; Jalil, R.; Ponomarenko, L. A.; Blake, P.; Novoselov, K. S.; Watanabe, K.; Taniguchi, T.; Geim, A. K. Micrometer-Scale Ballistic Transport in Encapsulated Graphene at Room Temperature. *Nano Lett.* **2011**, *11* (6), 2396–2399. DOI: 10.1021/nl200758b.

(7) Lee, C.; Wei, X.; Kysar, J. W.; Hone, J. Measurement of the Elastic Properties and Intrinsic Strength of Monolayer Graphene. *Science* **2008**, *321* (5887), 385–388. DOI: 10.1126/science.1157996.

(8) Geim, A. K.; Grigorieva, I. V. Van Der Waals Heterostructures. *Nature* **2013**, *499* (7459), 419–425. DOI: 10.1038/nature12385.

(9) Watanabe, K.; Taniguchi, T.; Kanda, H. Direct-Bandgap Properties and Evidence for Ultraviolet Lasing of Hexagonal Boron Nitride Single Crystal. *Nat. Mater.* **2004**, *3* (6), 404–409. DOI: 10.1038/nmat1134.

(10) Falin, A.; Cai, Q.; Santos, E. J. G.; Scullion, D.; Qian, D.; Zhang, R.; Yang, Z.; Huang, S.; Watanabe, K.; Taniguchi, T.; Barnett, M. R.; Chen, Y.; Ruoff, R. S.; Li, L. H. Mechanical Properties of Atomically Thin Boron Nitride and the Role of Interlayer Interactions. *Nat. Commun.* **2017**, *8*, 15815. DOI: 10.1038/ncomms15815.

(11) Li, L. H.; Cervenka, J.; Watanabe, K.; Taniguchi, T.; Chen, Y. Strong Oxidation Resistance of Atomically Thin Boron Nitride Nanosheets. *ACS Nano* **2014**, *8* (2), 1457–1462. DOI: 10.1021/nn500059s.

(12) Li, X.; Cai, W.; An, J.; Kim, S.; Nah, J.; Yang, D.; Piner, R.; Velamakanni, A.; Jung, I.; Tutuc, E.; Banerjee, S. K.; Colombo, L.; Ruoff, R. S. Large-Area Synthesis of High-Quality and Uniform Graphene Films on Copper Foils. *Science* **2009**, *324* (5932), 1312–1314. DOI: 10.1126/science.1171245.

(13) Castellanos-Gomez, A.; Vicarelli, L.; Prada, E.; Island, J. O.; Narasimha-Acharya, K. L.; Blanter, S. I.; Groenendijk, D. J.; Buscema, M.; Steele, G. A.; Alvarez, J. V.; Zandbergen, H. W.; Palacios, J. J.; van der Zant, H. S. J. Isolation and Characterization of Few-Layer Black Phosphorus. *2D Mater.* **2014**, *1* (2), 025001. DOI: 10.1088/2053-1583/1/2/025001.

(14) Li, L.; Yu, Y.; Ye, G. J.; Ge, Q.; Ou, X.; Wu, H.; Feng, D.; Chen, X. H.; Zhang, Y. Black Phosphorus Field-Effect Transistors. *Nat. Nanotechnol.* **2014**, *9* (5), 372–377. DOI: 10.1038/nnano.2014.35.

(15) Splendiani, A.; Sun, L.; Zhang, Y.; Li, T.; Kim, J.; Chim, C.-Y.; Galli, G.; Wang, F. Emerging Photoluminescence in Monolayer MoS2. *Nano Lett.* **2010**, *10* (4), 1271–1275. DOI: 10.1021/nl903868w.

(16) Chiu, M.-H.; Zhang, C.; Shiu, H.-W.; Chuu, C.-P.; Chen, C.-H.; Chang, C.-Y. S.; Chen, C.-H.; Chou, M.-Y.; Shih, C.-K.; Li, L.-J. Determination of Band Alignment in the Single-Layer MoS2/WSe2 Heterojunction. *Nat. Commun.* **2015**, *6*, 7666. DOI: 10.1038/ncomms8666.

(17) Qian, X.; Liu, J.; Fu, L.; Li, J. Solid State Theory. Quantum Spin Hall Effect in Two-Dimensional Transition Metal Dichalcogenides. *Science* **2014**, *346* (6215), 1344–1347. DOI: 10.1126/science.1256815.

(18) Reina, A.; Son, H.; Jiao, L.; Fan, B.; Dresselhaus, M. S.; Liu, Z.; Kong, J. Transferring and Identification of Single- and Few-Layer Graphene on Arbitrary Substrates. *J. Phys. Chem. C* **2008**, *112* (46), 17741–17744. DOI: 10.1021/jp807380s.

(19) Gupta, P.; Dongare, P. D.; Grover, S.; Dubey, S.; Mamgain, H.; Bhattacharya, A.; Deshmukh, M. M. A Facile Process for Soak-and-Peel Delamination of CVD Graphene from Substrates Using Water. *Sci. Rep.* **2014**, *4*, 3882. DOI: 10.1038/srep03882.

(20) Liu, K.; Zhang, L.; Cao, T.; Jin, C.; Qiu, D.; Zhou, Q.; Zettl, A.; Yang, P.; Louie, S. G.; Wang, F. Evolution of Interlayer Coupling in Twisted Molybdenum Disulfide Bilayers. *Nat. Commun.* **2014**, *5*, 4966. DOI: 10.1038/ncomms5966.

(21) Huang, S.; Ling, X.; Liang, L.; Kong, J.; Terrones, H.; Meunier, V.; Dresselhaus, M. S. Probing the Interlayer Coupling of Twisted Bilayer MoS2 Using Photoluminescence Spectroscopy. *Nano Lett.* **2014**, *14* (10), 5500–5508. DOI: 10.1021/nl5014597.

(22) Zhong, Y.; Cheng, B.; Park, C.; Ray, A.; Brown, S.; Mujid, F.; Lee, J.-U.; Zhou, H.; Suh, J.; Lee, K.-H.; Mannix, A. J.; Kang, K.; Sibener, S. J.; Muller, D. A.; Park, J. Wafer-Scale

Synthesis of Monolayer Two-Dimensional Porphyrin Polymers for Hybrid Superlattices. *Science* **2019**, *366* (6471), 1379–1384. DOI: 10.1126/science.aax9385.

(23) Mannix, A. J.; Ye, A.; Sung, S. H.; Ray, A.; Mujid, F.; Park, C.; Lee, M.; Kang, J.-H.; Shreiner, R.; High, A. A.; Muller, D. A.; Hovden, R.; Park, J. Robotic Four-Dimensional Pixel Assembly of van Der Waals Solids. *Nat. Nanotechnol.* **2022**, *17* (4), 361–366. DOI: 10.1038/s41565-021-01061-5.

(24) Coleman, J. N.; Lotya, M.; O'Neill, A.; Bergin, S. D.; King, P. J.; Khan, U.; Young, K.; Gaucher, A.; De, S.; Smith, R. J.; Shvets, I. V.; Arora, S. K.; Stanton, G.; Kim, H.-Y.; Lee, K.; Kim, G. T.; Duesberg, G. S.; Hallam, T.; Boland, J. J.; Wang, J. J.; Donegan, J. F.; Grunlan, J. C.; Moriarty, G.; Shmeliov, A.; Nicholls, R. J.; Perkins, J. M.; Grieveson, E. M.; Theuwissen, K.; McComb, D. W.; Nellist, P. D.; Nicolosi, V. Two-Dimensional Nanosheets Produced by Liquid Exfoliation of Layered Materials. *Science* **2011**, *331* (6017), 568–571. DOI: 10.1126/science.1194975.

(25) Nicolosi, V.; Chhowalla, M.; Kanatzidis, M. G.; Strano, M. S.; Coleman, J. N. Liquid Exfoliation of Layered Materials. *Science* **2013**, *340* (6139), 1226419–1226419. DOI: 10.1126/science.1226419.

(26) Cunningham, G.; Lotya, M.; Cucinotta, C. S.; Sanvito, S.; Bergin, S. D.; Menzel, R.; Shaffer, M. S. P.; Coleman, J. N. Solvent Exfoliation of Transition Metal Dichalcogenides: Dispersibility of Exfoliated Nanosheets Varies Only Weakly between Compounds. *ACS Nano* **2012**, *6* (4), 3468–3480. DOI: 10.1021/nn300503e.

(27) Kelly, A. G.; Hallam, T.; Backes, C.; Harvey, A.; Esmaeily, A. S.; Godwin, I.; Coelho, J.; Nicolosi, V.; Lauth, J.; Kulkarni, A.; Kinge, S.; Siebbeles, L. D. A.; Duesberg, G. S.; Coleman, J. N. All-Printed Thin-Film Transistors from Networks of Liquid-Exfoliated Nanosheets. *Science* **2017**, *356* (6333), 69–73. DOI: 10.1126/science.aal4062.

(28) Watcharotone, S.; Dikin, D. A.; Stankovich, S.; Piner, R.; Jung, I.; Dommett, G. H. B.; Evmenenko, G.; Wu, S.-E.; Chen, S.-F.; Liu, C.-P.; Nguyen, S. T.; Ruoff, R. S. Graphene-Silica Composite Thin Films as Transparent Conductors. *Nano Lett.* **2007**, *7* (7), 1888–1892. DOI: 10.1021/nl070477+.

(29) Zheng, Q.; Ip, W. H.; Lin, X.; Yousefi, N.; Yeung, K. K.; Li, Z.; Kim, J.-K. Transparent Conductive Films Consisting of Ultralarge Graphene Sheets Produced by Langmuir-Blodgett Assembly. *ACS Nano* **2011**, *5* (7), 6039–6051. DOI: 10.1021/nn2018683.

(30) Baumgardner, W. J.; Whitham, K.; Hanrath, T. Confined-but-Connected Quantum Solids via Controlled Ligand Displacement. *Nano Lett.* **2013**, *13* (7), 3225–3231. DOI: 10.1021/nl401298s.

(31) Murray, C. B.; Kagan, C. R.; Bawendi, M. G. Self-Organization of CdSe Nanocrystallites into Three-Dimensional Quantum Dot Superlattices. *Science* **1995**, *270* (5240), 1335–1338. DOI: 10.1126/science.270.5240.1335.

(32) Stankovich, S.; Dikin, D. A.; Dommett, G. H. B.; Kohlhaas, K. M.; Zimney, E. J.; Stach, E. A.; Piner, R. D.; Nguyen, S. T.; Ruoff, R. S. Graphene-Based Composite Materials. *Nature* **2006**, *442* (7100), 282–286. DOI: 10.1038/nature04969.

(33) Eda, G.; Fanchini, G.; Chhowalla, M. Large-Area Ultrathin Films of Reduced Graphene Oxide as a Transparent and Flexible Electronic Material. *Nat. Nanotechnol.* **2008**, *3* (5), 270–274. DOI: 10.1038/nnano.2008.83.

(34) Chen, X.; Kohring, M.; Assebban, M.; Tywoniuk, B.; Bartlam, C.; Moses Badlyan, N.; Maultzsch, J.; Duesberg, G. S.; Weber, H. B.; Knirsch, K. C.; Hirsch, A. Covalent Patterning of 2D Mos2. *Chem. Eur. J* **2021**, *27* (52), 13117–13122. DOI: 10.1002/chem.202102021.

(35) Kang, N.; Paudel, H. P.; Leuenberger, M. N.; Tetard, L.; Khondaker, S. I. Photoluminescence Quenching in Single-Layer MoS_2 via Oxygen Plasma Treatment. *J. Phys. Chem. C* **2014**, *118* (36), 21258–21263. DOI: 10.1021/jp506964m.

(36) Georgakilas, V.; Otyepka, M.; Bourlinos, A. B.; Chandra, V.; Kim, N.; Kemp, K. C.; Hobza, P.; Zboril, R.; Kim, K. S. Functionalization of Graphene: Covalent and Non-Covalent Approaches, Derivatives and Applications. *Chem. Rev.* **2012**, *112* (11), 6156–6214. DOI: 10.1021/cr3000412.

(37) Ali, A.; Rehman, F.; Ali Khan, M.; Memon, F. H.; Soomro, F.; Iqbal, M.; Yang, J.; Thebo, K. H. Functionalized Graphene Oxide-Based Lamellar Membranes with Tunable Nanochannels for Ionic and Molecular Separation. *ACS Omega* **2022**, *7* (36), 32410–32417. DOI: 10.1021/acsomega.2c03907.

(38) Naguib, M.; Kurtoglu, M.; Presser, V.; Lu, J.; Niu, J.; Heon, M.; Hultman, L.; Gogotsi, Y.; Barsoum, M. W. Two-Dimensional Nanocrystals Produced by Exfoliation of Ti3 AlC2. *Adv. Mater.* **2011**, *23* (37), 4248–4253. DOI: 10.1002/adma.201102306.

(39) Naguib, M.; Mashtalir, O.; Carle, J.; Presser, V.; Lu, J.; Hultman, L.; Gogotsi, Y.; Barsoum, M. W. Two-Dimensional Transition Metal Carbides. *ACS Nano* **2012**, *6* (2), 1322–1331. DOI: 10.1021/nn204153h.

(40) Wang, K.; Jin, H.; Li, H.; Mao, Z.; Tang, L.; Huang, D.; Liao, J.-H.; Zhang, J. Role of Surface Functional Groups to Superconductivity in Nb2C-MXene: Experiments and Density Functional Theory Calculations. *Surfaces and Interfaces* **2022**, *29*, 101711. DOI: 10.1016/j.surfin.2021.101711.

(41) Pandey, A.; Sardana, N. Effect of Functionalization on Properties of Scandium-Based MXenes: A DFT Study. *Comp. Mater. Sci.* **2025**, *248*, 113598. DOI: 10.1016/j.commatsci.2024.113598.

(42) Whittingham, M. S.; Gamble, F. R. The Lithium Intercalates of the Transition Metal Dichalcogenides. *Mater. Res. Bull.* **1975**, *10* (5), 363–371. DOI: 10.1016/0025-5408(75)90006-9.

(43) Whittingham, M. S. Electrical Energy Storage and Intercalation Chemistry. *Science* **1976**, *192* (4244), 1126–1127. DOI: 10.1126/science.192.4244.1126.

(44) Mizushima, K.; Jones, P. C.; Wiseman, P. J.; Goodenough, J. B. LixCoO2 (0< X< -1): A New Cathode Material for Batteries of High Energy Density. *Mater. Res. Bull.* **1980**, *15* (6), 783–789. DOI: 10.1016/0025-5408(80)90012-4.

(45) Fong, R.; von Sacken, U.; Dahn, J. R. Studies of Lithium Intercalation into Carbons Using Nonaqueous Electrochemical Cells. *J. Electrochem. Soc.* **1990**, *137* (7), 2009–2013. DOI: 10.1149/1.2086855.

(46) Gamble, F. R.; Osiecki, J. H.; Cais, M.; Pisharody, R.; Disalvo, F. J.; Geballe, T. H. Intercalation Complexes of Lewis Bases and Layered Sulfides: A Large Class of New Superconductors. *Science* **1971**, *174* (4008), 493–497. DOI: 10.1126/science.174.4008.493.

(47) Moncton, D. E.; Axe, J. D.; DiSalvo, F. J. Study of Superlattice Formation In-Nband-Taby Neutron Scattering. *Phys. Rev. Lett.* **1975**, *34* (12), 734–737. DOI: 10.1103/PhysRevLett.34.734.

(48) Di Salvo, F. J.; Hull, G. W.; Schwartz, L. H.; Voorhoeve, J. M.; Waszczak, J. V. Metal Intercalation Compounds of TaS2: Preparation and Properties. *J. Chem. Phys.* **1973**, *59* (4), 1922–1929. DOI: 10.1063/1.1680277.

(49) Wang, C.; He, Q.; Halim, U.; Liu, Y.; Zhu, E.; Lin, Z.; Xiao, H.; Duan, X.; Feng, Z.; Cheng, R.; Weiss, N. O.; Ye, G.; Huang, Y.-C.; Wu, H.; Cheng, H.-C.; Shakir, I.; Liao, L.; Chen, X.; Goddard, W. A.; Huang, Y.; Duan, X. Monolayer Atomic Crystal Molecular Superlattices. *Nature* **2018**, *555* (7695), 231–236. DOI: 10.1038/nature25774.

(50) Lin, Z.; Wan, Z.; Song, F.; Huang, B.; Jia, C.; Qian, Q.; Kang, J. S.; Wu, Y.; Yan, X.; Peng, L.; Wan, C.; Zhou, J.; Sofer, Z.; Shakir, I.; Almutairi, Z.; Tolbert, S.; Pan, X.; Hu, Y.; Huang, Y.; Duan, X. High-Yield Exfoliation of 2D Semiconductor Monolayers and Reassembly of Organic/Inorganic Artificial Superlattices. *Chem* **2021**. DOI: 10.1016/j.chempr.2021.03.022.

(51) Qian, Q.; Ren, H.; Zhou, J.; Wan, Z.; Zhou, J.; Yan, X.; Cai, J.; Wang, P.; Li, B.; Sofer, Z.; Li, B.; Duan, X.; Pan, X.; Huang, Y.; Duan, X. Chiral Molecular Intercalation Superlattices. *Nature* **2022**, *606* (7916), 902–908. DOI: 10.1038/s41586-022-04846-3.

(52) Johnson, J. W. Amine Intercalation in Tantalum Disulfide: The Effect of Small Amounts of Water. *Physica B+C* **1980**, *99* (1–4), 141–144. DOI: 10.1016/0378-4363(80)90223-5.

(53) Lomax, J. F.; Diel, B. N.; Marks, T. J. New Information On 2H-TaS_2 Intercalation Chemistry With Organic Bases. *Molecular Crystals and Liquid Crystals* **1985**, *121* (1–4), 145–148. DOI: 10.1080/00268948508074850.

(54) Py, M. A.; Haering, R. R. Structural Destabilization Induced by Lithium Intercalation in MoS_2 and Related Compounds. *Can. J. Phys.* **1983**, *61* (1), 76–84. DOI: 10.1139/p83-013.

(55) Woollam, J. A.; Somoano, R. B. Physics and Chemistry of MoS2 Intercalation Compounds. *Materials Science and Engineering* **1977**, *31*, 289–295. DOI: 10.1016/0025-5416(77)90048-9.

(56) Friend, R. H.; Yoffe, A. D. Electronic Properties of Intercalation Complexes of the Transition Metal Dichalcogenides. *Adv. Phys.* **1987**, *36* (1), 1–94. DOI: 10.1080/00018738700101951.

(57) Joensen, P.; Frindt, R. F.; Morrison, S. R. Single-Layer MoS2. *Mater. Res. Bull.* **1986**, *21* (4), 457–461. DOI: 10.1016/0025-5408(86)90011-5.

(58) Divigalpitiya, W. M.; Frindt, R. F.; Morrison, S. R. Inclusion Systems of Organic Molecules in Restacked Single-Layer Molybdenum Disulfide. *Science* **1989**, *246* (4928), 369–371. DOI: 10.1126/science.246.4928.369.

(59) Kuo, D.-Y.; Cossairt, B. M. Direct Intercalation of MoS2 and WS2 Thin Films by Vacuum Filtration. *Mater. Horiz.* **2022**, *9* (1), 360–367. DOI: 10.1039/d1mh01193f.

(60) Sim, D. M.; Han, H. J.; Yim, S.; Choi, M.-J.; Jeon, J.; Jung, Y. S. Long-Term Stable 2H-MoS2 Dispersion: Critical Role of Solvent for Simultaneous Phase Restoration and Surface Functionalization of Liquid-Exfoliated MoS2. *ACS Omega* **2017**, *2* (8), 4678–4687. DOI: 10.1021/acsomega.7b00841.

(61) Chou, S. S.; Huang, Y.-K.; Kim, J.; Kaehr, B.; Foley, B. M.; Lu, P.; Dykstra, C.; Hopkins, P. E.; Brinker, C. J.; Huang, J.; Dravid, V. P. Controlling the Metal to Semiconductor Transition of MoS2 and WS2 in Solution. *J. Am. Chem. Soc.* **2015**, *137* (5), 1742–1745. DOI: 10.1021/ja5107145.

(62) Whitby, M.; Cagnon, L.; Thanou, M.; Quirke, N. Enhanced Fluid Flow through Nanoscale Carbon Pipes. *Nano Lett.* **2008**, *8* (9), 2632–2637. DOI: 10.1021/nl080705f.

(63) Whitby, M.; Quirke, N. Fluid Flow in Carbon Nanotubes and Nanopipes. *Nat. Nanotechnol.* **2007**, *2* (2), 87–94. DOI: 10.1038/nnano.2006.175.

CHAPTER TWO – METHODS FOR PREPARATION, PROCESSING, AND CHARACTERIZATION OF 2D MATERIALS AND FILMS

Introduction

Because of the great variety of 2D materials, I have learned to use many different techniques to both fabricate thin films and study the properties of these materials. Much of my work has been performed on MoS_2, although many of the techniques I describe in this chapter should theoretically be applicable to other types of TMDCs and 2D van der Waal's materials. In this chapter, I outline both the experimental and computational methods that I have found to work well, particularly with the MoS_2-molecule superlattice system. These methods include techniques for the chemical exfoliation and subsequent recovery of monolayer MoS_2 (Section 2.1), the assembly of superlattices from monolayer solutions (Section 2.2), electrochemical methods to intercalate the material, and finally, the use of MD (particularly LAMMPS) to calculate various physical properties, including energy barriers, diffusion coefficients, and solvation energies (Section 2.4).

2.1 Chemical exfoliation of MoS_2

There are many different ways to prepare monolayers of MoS_2, including hydrothermal synthesis[1], atomic layer/chemical vapor deposition[2,3], and various bulk crystal exfoliation methods[4]. While bottom-up synthesis methods are useful for preparing bulk crystals and pristine monolayers, liquid exfoliation methods generating suspensions of monolayers are more useful when attempting to fabricate solid devices that are composed of more than one monolayer. Additionally, suspensions of 2D materials are easier to work with and can be used in a variety of

well understood ways, such as spin/spray coating, electrodeposition, and various interfacial assembly techniques, to generate ordered solids.

To generate suspensions of MoS_2, there are two main methods that can exfoliate bulk crystals into a solvent: the "standard" liquid exfoliation method and chemical exfoliation. The standard liquid exfoliation method, popularized by Coleman and coworkers[5,6], uses a highly polar solvent (typically N-methylpyrrolidone (NMP), or similar nitrogen-containing molecules) and ultrasonication to break apart the layers of a bulk 2D crystal. This method is highly generalizable and has been shown to work with a variety of different 2D materials. However, it has a significant downside, namely, it does not generate a high fraction of true monolayers; typically, small flakes are 2-5 layers thick. As previously mentioned, bilayer and thicker flakes are much less quantum confined than monolayer flakes are and therefore lose many of the desirable properties. For a step-by-step guide and a more in-depth discussion of the pros and cons of the standard liquid exfoliation method, see my predecessor Tyler Farnsworth's dissertation.

For many 2D material systems, a monolayer is much more desirable than even a bilayer. For example, in MoS_2, the monolayer material has a direct bandgap, whereas the bilayer and thicker materials have an indirect bandgap[7,8]. One of the most effective ways to generate solutions of monolayers is chemical exfoliation, which was demonstrated with MoS_2 by Morrison and coworkers in the late 1980s[9]. This method relies on the intercalation of lithium into the layered crystal and the subsequent reaction with water to generate interlayer hydrogen gas and separate the layers. I have adapted the method used by Tyler Farnsworth, who in turn adapted it from Eda and coworkers[8]. Both the method outlined here by me and the method outlined by Tyler in his thesis work to generate monolayers, although I find that my method results in higher yield with fewer impurities.

2.1.1 Generation of a metallic (1T) monolayer solution

First, bulk MoS_2 powder (300 mg) and 3 mL of 1.6 M n-butyllithium (n-buLi) in hexanes were added to a sealed scintillation vial, and the mixture was allowed to sit for 48 hours under a nitrogen atmosphere. I found no difference in the final product between performing the intercalation in a glove box and in a scintillation vial sealed with a rubber septum. Despite suggestions in the literature, I also found that both stirring and heating (~60°C) were unnecessary and resulted in a final product similar to that of this method. After 48 hours, the MoS_2 powder visibly swells to 2–3 times its original volume. Letting the mixture sit for more than 72 hours results in drastically lower yield, and I would not recommend using any material generated from such a synthesis.

This intercalated powder is highly reactive with air and water and must be handled quickly to prevent the loss of product. After the powder and n-buLi were allowed to sit for 48 hours, the sealed vial was briefly sonicated to agitate the powder and disperse it in the hexanes. After sonicating, the sides of the vial were dried, the powder was recovered via vacuum filtration, and the powder was washed out of the vial with additional hexanes (~100 mL). During this step, it is crucial to act quickly and ensure that there is no trace water anywhere near the system. Using gloves that are even slightly wet will cause the filter paper to combust and result in the loss of product, as will exposing the powder to air for too long. Oxidation will be obvious during the filtration step, as the black powder will turn white and begin smoking. I found that ending the filtration early, while the powder is still slightly wet with hexanes, results in the maximum yield, as the hexanes protect the powder from immediate oxidation.

After the powder was recovered in a 100 mL scintillation vial, 100 mL of DI water was added to the powder, and the vial was sealed with electrical tape. If the powder is still slightly wet

with hexanes, it should not mix well with the water and instead will sit on top, forming an obvious interface. Vigorous shaking allows the 2 phases to mix, resulting in a black, bubbly, highly alkaline suspension. Sonicating this suspension for 1 hour results in exfoliation of the intercalated material.

Next, to use the suspension of monolayers for device fabrication, we must first purify it and, in particular, wash off the lithium salts and lower the alkalinity of the suspension. I found this centrifugation procedure to work best for purification:

1) The material was centrifuged for 40 minutes at 3,000 rpm, and the supernatant was collected. This removes all unexfoliated material, which can be anywhere from 50–80% of the starting MoS_2. The faster the material is filtered and the better it is protected from oxidation, the higher the yield of exfoliated material will be.
2) The supernatant was mixed in a 1:1 ratio with isopropanol. Isopropanol is a worse solvent than water for the monolayers and helps the material crash out of the solution in the subsequent centrifugation steps. The suspension was centrifuged at 19,000 rpm for 2 hours, and the resulting precipitate was collected. The precipitate must not be allowed to dry out, as this will result in irreversible restacking of the material. The resulting supernatant was clear or pale yellow and was discarded. If the supernatant is black, I would suggest resuspending and diluting the suspension by 50% and performing the same centrifugation again. After this step, it is possible to combine centrifugation fractions, although I would avoid trying to combine more than 2 fractions at a time, as I have found it difficult to collect all of the precipitates fully without the addition of a large amount of liquid.

3) The precipitate was washed by centrifuging in 1:1 water/isopropanol at 19,000 rpm for 1 hour. The precipitate was collected, the supernatant was discarded, and the fractions were combined as needed. After 2–3 washes, the pH of the solution should approach neutral and be usable in film fabrication. It is critically important to never let the monolayers fully dry out, as this will result in irreversible restacking. Even leaving them in ~1 mL of water is sufficient to prevent this at least overnight.

Additionally, I have successfully scaled this method up to ~2 g of MoS_2 while still obtaining a reasonable (~20%) yield. It is important to scale the amount of water used for the sonication and centrifugation steps such that the concentration of MoS_2 does not exceed 5 g/mL. If the suspension is too concentrated, the nanosheets will restack, most likely through a liquid crystalline intermediate phase[10]. However, when dealing with larger amounts of n-buLi, extra care must be taken, as n-buLi is pyrophoric. In particular, the most dangerous step is the filtration, as this involves exposing the n-buLi to air and placing it in contact with flammable filter paper. To mitigate risk, I found that using a syringe to remove excess n-buLi solution before filtration while the vial is still sealed results in fewer fires involving the filter paper. I would not recommend trying this procedure above the 2 g scale, as it will be necessary to switch the filter paper out halfway through, and letting the powder sit outside of a nitrogen atmosphere will result in oxidation of the MoS_2-Li powder.

In addition to using n-buLi as a lithiation agent, I have also found success in using pyrene-lithium (Py-Li), as suggested in other works[11]. This lithium reagent has the distinct advantage of being far less hazardous than n-buLi, even being relatively air stable for short periods of time. However, annoyingly, Py-Li is not commercially available, so it must be prepared before use via this procedure. This technique works well, and is straightforward:

1) In a glove box, 2.04 g of pyrene was dissolved in 50 mL of an ether while stirring. I have used both dimethyl ether and 1,3-dioxalane to successfully dissolve the molecule.
2) After the pyrene dissolves, 140 mg of lithium metal was added to this yellow solution. Typically, I use lithium foil, which I scrub first with a toothbrush to remove the oxide layer. As the lithium dissolves, the mixture will turn blood red.
3) This mixture was stirred overnight before use and must be stored while stirring. I would suggest using the mixture within 2 weeks of preparation, as waiting longer causes the formation of a precipitate at the bottom of the scintillation vial even with stirring.

To exfoliate the MoS_2, the powder is intercalated and collected via filtration following a similar procedure to that of n-buLi exfoliation. Importantly, a slight molar excess (~1.1-1.2 eq.) of Py-Li must be used. Additionally, allowing the mixture to sit of more than 1 day after combining the MoS_2 and Py-Li results in lower yield; I typically conducted exfoliation within 12 hours and found that waiting longer was not necessary. Additionally, extra care must be taken in cleaning the resulting monolayer suspension to remove excess pyrene from the solution. I would suggest an additional wash with hexanes or similar nonpolar solvent before using in thin film fabrication. This method affords a yield similar to that of n-buLi exfoliation with a greatly reduced hazard, although I have spent much less time optimizing this procedure.

Another method to incorporate lithium into TMDCs suggested to me by Michael Naguib involves mechanochemical intercalation. This method is extremely scalable (100 g scale vs <5 g), although I have only gotten it to work with middling success. To perform this method of lithium intercalation, the TMDC powder was simply sprinkled onto lithium foil, and the foil was folded over itself and pressed into the powder. It was suggested to me to use a pasta maker to press the foil together, but lacking that, I used a pellet press at low pressure (<2000 lbs). After the pellet is

formed, it is put in water and sonicated for 1 hour. This process exfoliates the material in a reasonable yield (~10%) and generates solutions similar to those used for n-buLi exfoliation, although this procedure is far less optimized than the either of the chemical methods previously mentioned.

2.1.2 Conversion from the metallic (1T) to semiconducting (2H) phase

For many electronic uses, having access to a solution of semiconducting monolayers is much more useful than having access to a solution of metallic monolayers. Unfortunately, chemical exfoliation induces a phase transition from the semiconducting (2H) to metallic phase (1T). However, the 1T phase is metastable and therefore straightforward to convert back to the 2H phase. Previous work has shown that low-temperature annealing (~300°C) in an oxygen-free environment of films cast from metallic MoS_2 is sufficient to convert ~95% of the 1T phase back to the 2H phase[8]. However, casting films leads to MoS_2 monolayers being returned to the solid state where solution processing methods are no longer viable, as drying a suspension of monolayers results in irreversible restacking. Therefore, the annealing must be conducted in an appropriately high boiling solvent which prevents the material from restacking.

Solution-phase annealing methods are quite difficult however, as the 2H and 1T phases require different types of solvents to maintain a stable suspension. This is most likely due to the high partial charge left over on the MoS_2 monolayers from the exfoliation process[9], which gives the 1T monolayers good dispersibility in highly polar solvents but low dispersibility in nonpolar solvents[12]. The dispersibility of metallic monolayers is so low in nonpolar solvents that they will crash out of solution and restack, leading to bulk MoS_2. To further complicate this problem, annealing tends to reduce the surface charge of the monolayers[12,13], such that after annealing, the opposite trend is observed where 2H monolayers tend to crash out of polar solvents and restack

into bulk material. Previous work has attempted to remedy this problem by attaching ligands to increase dispersibility in high-boiling, nonpolar solvents, but this approach is associated with the obvious downside of surface functionalization of the material, making further processing and recovery of interesting properties much more difficult[12].

In addition to attaching ligands to increase dispersibility, other works have shown that annealing in neat NMP also works to keep both the 1T and 2H phases suspended[13]. In this work, annealing at ~200°C in a variety of solvents was found to induce ~85% conversion from the 1T to 2H phase. However, similar to previous works, unfunctionalized MoS_2 crashes out from solvents after annealing, with the exception of NMP and the partial exception of formamide. The authors attributed this observation to the degradation of NMP surface functionalizing the MoS_2, where the NMP decomposes and nitrogen groups react with molybdenum atoms to provide 2H monolayers with high dispersibility after annealing. The resulting suspension of surface-functionalized 2H MoS_2 showed remarkably high solution stability, remaining suspended for months after annealing. However, these 2H monolayers are still surface functionalized and not pristine, so the recovery of the interesting monolayer properties is not necessarily possible.

2.1.3 Annealing procedure to generate solutions of 2H monolayers

To build off the previous work of Morrison and coworkers and realize the general assembly of molecules with MoS_2, I found it necessary to generate a solution of unfunctionalized monolayers. Tyler wrote a procedure in his dissertation that used N,N'-dimethylpropyleneurea (DMPU), a similar solvent to NMP in terms of structure and boiling point. However, I found that annealing in DMPU might have led to surface functionalization of the monolayers, similar to that described in previous reports[13]. On the basis of the similarities in structure between NMP and DMPU, I would not be surprised if this were the case, although finding direct evidence of this

surface functionalization is quite difficult. The best evidence I have for DMPU functionalizing the material is in diffraction patterns of lattices assembled with "different" molecules. Typically we can see a change in in interlayer spacing when other molecules are assembled into films with our MoS_2, but with films annealed in DMPU, the superlattices typically have the same spacing of 10.0 Å despite different molecules nominally incorporating.

2.1.4 Analysis of solvent and annealing parameters

In choosing a solvent for our annealing procedure, we first examined solvents that have often been used for dispersing uncharged 2D materials, such as N-methylpyrrolidone (NMP). However, NMP has a boiling point of 200°C, which is significantly lower than the 300°C that is often used in solid-state annealing procedures. Additionally, annealing in NMP has been shown to covalently functionalize the surface of MoS_2, which we wanted to avoid. To find other candidate solvents for our annealing procedure, we examined the Hansen solubility parameters of related solvents. For this analysis, we chose DMPU, a higher boiling (~250°C) solvent with a similar Hansen parameter to that of NMP. After 1T MoS_2 dispersions were annealed in DMPU, our initial characterization of the suspension appeared promising. We observed both high conversion from the 1T to 2H phase by UV–vis and qualitatively, that the solvent worked extremely well for dispersing the 2D nanosheets both before and after annealing. Annealing for ~24 hours was needed to induce flocculation of the MoS_2 nanosheets in these DMPU suspensions.

The problem with refluxing in DMPU was that it proved impossible to fully separate DMPU from MoS_2, even with repeated centrifugation steps. On the basis of previous reports, we hypothesize that the nitrogen in DMPU strongly interacts with MoS_2 and prevents solvent removal during the purification process. This led us to use propylene carbonate (PC) as the refluxing solvent, as it has a similar Hansen parameter to DMPU, boils at a similar temperature, and most

importantly, contains no nitrogen. We found that PC effectively dispersed the nanosheets after refluxing for 4 hours. Refluxing for longer than 4 hours led to flocculation of the MoS_2 nanosheets. While PC is a worse solvent for dispersing both metallic and semiconducting MoS_2, we found that ~4 hours of reflux was sufficient to induce conversion from the 1T to 2H phase while still producing stable suspensions.

My annealing procedure is similar to Tyler's procedure, although I did find some optimizations in addition to the obvious change in solvent from DMPU to PC:

1) First, the washed (see above) metallic monolayers were transferred from water/IPA into ~50 mL of PC in a round bottom flask. If the exfoliation process is scaled, it is important to scale the amount of PC proportionally. It is not necessary to remove 100% of the water, as we heat the solution well above 100^{o} C during the reflux, which will boil off any remaining water.
2) The suspensions were stirred and sparged by submerging a nitrogen needle below the liquid. Nitrogen is bubbled through the PC for ~15 minutes to remove oxygen, as residual oxygen will oxidize the MoS_2. If the bubbler is left open to check the N_2 flow rate during the sparging process, it is important to turn off the stirrer temporarily and check for bubbles coming from the needle. If there are no bubbles, simply close the bubbler for the duration of the sparging but make sure to reopen before heating. I have found that the nitrogen line in lab often requires the bubbler to be closed in order to degas the solvent.
3) After sparging, a condenser fitted with a rubber septum is attached to the flask, cold water is run through the condenser, and vacuum is pulled through a needle for approximately one minute to remove any gases remaining in the system. While

vacuum is being applied, some bubbles should be visible in the liquid, but it should not boil.

4) Turn off the vacuum and backfill the flask with nitrogen. The flask will be kept under nitrogen for the duration of the annealing procedure.
5) The reaction setup was placed into a sand bath connected to a Variac heating mantle, and the Variac voltage was set to ~30 V. This should increase the temperature of the reaction mixture to slightly greater than 100°C. The mixture was heated at this temperature for ~20 minutes to remove excess water.
6) After 20 minutes, the voltage was increased to ~65 V. This should gently reflux the suspension. If it is vigorously boiling, turn the voltage down. To check the temperature, a thermometer in the sand bath works well as it is difficult to directly measure the temperature of the suspension in the flask.
7) The suspension is then refluxed for no more than 4 hours. It is important to not reflux the suspension for longer, as this will cause flocculation of the monolayers and result in restacking of the nanosheets upon recovery.
8) To transfer the monolayers out of the PC, it is necessary to add ~60% by volume toluene before centrifuging them via the transfer procedure outlined by Tyler.

By XPS, this procedure results in ~85% 2H monolayers that will remain suspended for approximately one week in PC (Appendix 1). Obviously, annealing for longer than 4 hours results in higher 1T to 2H conversion, but this comes at the cost of monolayer yield. I would advise against using anything annealed longer than 4 hours, as longer annealing does significantly reduce the dispersibility of the monolayers. To preserve the maximum yield of monolayers, I suggest

leaving the monolayers in PC until you are ready to use them and only then transferring them into a different solvent the day you plan to use them.

Additionally, the annealing procedure results in quite low solution stability in many different solvents, as the monolayers are left in a state of low partial charge where they are not stable in either polar or nonpolar solvents. The only solvents in which the monolayers are relatively stable are nitrogen-containing solvents, which I believe are chemically reacting with the surface and should probably be avoided for most device fabrication purposes. Therefore, before using the solution in any assembly procedure, I ensure that the solution is sonicated for ~30 s to break up aggregations, although sometimes it takes a longer time depending on the solvent and how long the solution has been sitting for.

2.2 Assembly of ordered superlattices from a solution of monolayers

Having generated semi-stable solutions of monolayer 2D materials dispersed in a solvent, the next step in the process is to assemble these dispersions into an ordered solid. The target structure for our solid is shown in Figure 1, where we want to generate a solid with alternating layers of 2D materials and molecules. Analogous to quantum dot solids, the molecular layer serves to keep the monolayers of 2D materials far enough apart that they can remain quantum confined.

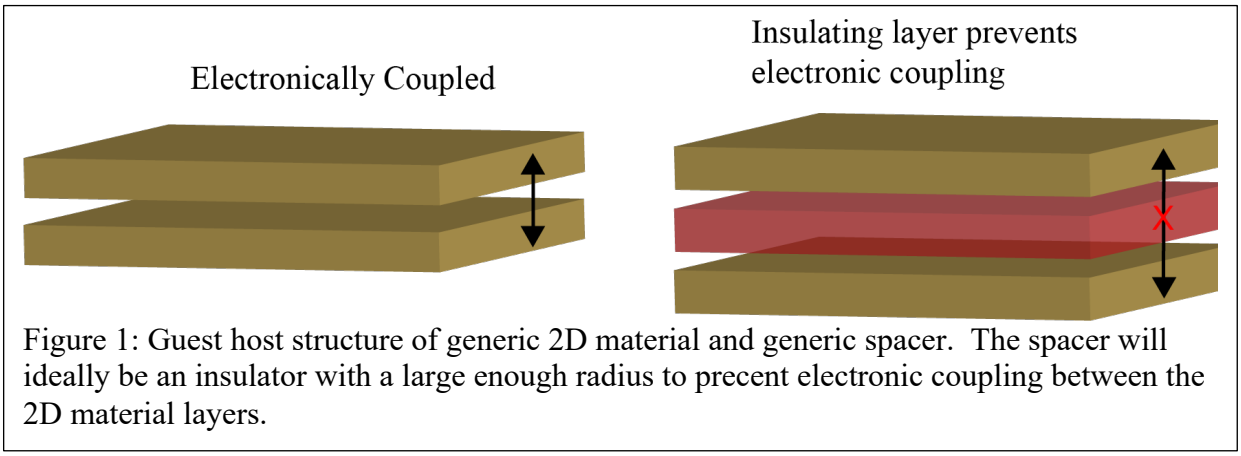


Figure 1: Guest host structure of generic 2D material and generic spacer. The spacer will ideally be an insulator with a large enough radius to precent electronic coupling between the 2D material layers.

In addition to keeping the 2D material layers separate, the molecular layer will also not be bonded to the 2D material, so van der Waal interactions will be the primary interaction keeping this solid together. With this structure in mind, a method utilizing self-assembly is most appropriate, as self-assembly is generalizable to almost any molecule and any 2D material system.

2.2.1 Vacuum filtration for the assembly of thin films

One such self-assembly procedure was outlined by Morrison and coworkers in their work on metallic MoS_2 in the 1980s[9]. In this technique, they utilized the partial charge on the exfoliated nanosheets to assemble MoS_2 at an oil–water interface. By shaking a mixture of nanosheets, water, organic solvent (i.e., hexanes), and nonvolatile organic species (i.e., ferrocene), they were able to incorporate alternating layers of ferrocene into a superlattice of MoS_2. They offer no explanation as to why this structure forms, although they do demonstrate the inclusion of a small variety of molecules that cannot be included by direct intercalation. It was later found that identical structures could be obtained by intercalation via vacuum filtration[14]. In this work, exfoliated MoS_2 and WS_2 were assembled on a filter and subsequently washed with a solution of a nonvolatile organic species to yield a structurally identical superlattice to that of Morrison and coworkers.

I have also found a similar method to work with solutions of monolayers, where these superlattices can be assembled in one step by vacuum filtering a solution of monolayers, solvent, and nonvolatile organic. Following this method, I have been able to assemble fairly crystalline films ~1–10 μm thick containing alternating layers of 2D material and small molecules:

1) When the product of a 300 mg exfoliation of 2D material is transferred into ~5 mL of a solvent, butanol works well enough to disperse the monolayers but does require sonication to break up the aggregates before film fabrication. To this suspension, 50 μL of the desired organic molecule were added.

2) For the filtration step, I found that a PES filter with a pore size of 0.2 μm has a good ratio of fast filtration to good deposition. Increasing the pore size increases the filtration speed at the cost of the film thickness, which makes subsequent analysis more difficult. Importantly, fast flow is important as it allows the deposition to happen fairly quickly, which helps keep the monolayers in the film parallel and highly ordered. To deposit the film, the suspension was simply added dropwise to the filter until a convex bubble was visible on the surface of the filter.
3) Once the liquid on the surface is convex and remains so without the addition of further liquid, the excess liquid is removed by pipetting, and the film is allowed to sit on the filter for 15–20 minutes until it is dry. This should produce a fairly ordered film containing molecules and 2D monolayers.

2.2.2 Doctor blading of superlattices

Doctor blading is a deposition technique that I have found works well on a variety of substrates other than filter paper to assemble thick, lower-order superlattices. Owing to the low ordering of the films relative to other deposition methods, I would recommend using techniques other than doctor blading if possible. Typically, and in my work, doctor blading was used to fabricate electrodes. The method of doctor blading is, however, straightforward and can quickly be used to make many electrodes on a variety of nonporous substrates. To doctor blade a film, I have found the following method to work best:

1) A slurry of 70% active material (in this case, MoS_2 monolayers), 20% conductive carbon black (e.g., Super P), and 10% binder (such as PVDF) in a high boiling solvent such as NMP was mixed together. NMP was added to the solids until they formed a

viscous slurry. I have found that a small amount of sonication helps break apart chunks and minimizes the amount of NMP required to dissolve solids.

2) Tape the desired substrate, typically something such as aluminum foil, onto a ceramic plate. The type of tape used determines the thickness of the doctor-bladed film; thus, the thickness should be chosen carefully on the basis of the desired electrode thickness.
3) The slurry was added to the well created with tape. The slurry is spread across the substrate by pulling a razor blade along the tape, and the blade should be able to spread the slurry easily. More slurry was added to fully coat the substrate, and was spread with a razor blade to ensure an even film.
4) After the entire substrate was evenly coated with the slurry, the electrode was heated at 80°C for ~1 hour to remove excess NMP, and the electrode was set. Not annealing the electrode results in poor binding to the substrate and often results in delamination if the electrode is placed in a liquid. After annealing, the film is ready for use.

2.2.3 Langmuir–Blodgett (LB) interfacial assembly

Another technique that has been utilized for depositing films of 2D materials is Langmuir Blodgett assembly[15,16], which is an interfacial assembly technique that occurs at the air–water interface and consistently assembles high-order films. Similar to the method detailed by Morrison, by utilizing the difference in potential at an interface, 2D materials spontaneously order into superlattices. The main difference between LB deposition and oil–water self-assembly is the presence of perpendicular compression in the LB assembly, which maintains a constant surface pressure during the deposition process. In LB assembly, the solution of monolayers is suspended in a solvent that is immiscible with water and deposited on the surface of the water layer in an LB trough. As the solvent suspending the monolayers evaporates, the 2D materials deposit on the

surface of the water layer, and compression perpendicular to the water surface maintains the surface pressure during the evaporation process. Once the solvent has evaporated, a substrate held parallel to the water can be raised through the resulting film, which will cause the deposition of the 2D materials onto the substrate. Annealing this film to adhere it to the substrate completes 1 cycle of LB deposition. After annealing, the film can be resubmerged to deposit additional LB layers, or experimental measurements can be performed. For a detailed discussion of how to use the LB trough, see Tyler's dissertation. Films are typically deposited on glass microscope slides or silicon wafers and analyzed via a variety of techniques.

One of the main advantages of LB assembly over the oil–water method is the horizontal compression of the LB film. This results in deposition conditions that are much more highly controlled and produce films where the crystalline order is higher. However, LB deposition is also more time consuming, with an average deposition cycle of ~1 hour, which can be difficult because of the low solution stability of our monolayers. I have found that butanol is the only volatile solvent that works for the deposition procedure. However, butanol has the right mix of polarity and volatility, is immiscible with water, and still suspends the MoS_2 nanosheets fairly well. As a solvent, butanol is better at suspending less polar nanosheets, so much so that 1T LB deposition is quite difficult, and I would recommend against using this method with the metallic phase. While it is possible, it is much more difficult and requires frequent sonication to keep the monolayers dispersed.

In addition to those notes on solvent selection, two types of films can be deposited via this method: films containing monolayers of molecules and films containing bilayers of molecules. I believe that the greater control over deposition conditions allows for the formation of a molecular bilayer under the correct conditions, which is why it has not been previously observed with oil–

water or filtration deposition techniques. The way to control molecular monolayer vs bilayer formation is to simply change the concentration of the nonvolatile molecule relative to the 2D material. However, this only works with certain molecules and will be discussed more in Chapter 3. The ratios that I have used to generate each film are as follows:

Molecular monolayer: 300 mg MoS_2 exfoliation, 5 mL butanol, 10–50 µL nonvolatile molecule

Molecular bilayer: 300 mg MoS_2 exfoliation mixture, 5 mL butanol, 150+ µL nonvolatile molecules.

Assuming a yield of ~20% from exfoliation, approximately 60 mg of Mos_2 monolayers are recovered from exfoliation. To assemble a pure molecular bilayer, we need to include approximately 3 times the mass of the molecule relative to the MoS_2. Interestingly, a highly crystalline film containing a molecular monolayer can be formed at various mass ratios, suggesting that even a partially filled interlayer still produces a stable structure.

2.2.4 Characterization techniques

Cross-sectional TEM. The sample was prepared by depositing 5 LB layers of MoS_2-PEG solution onto a Si substrate, resulting in a superlattice that was approximately 200 nm thick. The sample was loaded into a ThermoFisher Quanta 3D FEG, and a cross section was prepared via focused ion beam milling to an approximate thickness of either 100 nm or 50 nm at an accelerating voltage of 5 kV under high vacuum. The cross section was placed onto an EM-Tec FIB lift-out grid by an Omniprobe micromanipulator, loaded into a Thermo Scientific Talos F200X transmission electron microscope and studied at room temperature under high vacuum at an accelerating voltage of 80 kV. Imaging at 200 kV was found to destroy the sample before an image could be captured. Images were analyzed via a Gatan Digital Micrograph v3.

X-ray diffraction (XRD). Superlattices prepared by LB deposition onto various substrates were characterized at room temperature in a Bragg–Brentano geometry typically across a range of 2q = 3–15° using Cu Kα (λ = 1.54056 Å) radiation with a Rigaku Smartlab diffractometer. Air scattering at low angles can be removed by fitting an exponential function ($Ce^{-x/a} + b$). To find the peak position, the peaks were fitted to a Lorentzian function via Origin 2018b.

Temperature-dependent XRD. The sample was prepared by depositing 7 LB layers of MoS_2-DMPU onto a Si substrate. Characterization was performed in a Bragg–Brentano geometry across a range of 6–20° using Cu Kα radiation (λ = 1.54056 Å) in a PANanalytic Empyrean diffractometer equipped with an HTK-1200 N (Anton-Paar) high-temperature oven chamber under an argon atmosphere. The temperature was ramped from room temperature (29°C) to 300°C at a rate of 4°C/minute. The sample was held at 300°C for 20 minutes and then cooled at a rate of -4°C/minute.

Ambient photoluminescence (PL) and Raman spectroscopy. The sample was prepared by depositing 10 LB layers of MoS_2-DMPU onto a quartz substrate. Photoluminescence measurements were collected on an Edinburgh Instruments FLS900 instrument equipped with a 450 W xenon lamp and a Czerny–Turner monochromator. Raman measurements were taken on a Horiba Jobin Yvon LabRam ARAMIS using a HeCd laser with an excitation wavelength of 442 nm. Annealing was a one-step process wherein the sample was heated to 300°C at a rate of 50°C/hour under argon and held for 12 hours before cooling back to room temperature at the same rate. The spectra were calibrated against a Si standard.

High-Pressure PL and Raman. The substrate was prepared by doctor blading polydimethylsiloxane (JB Weld Clear Silicone) onto a glass substrate and air curing for 24 hours before annealing at 150°C for 2 hours. The superlattice was prepared by depositing 5 LB layers of MoS_2-DMPU onto polydimethylsiloxane, and the substrate was cut away from the glass film and loaded into a diamond anvil cell (DAC, Almax EasyLab). The DAC used for these measurements is a Diacell Bragg Mini with a Boehler-Almax design consisting of Type II diamonds (3.3 mm/85 degree aperture, 16 sided, cutoff = 1 mm, (100)-oriented). Pressure monitoring was achieved by using the R_1 fluorescence shift of a ruby ($Al_2O_3:Cr^{3+}$) with 4:1 methanol-ethanol as the pressure medium to establish a calibration curve. For the measurements of the superlattices, a silicone substrate was used as the medium, and the film had direct contact with the diamond cutlet. Both PL and Raman measurements were collected on a Horiba Jobin Yvon LabRam ARAMIS using a HeCd laser with an excitation wavelength of 442 nm. Laser spikes on the PL spectra were manually removed for clarity. The spectra were calibrated against the Si peak of the substrate. Scans were conducted over 53 seconds.

Calibration of the pressure in the DAC. Using the Mao and Bell calibration[17], the pressure in the DAC was calculated from the ruby R_1 fluorescence peak position. The Mao and Bell calibration was developed by comparing the shift in the R_1 fluorescence peak to experimentally measured NaCl lattice parameters via the Decker isothermal equation of state[18]. As the pressure increases, the R_1 fluorescence peak redshifts according to the following equation:

$$P = \frac{A}{B} * [\left(\frac{1 + \Delta\lambda}{\lambda_0}\right)^B - 1]$$

where P = pressure (Mbar), λ = wavelength (nm) of the ruby R_1 line, λ_o = wavelength of the R_1 line at 0 pressure, A = 19.04 (Mbar) and B = 7.665. We observed a redshift of 0.78 nm (Figure S12) relative to atmospheric pressure (.0001 GPa), which is consistent with a pressure of 2.7 GPa.

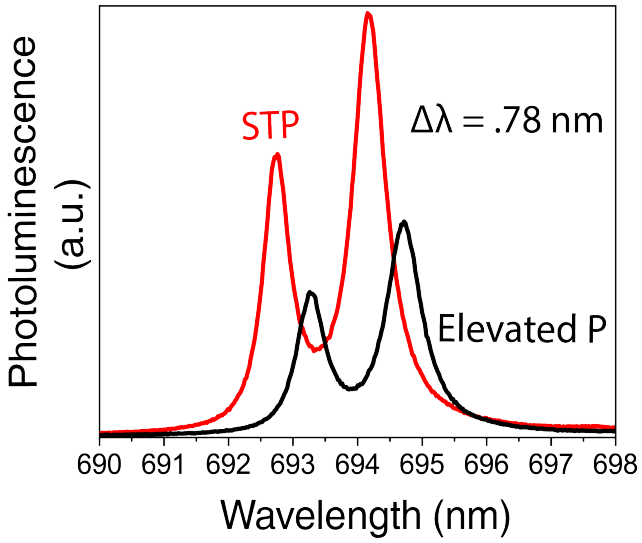


Figure 2: The ruby PL spectra used to calibrate the pressure in the DAC. Inside the DAC was a ruby that was used to calibrate the pressure. The ruby PL peaks showed a shift of 0.78 nm, which corresponds to a pressure of ~2.7 GPa using the Mao and Bell calibration equation.

Conductivity measurements. The sample was prepared by depositing 5 LB layers of MoS_2-DMPU onto 0.5 inch-width PTFE tape (TaegaSeal) wrapped around a microscope slide. Electrical contacts made of Cu foil were attached with conductive adhesive in a van der Pauw geometry. For electrical measurements, the PTFE was removed from the microscope slide and placed onto a 1 cm diameter steel die. The sample temperature was controlled by wrapping a heating tape around the steel die, with temperature feedback from a PID controller. Electrical measurements were taken on a Keithly 2636B sourcemeter. The DMPU was removed from the sample by annealing at 250°C for 1 hour under argon. The sample thickness was estimated via cross-sectional SEM imaging.

Pole figure XRD characterization of MoS_2-molecule superlattices. Pole figure XRD was used to probe the orientation of the sheets relative to the substrate. The sample was prepared by depositing 7 LB layers of MoS_2-DMPU onto a glass substrate. Measurements were taken on the peak at 2q

= 8.8°, in a Panalytical X'Pert PRO MRD HD XRD diffractometer using a Bragg–Brentano geometry with Cu Kα radiation (λ = 1.54056 Å). The low intensity above a χ angle of 2θ=15° indicated that the MoS_2 monolayers were highly oriented parallel to the normal of the substrate. We propose that this high degree of order is due to the liquid crystalline self-assembly mechanism.

XPS characterization of MoS_2-molecule superlattices. X-ray photoelectron spectroscopy (XPS) was used to verify the identity of the organic molecules in the superlattice. The sample was prepared by depositing 5 LB layers of MoS_2 and molecule solution onto a Si substrate. Superlattices were characterized via X-ray photoemission spectroscopy (XPS) via a Kratos Axis Ultra Delay-Line Detector spectrometer with a monochromatic Al Kα source. High-resolution XPS data were collected at a pass energy of 20 eV, and a charge neutralizer was used for charge compensation. All the data were corrected to the C 1 s peak at 284.6 eV.

2.3 Electrochemical intercalation of the superlattice

One of the main uses that we can envision for the superlattice material is as a filtration membrane. The basis of this idea comes from the work of Giem et al., who noted that restacked graphene is impermeable to even helium gas, whereas graphene that is exfoliated and restacked is reasonably permeable to a variety of fluids[19]. In that work, they explain this observation by noting the presence of bridging metal ions in the restacked graphene systems, which increase the graphene interlayer spacing enough that molecules of a sufficiently small kinetic diameter can fit inside the interlayer. Our superlattice system shares a marked similarity to this system, where MoS_2 monolayers are spaced by organic molecules. Additionally, our system may even have an advantage over graphene systems, as the molecular interlayer is much more capable of diffusion

than a metal ion due to the lack of strong interactions between the molecules and 2D materials. We repeated many of the experiments detailed in the previous work, where we sealed a custom aluminum container with a film assembled by vacuum filtration. The container was 13 mm in diameter, and the films were secured to the top of the container by two o-rings clamped between a vice.

To explore this idea, we attempted a variety of electrochemical experiments aimed at intercalating ions at low potentials. For our electrochemical experiments, we used a three-electrode setup consisting of a doctor bladed with MoS_2 on an aluminum foil working electrode, an aluminum counter electrode, and a reference Pt wire in a 1.6 M Ag/AgCl solution electrode. This setup was contained in a Teflon electrochemical cell, to which we added an electrolyte. In all of our experiments, we collected the open-circuit voltage for 15 minutes before performing any sweeps to allow the electrolyte to equilibrate with the reference electrode. For the linear sweep voltammetry (LSV) experiments, scans were conducted at a rate of 2 mV/s, typically from 0–1.5 V. The current was recorded over the last 50% of the step duration and averaged over 10 voltage steps. The resolution was 333.33 μV, corresponding to an E range of -10-10 V. The current range was set automatically by the software, and the bandwidth was 8. For the chronopotentiometry (CP) experiments, a 0.100 mA current was applied for a 48 hour scan. The upper cutoff limit for the sweep was 2 V, although no experiment ever climbed to a voltage that high.

2.4 Molecular dynamics simulations of the superlattice system

Simulation is a targeted way to gain an understanding of a certain property in a chemically interesting system. In chemistry, two broad types of calculations are often used to model systems: density functional theory (DFT)-based calculations and molecular dynamics (MD). In their

simplest forms, DFT-based calculations utilize quantum mechanical methods to determine the energy of electrons in a system, whereas MD uses a statistical mechanics-based approach to calculate the evolution of a system over time on the basis of various attractive and repulsive forces. While MD approaches modeling from a nonquantum perspective, it is a particularly useful type of simulation for determining the properties of large (1000 atoms) systems where DFT-based models take too much computational time to obtain results. It also has the distinct advantage of modeling dynamic behavior that occurs over long periods of time, whereas DFT-based calculations typically look at discrete points of a system.

To model many of the properties of the superlattice system, I used the LAMMPS software package, which is a molecular dynamics software from Sandia National Labs[20]. The LAMMPS documentation is well maintained and has a good user manual, which well explains how to use the different commands. Additionally, there is a responsive and large community that can help to troubleshoot individual issues simulation issues. The best way that I can recommend learning LAMMPS is to take old, working simulations and gradually modify them until they work in the way that is desired.

2.4.1 MD simulation parameters

For each type of simulation, we used a consistent set of carefully chosen simulation parameters. We used the MoS_2 force field developed by Pádua, Blankschtein, and coworkers, which was designed to accurately model the interfacial interaction between MoS_2 and organic molecules[21]. We paired the MoS_2 forcefield with the OPLS–AA forcefield[22] for organic molecules by using geometric combining rules for the LJ interactions. Long-range Coulombic interactions were accounted for via the particle–particle–mesh solver[23]. LJ interactions were cut off at 1.2 nm. A weighting component for interactions within bonded molecules was set as 0 for first- and

second-neighbor bonded atoms and as 0.5 for third-neighbor bonded atoms. Time integration was performed via Nosé–Hoover-style non-Hamiltonian equations of motion in the isothermal–isobaric (NPT) ensemble. Unless stated otherwise, simulations were typically performed under hydrostatic pressure at 1 atm. Simulations were performed with an accuracy of 10^{-5} in energy, except for solvation energy calculations, which were performed at 10^{-6}. The SHAKE algorithm was applied to H atoms with an integration time step of 1 fs[24]. The simulation boxes were prepared using fftool[25] and packmol[26].

2.4.2 Simulation box setup

Prior to running calculations in LAMMPS, it is first necessary to set up a simulation box. Unlike in DFT-based methods, the simulation size is often quite large, and the system is often not a perfect crystal. This makes the initial geometry quite important, as setting up an unrealistic starting geometry often causes the simulation box to "explode". This is because we typically use an NPT ensemble, so the simulation volume is not held constant. When atoms in an unrealistic geometry check the forces of nearby atoms at each timestep, there will be a strong repulsive set of interactions that the simulation box will counteract by expanding in volume. If this expansion in volume does not relieve unrealistic forces, e.g., because a solvent molecule is trapped inside an MoS_2 monolayer, then large repulsive interactions will still be calculated and the box will expand again until the pressure is relieved. If this pressure is never relieved, the simulation box continues expanding until the simulation crashes. When viewed as a movie, the volume expansion will naturally be filled by solvent molecules, and the simulation box will seemingly explode.

To set up an initial starting geometry, I found it most useful to use packmol and fftool, a set of python scripts that pack molecules into a simulation box, write out LAMMPS input files, and very quickly check that the initial geometry is somewhat realistic. The packmol software

works by packing molecules into predefined regions of space in a simulation box, which allows for high control over the exact simulation box setup. After running packmol, fftool writes out LAMMPS compatible input files on the basis of the packmol simulation box. A typical simulation setup, annotated below, using packmol looks like this:

```
tolerance 2.5                  # minimum distance (Å) between molecules of the same type
filetype xyz                   # output file type
output simbox.xyz              # output file name

structure MoS2.xyz                        # .xyz file name of molecule 1
  number 1                                # number of molecule 1
  center                                  # fix center command
  fixed 75.8496 76.636 2.0 0 0 0          # xyz coordinates of the center of molecule 1
end structure                             # go to molecule 2

structure DMPU.xyz                        # .xyz file name of molecule 2
  number 420                              # number of molecule 2
  inside box 2.44 1.78 3 148 153.22 11    # pack inside a box bordered by
end structure                             # go to molecule 3
```

This code outputs a simulation box containing 421 “molecules”, 1 molecule given by the structure file MoS2.xyz, and 420 molecules given by the structure file DMPU.xyz. In the simulation box, first, the MoS2.xyz file is centered at the coordinates given in the code, and then the 420 DMPU.xyz molecules are randomly packed into the simulation box bordered by the coordinates given above. In addition, the tolerance command (2.5) ensures that no two atoms on different molecules are closer together than 2.5 Å, thus limiting the potential for unphysical geometries. If packmol fails to build a simulation box within ~100 iterations, then most likely, the packmol input file is unrealistic in some way. The most common error that I often ran into was trying to pack too many molecules into a volume that was too small, where the tolerance command did not allow for possible packing without neighbors being too close together. After packmol outputs the file simbox.xyz, I recommend checking the simbox in visualization software, such as VESTA, to

ensure that the simulation is packed properly. Simulation boxes prepared properly can then be used in a variety of analyses after an appropriate equilibration step.

2.4.3 Simulations to calculate potential energy surfaces

Umbrella sampling is a powerful sampling technique that allows for the collection of data in complex physical systems[27]. Particularly in systems with complex potential energy surfaces, Monte Carlo sampling methods are often unable to adequately sample the entirety of the phase space, as there are difficulties in overcoming large energy barriers (i.e., sampling through unfavorable transition states). Umbrella sampling techniques allow for the entirety of the phase space to be measured by applying a bias, which encourages configurations that are difficult to sample. In our simulations to produce a potential energy surface for the assembly of the superlattice system, we performed potential of mean force (PMF) calculations via the COLVARS module[28] in LAMMPS, where we measured the force applied to springs attached to MoS_2 sheets as they approached the solvent. We then analyzed the output via a weighted histogram analysis method (WHAM)[29].

To perform the PMF calculations, simulation boxes with two AB-stacked MoS_2 monolayers in a parallel orientation were created. To minimize edge effects, the monolayers had a hexagonal shape. Each hexagon was 4.1 nm edge-to-edge. The sheets were solvated by either DMPU or 15-crown-5 in a 7 by 7 by 9 nm box. The simulations began with the center of mass-to-center of mass (hereafter, center-to-center distance) at separations of 1.0, 1.5, 2.0, 2.5, 3.0, 3.5, and 4.0 nm. Prior to beginning a PMF simulation, the simulation box was annealed at 400°C for 5 ns while holding the MoS_2 sheets in their starting position via a spring/self restraint. During the course of the PMF calculation, the two MoS_2 sheets were maintained in a close-to-parallel orientation by using spring restraints on each layer. For both sheets, a spring/self restraint was

used to restrain movement on a per-atom basis, with a value of 120,000 kcal/mol/Å^2. This ensured that the sheets remained highly coplanar. For the bottom sheet, the restraint was applied to the x, y, and z directions of movement. For the top sheet, the restraint was applied only to the x and y directions of movement. This allowed the top sheet to move toward or away from the bottom sheet while maintaining AB stacking.

The COLVARS module[28] in LAMMPS was used for PMF simulations. These tests were performed in both the forward (pulling MoS_2 together) and reverse (pushing MoS_2 apart) directions to test for hysteresis. In our simulations, each MoS_2 flake lay in the x–y plane and was moved together or apart in the z direction. The simulations explored MoS_2 center-to-center separations from 4 nm to 0.4 nm, where 0.62 nm is the expected interlayer distance for bulk MoS_2. A smaller force constant of 300 kcal/mol/Å^2 was used for larger separations (4 nm to 1.5 nm), whereas a higher force constant of 3000 kcal/mol/Å^2 was required for smaller separations (1.8 nm to 0.4 nm). For larger separations, sampling was performed every 0.1 Å, whereas for smaller separations, sampling was performed every 0.025 Å. Each position was sampled for 1.5 million timesteps (equivalent to 1.5 ns). Trajectory information was recorded every five timesteps.

To calculate a free energy surface, we used the python implementation of BayesWHAM[29]. For each 1.5-ns sampling of a position, we excluded the first 30% of the timesteps. The removal of the first 30% of the timesteps was necessary to minimize hysteresis between PMF simulations performed in the forward and backward directions. For the WHAM analysis, binning was performed along the z-axis with a bin width of 0.001 Å. WHAM calculations converged to 10^{-15}.

2.4.4 Simulations to calculate diffusion coefficients

Diffusion calculations are one of the simplest types of measurements that can be collected via MD software. In a system that is assumed to be randomly moving (e.g., owing to Brownian

motion), the mean squared displacement (MSD) of a given body in that system increases with time. Mathematically, the MSD in a one-dimensional system is defined by the position of a body at time t (x(t)) relative to its starting position ((x(0)):

$$\text{MSD} = \langle (x(t) - x(0))^2 \rangle$$

For a particle in an n-dimensional system, the MSD can therefore be defined as:

$$\text{MSD} = 2nDt$$

where D is the diffusion coefficient and t is the time over which the random walk occurs. Molecular dynamics software works by calculating the trajectories of atoms, which in turn outputs a position for each timestep of the simulation. By time averaging the position of atoms within a system, MD software can output MSD on the basis of a starting position for every atom.

In all the simulations, periodic boundary conditions were used, and the center of mass for each molecule was used to calculate the MSD. For the simulations of the bulk liquid, 1800–2000 solvent molecules were packed into a 6 × 6 × 6 nm simulation box and allowed to equilibrate at the desired temperature for 5 ns before running. For simulations of confined liquids, a bilayer of 10 × 10 nm MoS_2 sheets was separated by 10 Å and packed with a monolayer of molecules above each monolayer, typically between 160 and 200 molecules, depending on the exact molecular size. To one side of this lattice, an additional 600–1000 molecules were packed into a 100 × 40 × 20 Å well to allow equilibration and ensure that the interlayer packing was thermodynamically ideal. These simulations were allowed to equilibrate at 500°C for 10 ns prior to running before being cooled to the desired temperature and equilibrated for another 10 ns. The MSD was calculated for atoms that started within a 60 × 60 Å box centered in the middle of the MoS_2 layers. The simulations were run until the MSD plateaued, which took variable amounts of time for different temperature simulations. In particular, low-temperature simulations often take many more

timesteps to equilibrate than high-temperature simulations do. In these simulations, there are two important differences from bulk simulations. First, anisotropic box expansion was allowed to account for the anisotropy of the simulation box. If isotropic box expansion was allowed, the simulations would often crash. Second, when processing the data, it was assumed that all the atoms only diffused in 2 dimensions as they could not move through the MoS_2 sheets, so n = 2 rather than 3 when the diffusion coefficient was solved for.

2.4.5 Simulations to calculate solvation energies

In addition to calculating physical properties, MD was also used to calculate solvation energies, both for MoS_2 layers in solvent and for solvent molecules confined in 2 dimensions between the layers. In molecular dynamics, a common way to calculate the energies of dynamic processes is the method of free energy perturbation (FEP). Using this method, the energy of the system is separated into three different terms: the background energy of nonchanging components (U_{bg}), a reference term corresponding to the energy of the atoms before perturbation (U_0), and a final term corresponding to the energy of the interactions after perturbation (U_1). As the energy of the system is varied by a factor of λ, the total energy of the system can be defined as:

(1) $U(\lambda) = U_{bg} + U_1(\lambda) + U_0(\lambda)$ and when

(2) $\lambda = 0$, $U = U_{bg} + U_0$ and when

(3) $\lambda = 1$, $U = U_{bg} + U_1$

Essentially, in an FEP calculation, the energy of the system is examined as a function of the λ coupling parameter, and by using thermodynamic integration over that range of λ values, the energy for a certain process can be extracted. Specifically, to calculate the solvation energy of MoS_2, we used an alchemical decoupling approach in LAMMPS via scripts provided by Vikram Khanna[30]. This approach calculates the free energy for removing a solute (MoS_2) from a solvent

(DMPU or 15-crown-5) into the gas phase. As our forcefields had two components, the coupling parameter (λ) is specified for both the LJ and coulombic interactions. Essentially, the energy of a given interaction in the system is broken up into 2 components:

$$U_{total} = U_{LJ} + U_{coul}$$

However, to isolate each component, we run two sets of simulations. In one set of simulations, the LJ λ is scaled from 0 to 1, and the coulombic component for the forcefield is turned off to isolate only LJ interactions. To isolate coulombic interactions, the simulation is run in two parts. First, the LJ component was scaled from 0 to 1 to obtain an accurate system geometry. Second, the simulation is rerun following the dump file with the LJ interactions turned off and the coulombic interactions scaled from 0-1. The system energy is analyzed via free energy perturbation[31] and thermodynamic integration[32] with a Gauss–Legendre quadrature.

In the solvation energy calculations, a single MoS_2 sheet was solvated. The monolayer size was 3.8 by 4.2 nm and contained 546 atoms. The MoS_2 was solvated by 266 molecules of DMPU or 160 molecules of 15-crown-5. The MoS_2 sheet spanned the full x-y dimensions of the simulation and was bonded to the MoS_2 in adjoining cells via periodic boundary conditions. The z-dimension of the cell started at ~33 Å (when MoS_2 was fully decoupled) and expanded to ~40 Å (when MoS_2 was fully coupled). The constrained size on the x-y plane combined with the expansion on z led us to decouple the x, y, and z dimensions of pressure. Specifically, for the NPT ensemble, we select the "aniso" barostat setting in LAMMPS, which means that the x, y, and z dimensions are controlled independently via the P_{xx}, P_{yy}, and P_{zz} components of the stress tensor. If these were not decoupled, the simulation cell would be unable to expand in z because of the limited in-plane expansion of the MoS_2 sheet. Because of the large expansion of the cell during solvation, we also calculated the pressure–volume work of expansion. We found that this

contribution was small (approximately 1/1000 of the solvation energy); we have corrected for this effect in our reported solvation energy.

For calculations of the MoS_2-solvent solvation energy, we used the recently described decoupling approach in LAMMPS[30]. The same parameters as noted above were used for these calculations. All the systems were equilibrated for 10 ns, followed by a production run of 8 ns for each LJ or coulombic decoupling calculation. For DMPU, LJ integration was performed via three Gauss–Legendre quadratures (7 points from 0-0.18, 20 points from 0.18-0.22, and 13 points from 0.22-1), and coulombic integration was performed via one quadrature (8 points from 0-1). For 15-crown-5, LJ integration was performed via three Gauss–Legendre quadratures (6 points from 0-0.13, 17 points from 0.13-0.195, and 9 points from 0.195-1), and coulombic integration was performed via one quadrature (8 points from 0-1). We performed each decoupling calculation three times with different initial solvent velocities by varying the seed parameters. We use these results to calculate an average and standard deviation for each solvation energy. The simulations were run at 400 K.

For calculations of the solvent-solvent solvation energy, 3D solvation energies were calculated in simulation boxes containing 1800 molecules utilizing the same simulation parameters as above, with the exception of an isotropic barostat setting, as MoS_2 breaking the isotropic symmetry of the simulation was no longer a problem. For 2D solvation energies, the greatest difficulty lies in achieving proper interlayer packing. The fundamental problem with attempting to calculate a 2D solvation energy lies in how the solvation energy relies on removing a molecule into the gas phase. In a simulation set up in an identical way to the diffusion calculation, with a well of bulk liquid equilibrating the interlayer, removing a molecule from the interlayer faces a problem where a molecule from the bulk will simply intercalate to fill the void left by the

disappearance of the molecule. To address this problem, we had to remove the ability of the well to intercalate molecules, but that required the precise packing of the interlayer with the correct number of molecules. If the interlayer ends up overpacked with too many molecules, the energy given by an FEP calculation would be unrealistic, as the removal of a molecule would alleviate the compression caused by overpacking. We found that systematically underpacking the interlayer led to convergence, where the molecules remained together in the middle of the two MoS_2 layers. As shown in Figure 3, when the interlayer is overfilled with molecules, the total solvation energy is positive, indicating that the removal of a molecule results in a relaxation of the other molecules and a net decrease in the potential of the system. As we decrease the number of molecules, we find that the solvation energy converges, indicating that the underpacked interlayer, visualized in Figure 3, reasonably approximates a properly pack system.

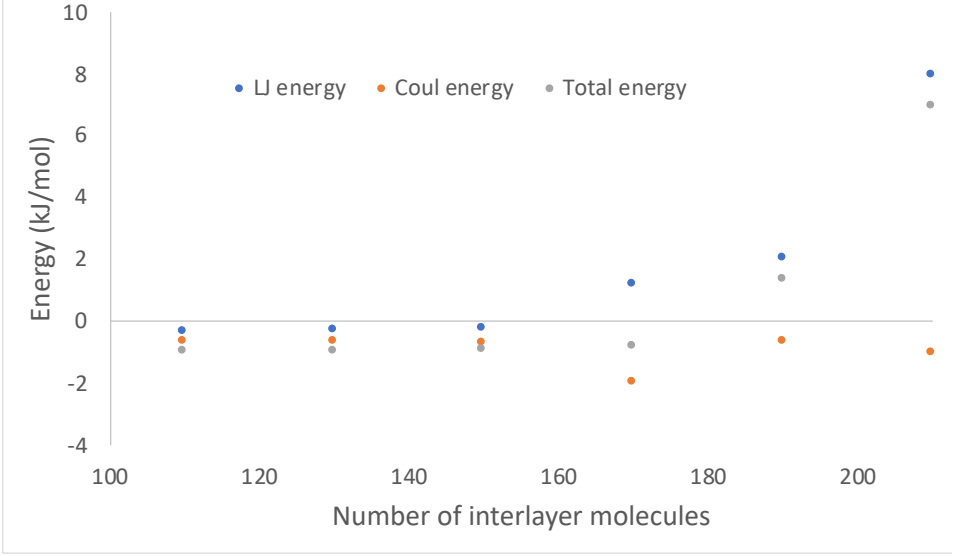


Figure 3: Convergence plot for solvation energy. As the number of interlayer molecules decreases, the solvation energy for both the LJ and coulombic components converge.

In these simulations, MoS_2 sheets were held apart at the corners by a self/spring restraint with a force constant of 500 kcal/mol/Å^2. Additionally, for the compute FEP command in both the LJ and coulombic components of the calculation, only the difference between the solvent

molecules was calculated. The interactions with both MoS_2 and the solvent were scaled by the λ parameter, but when the actual free energy perturbation command was enacted, only the solvent–solvent perturbation was calculated. By removing the coupling from MoS_2 from the FEP calculation, we hoped to isolate only the energy of the molecule–molecule interactions.

REFERENCES

(1) Duraisamy, S.; Ganguly, A.; Sharma, P. K.; Benson, J.; Davis, J.; Papakonstantinou, P. One-Step Hydrothermal Synthesis of Phase-Engineered MoS_2 /MoO_3 Electrocatalysts for Hydrogen Evolution Reaction. *ACS Appl. Nano Mater.* **2021**, *4* (3), 2642–2656. DOI: 10.1021/acsanm.0c03274.

(2) Liu, B.; Fathi, M.; Chen, L.; Abbas, A.; Ma, Y.; Zhou, C. Chemical Vapor Deposition Growth of Monolayer WSe2 with Tunable Device Characteristics and Growth Mechanism Study. *ACS Nano* **2015**, *9* (6), 6119–6127. DOI: 10.1021/acsnano.5b01301.

(3) Liu, H. F.; Wong, S. L.; Chi, D. Z. CVD Growth of MoS_2 -Based Two-Dimensional Materials. *Chem. Vap. Deposition* **2015**, *21* (10-11–12), 241–259. DOI: 10.1002/cvde.201500060.

(4) Novoselov, K. S.; Geim, A. K.; Morozov, S. V.; Jiang, D.; Zhang, Y.; Dubonos, S. V.; Grigorieva, I. V.; Firsov, A. A. Electric Field Effect in Atomically Thin Carbon Films. *Science* **2004**, *306* (5696), 666–669. DOI: 10.1126/science.1102896.

(5) Coleman, J. N.; Lotya, M.; O'Neill, A.; Bergin, S. D.; King, P. J.; Khan, U.; Young, K.; Gaucher, A.; De, S.; Smith, R. J.; Shvets, I. V.; Arora, S. K.; Stanton, G.; Kim, H.-Y.; Lee, K.; Kim, G. T.; Duesberg, G. S.; Hallam, T.; Boland, J. J.; Wang, J. J.; Donegan, J. F.; Grunlan, J. C.; Moriarty, G.; Shmeliov, A.; Nicholls, R. J.; Perkins, J. M.; Grieveson, E. M.; Theuwissen, K.; McComb, D. W.; Nellist, P. D.; Nicolosi, V. Two-Dimensional Nanosheets Produced by Liquid Exfoliation of Layered Materials. *Science* **2011**, *331* (6017), 568–571. DOI: 10.1126/science.1194975.

(6) Nicolosi, V.; Chhowalla, M.; Kanatzidis, M. G.; Strano, M. S.; Coleman, J. N. Liquid Exfoliation of Layered Materials. *Science* **2013**, *340* (6139), 1226419–1226419. DOI: 10.1126/science.1226419.

(7) Splendiani, A.; Sun, L.; Zhang, Y.; Li, T.; Kim, J.; Chim, C.-Y.; Galli, G.; Wang, F. Emerging Photoluminescence in Monolayer MoS2. *Nano Lett.* **2010**, *10* (4), 1271–1275. DOI: 10.1021/nl903868w.

(8) Eda, G.; Yamaguchi, H.; Voiry, D.; Fujita, T.; Chen, M.; Chhowalla, M. Photoluminescence from Chemically Exfoliated MoS2. *Nano Lett.* **2011**, *11* (12), 5111–5116. DOI: 10.1021/nl201874w.

(9) Divigalpitiya, W. M.; Frindt, R. F.; Morrison, S. R. Inclusion Systems of Organic Molecules in Restacked Single-Layer Molybdenum Disulfide. *Science* **1989**, *246* (4928), 369–371. DOI: 10.1126/science.246.4928.369.

(10) Kim, J. E.; Han, T. H.; Lee, S. H.; Kim, J. Y.; Ahn, C. W.; Yun, J. M.; Kim, S. O. Graphene Oxide Liquid Crystals. *Angew. Chem. Int. Ed* **2011**, *50* (13), 3043–3047. DOI: 10.1002/anie.201004692.

(11) Zhu, X.; Su, Z.; Wu, C.; Cong, H.; Ai, X.; Yang, H.; Qian, J. Exfoliation of MoS2 Nanosheets Enabled by a Redox-Potential-Matched Chemical Lithiation Reaction. *Nano Lett.* **2022**, *22* (7), 2956–2963. DOI: 10.1021/acs.nanolett.2c00148.

(12) Chou, S. S.; Huang, Y.-K.; Kim, J.; Kaehr, B.; Foley, B. M.; Lu, P.; Dykstra, C.; Hopkins, P. E.; Brinker, C. J.; Huang, J.; Dravid, V. P. Controlling the Metal to Semiconductor Transition of MoS2 and WS2 in Solution. *J. Am. Chem. Soc.* **2015**, *137* (5), 1742–1745. DOI: 10.1021/ja5107145.

(13) Sim, D. M.; Han, H. J.; Yim, S.; Choi, M.-J.; Jeon, J.; Jung, Y. S. Long-Term Stable 2H-MoS2 Dispersion: Critical Role of Solvent for Simultaneous Phase Restoration and Surface Functionalization of Liquid-Exfoliated MoS2. *ACS Omega* **2017**, *2* (8), 4678–4687. DOI: 10.1021/acsomega.7b00841.

(14) Kuo, D.-Y.; Cossairt, B. M. Direct Intercalation of MoS2 and WS2 Thin Films by Vacuum Filtration. *Mater. Horiz.* **2022**, *9* (1), 360–367. DOI: 10.1039/d1mh01193f.

(15) Li, X.; Zhang, L.; Wang, X.; Shimoyama, I.; Sun, X.; Seo, W.-S.; Dai, H. Langmuir-Blodgett Assembly of Densely Aligned Single-Walled Carbon Nanotubes from Bulk Materials. *J. Am. Chem. Soc.* **2007**, *129* (16), 4890–4891. DOI: 10.1021/ja071114e.

(16) Zheng, Q.; Ip, W. H.; Lin, X.; Yousefi, N.; Yeung, K. K.; Li, Z.; Kim, J.-K. Transparent Conductive Films Consisting of Ultralarge Graphene Sheets Produced by Langmuir-Blodgett Assembly. *ACS Nano* **2011**, *5* (7), 6039–6051. DOI: 10.1021/nn2018683.

(17) Mao, H. K.; Xu, J.; Bell, P. M. Calibration of the Ruby Pressure Gauge to 800 Kbar under Quasi-Hydrostatic Conditions. *J. Geophys. Res.* **1986**, *91* (B5), 4673. DOI: 10.1029/JB091iB05p04673.

(18) Decker, D. L. High-pressure Equation of State for Nacl, Kcl, and Cscl. *J. Appl. Phys.* **1971**, *42* (8), 3239–3244. DOI: 10.1063/1.1660714.

(19) Nair, R. R.; Wu, H. A.; Jayaram, P. N.; Grigorieva, I. V.; Geim, A. K. Unimpeded Permeation of Water through Helium-Leak-Tight Graphene-Based Membranes. *Science* **2012**, *335* (6067), 442–444. DOI: 10.1126/science.1211694.

(20) Thompson, A. P.; Aktulga, H. M.; Berger, R.; Bolintineanu, D. S.; Brown, W. M.; Crozier, P. S.; in 't Veld, P. J.; Kohlmeyer, A.; Moore, S. G.; Nguyen, T. D.; Shan, R.; Stevens, M. J.; Tranchida, J.; Trott, C.; Plimpton, S. J. LAMMPS - a Flexible Simulation Tool for Particle-Based Materials Modeling at the Atomic, Meso, and Continuum Scales. *Comput. Phys. Commun.* **2022**, *271*, 108171. DOI: 10.1016/j.cpc.2021.108171.

(21) Sresht, V.; Govind Rajan, A.; Bordes, E.; Strano, M. S.; Pádua, A. A. H.; Blankschtein, D. Quantitative Modeling of MoS_2 –Solvent Interfaces: Predicting Contact Angles and

Exfoliation Performance Using Molecular Dynamics. *J. Phys. Chem. C* **2017**, *121* (16), 9022–9031. DOI: 10.1021/acs.jpcc.7b00484.

(22) Jorgensen, W. L.; Maxwell, D. S.; Tirado-Rives, J. Development and Testing of the OPLS All-Atom Force Field on Conformational Energetics and Properties of Organic Liquids. *J. Am. Chem. Soc.* **1996**, *118* (45), 11225–11236. DOI: 10.1021/ja9621760.

(23) Hockney, R. W.; Eastwood, J. W. *Computer Simulation Using Particles*; CRC Press, 2021. DOI: 10.1201/9780367806934.

(24) Ryckaert, J.-P.; Ciccotti, G.; Berendsen, H. J. C. Numerical Integration of the Cartesian Equations of Motion of a System with Constraints: Molecular Dynamics of n-Alkanes. *J. Comput. Phys.* **1977**, *23* (3), 327–341. DOI: 10.1016/0021-9991(77)90098-5.

(25) Padua, A. *Fftool*; Zenodo, 2015.

(26) Martínez, L.; Andrade, R.; Birgin, E. G.; Martínez, J. M. PACKMOL: A Package for Building Initial Configurations for Molecular Dynamics Simulations. *J. Comput. Chem.* **2009**, *30* (13), 2157–2164. DOI: 10.1002/jcc.21224.

(27) Torrie, G. M.; Valleau, J. P. Nonphysical Sampling Distributions in Monte Carlo Free-Energy Estimation: Umbrella Sampling. *J. Comput. Phys.* **1977**, *23* (2), 187–199. DOI: 10.1016/0021-9991(77)90121-8.

(28) Fiorin, G.; Klein, M. L.; Hénin, J. Using Collective Variables to Drive Molecular Dynamics Simulations. *Mol. Phys.* **2013**, *111* (22–23), 3345–3362. DOI: 10.1080/00268976.2013.813594.

(29) Ferguson, A. L. BayesWHAM: A Bayesian Approach for Free Energy Estimation, Reweighting, and Uncertainty Quantification in the Weighted Histogram Analysis Method. *J. Comput. Chem.* **2017**, *38* (18), 1583–1605. DOI: 10.1002/jcc.24800.

(30) Khanna, V.; Monroe, J. I.; Doherty, M. F.; Peters, B. Performing Solvation Free Energy Calculations in LAMMPS Using the Decoupling Approach. *J. Comput. Aided Mol. Des.* **2020**, *34* (6), 641–646. DOI: 10.1007/s10822-020-00303-3.

(31) Zwanzig, R. W. High-Temperature Equation of State by a Perturbation Method. I. Nonpolar Gases. *J. Chem. Phys.* **1954**, *22* (8), 1420. DOI: 10.1063/1.1740409.

CHAPTER THREE – ASSEMBLY, MECHANISTIC INVESTIGATION, AND PROPERTIES OF 2D MATERIAL-MOLECULE SUPERLATTICE

Introduction

The synthesis of structurally precise materials that combine diverse building blocks will accelerate the development of artificial solids for electronics, energy, and medicine. Here we utilize simulation to identify how organic molecules can self-assemble with 2D materials into periodic superlattices with alternating layers of molecules and 2D monolayers. We experimentally demonstrate the generalizability of this mechanism by applying it to 2D semiconductors and various organic molecules or polymers. The resulting superlattices have unique and well-defined lattice constants that depend on the dimensions of the organic species. We are able to design superlattices with a wide variety of molecules (photoresponsive, chelating, light-emitting moieties), suggesting that the self-assembly does not depend on any specific chemical interaction yet can accommodate chemically diverse functional groups. We also observe that the 2D materials within the superlattices (MoS_2, WSe_2) remain quantum confined, even though the superlattice retains excellent electrical conductivity. This introduction of a mechanism and its experimental realization yield a general design strategy for a large class of quantum-confined, molecule-2D hybrid materials.

Since the pioneering studies of DiSalvo in the 1970s[1–3], there has been widespread interest in layered solids that contain small molecules. In DiSalvo's early studies, these were produced by intercalation of amines and phosphines into metal dichalcogenides, such as TaS_2 and NbS_2 to produce superlattices that are metallic but become superconductors at low temperatures[1,3]. Later

work on the intercalation of ions led to the development of many essential battery materials that are now widely used[4–6]. There has also been strong recent interest in the design of superlattices by intercalating ions[7,8] which have yielded optoelectronic and energy-storage materials that combine features from both the ions and layered materials[9–13]. With the emergence of tools for restacking 2D materials, it has even become possible to design superlattices of 2D materials and 2D polymers via mechanical stacking[14,15].

Across much of this earlier work, two broad challenges for the design of superlattices exist. First, many chemically interesting molecules cannot be intercalated. Intercalation into layered van der Waals solids is driven by charge transfer, and nearly always the intercalating species is an ion[16]. Even in DiSalvo's initial studies where it seemed that uncharged small molecules had intercalated[1], it was later revealed that the intercalation conditions (often >150 °C) caused decomposition reactions that yielded ammonium or phosphonium ions, and that it was these or related ions that intercalated[17–19]. Indeed, when interesting properties such as superconductivity were observed, they were often a result of charge transfer doping via intercalated ions[20–22]. The second broad challenge is that, across nearly all of the earlier work, intercalation causes the layered material to become metallic. This is noted, for example, in the widely studied conversion of MoS_2 from its 2H (semiconducting) to 1T (metallic) form[23,24]. In general, when an ion intercalates, the layered material becomes highly reduced or oxidized, causing the semiconducting material to either become degenerately doped or metallic[16,25].

To design superlattices that contain a wider variety of chemistries or to include 2D materials that are non-metallic, a different design strategy than intercalation may be required. In the 1980s, an intriguing strategy for incorporating uncharged molecules into superlattices was discovered. It was found that 1T (metallic) MoS_2 monolayers could be self-assembled with

uncharged molecules at an oil-water interface, yielding superlattices (Figure 1A)[26,27]. This and related approaches have been extended to other metallic 2D materials[28,29], but because there was not a well-defined mechanism for the assembly process, the full potential of this method has remained unclear.

Simulations of liquid suspensions of MoS_2 have, however, hinted at a possible mechanism for superlattice formation[30]. In this earlier work, the stability of solvated MoS_2 monolayers was examined. In one simulation, two solvated MoS_2 monolayers, both held parallel to each other but separated by a liquid, were pulled together to explore the potential energy surface (similar to Figure 1B). As the MoS_2 layers approached, local minima in potential energy were found that correspond to just one or two molecular layers (Figure 1C, blue). Notably, the local minimum for one molecular layer occurred at a MoS_2-MoS_2 (sheet center-to-sheet center) separation of 10 Å, which almost exactly matched the experimental d-spacing seen in the superlattices made by Morrison et al[26]. This correspondence suggests that this potential energy surface is relevant to the self-assembly mechanism. However, these simulations also found that the barrier to remove the last layer of molecules is lower than the barrier to remove the second-to-last layer of molecules. Thus, this potential energy surface predicts that superlattices with bilayers of molecules would be commonly observed when, in fact, all experiments to-date have yielded superlattices with just one molecular layer. Because of the absence of a mechanism for the self-assembly of superlattices, it remains unclear how large of a design space actually exists for the design of these superlattices.

To understand the limitations of the design space for these materials, we use molecular dynamics (MD) to explore the mechanism of self-assembly. Unlike earlier simulations, we calibrate our potential energy surfaces using the solvation energies of the 2D semiconductors. This improvement yields a qualitatively different potential energy surface. This new surface has a large

energy barrier to remove the final monolayer of solvent, in agreement with prior experiments. We use our simulations to propose a mechanism of self-assembly, and we then explore this mechanism and its generalizability. We find that a wide variety of uncharged small molecules and even polymers can be self-assembled into superlattices with semiconducting MoS_2 and WSe_2. Additionally, we further utilize our simulations to identify conditions that can trap two molecular layers between MoS_2 sheets, and we experimentally realize this predicted superlattice. We extensively characterize these novel semiconductor-molecule superlattices, revealing that the MoS_2 monolayers remain quantum confined despite being reassembled into solid state films. Moreover, despite the electronic isolation provided by the molecular layer, we find that electrons readily tunnel between MoS_2 layers, imparting a useful combination of electrical conductivity and quantum confinement. Thus, through this work, we demonstrate a generalizable mechanism for assembling exfoliated 2D materials with uncharged molecules into quantum confined but electrically conductive solids. Such materials may have wide importance in electronics, optics, energy, and medicine.

3.1 Simulations of MoS_2 aggregation in liquid

Entropy-driven ordering is a common phenomenon in evaporation-induced self-assembly[31]. When solvent is slowly removed, colloidal suspensions maximize system entropy by developing collective order[32–34]. For example, in concentrated liquid suspensions of 2D materials, it is often found that the 2D materials adopt parallel, coplanar orientations[32,34]. While it may seem that this ordering reduces entropy, in fact the parallel orientations provide added space for the 2D materials to move. Thus, during solvent evaporation, the loss of rotational entropy is more than compensated by increases in translational entropy.

Once the 2D sheets have adopted parallel orientations, further solvent evaporation simply decreases the average distance between sheets. For this reason, a simulation geometry in which two parallel MoS_2 sheets approach in the normal direction (Figure 1B) likely captures the final stages of evaporative self-assembly. Previous simulations[30] that explored the potential energy surface as the sheets approach revealed a local minimum at 10 Å (Figure 1C, blue), consistent with experimentally observed d-spacings of 10 Å for self-assembled superlattices. Although these simulations predicted the correct d-spacing, the activation energies of the transition states are inconsistent with experimental observations[26]. Specifically, the barrier between 15 and 10 Å is substantially higher than the barrier between 10 and 6 Å, raising questions about why experimental superlattices are only found with d-spacings of 10 Å.

This disagreement motivated us to revisit the earlier simulations and introduce additional steps to ensure the accuracy of the potential energy surface. We began by utilizing the same forcefields for MoS_2 and solvent (N-methyl pyrrolidone, NMP) as in the previous work[30]. Our simulation (Figure 1B) contained two hexagonal MoS_2 sheets with a 6-nm diameter. The sheets were pulled together in a potential of mean force (PMF) calculation from a center of sheet-to-center of sheet separation of 40 Å to 4 Å. Because the forcefield for MoS_2 was designed to model MoS_2-solvent interactions but not designed to model the out-of-plane bending of MoS_2, we adapted an earlier approach of adding empirical spring constraints to each MoS_2 sheet[30]. These constraints are intended to keep the two MoS_2 sheets parallel as they approach.

Although the qualitative agreement with experiment was exciting, we sought to obtain a better quantitative understanding of the system. Our inability to sample the transition state at 9 Å prevented us from relating the energy of desolvated MoS_2 (separation of 6 Å) to the energy of the solvated MoS_2 monolayers. To link these separate systems, we therefore developed a three-step

process. First, we calculated the potential energy surface as two monolayers were separated to a large distance in vacuum (Figure 1C, pink). Second, we calculated the potential energy surface for two parallel monolayers as they were pulled together in NMP (Figure 1C, purple). Third, we noted that, when the two monolayers are well separated (e.g., at 40 Å), the difference in energy between the two potential energy surfaces is just the solvation energy. We thus calculated the solvation energy of MoS_2 in NMP using an alchemical decoupling route in LAMMPS[35], which leveraged the same forcefields. We obtained a solvation energy of 7.4 meV/Å^2, thus yielding two potential energy surfaces whose relative energies have been calibrated.

Our new potential energy surfaces have several important features. We find that the

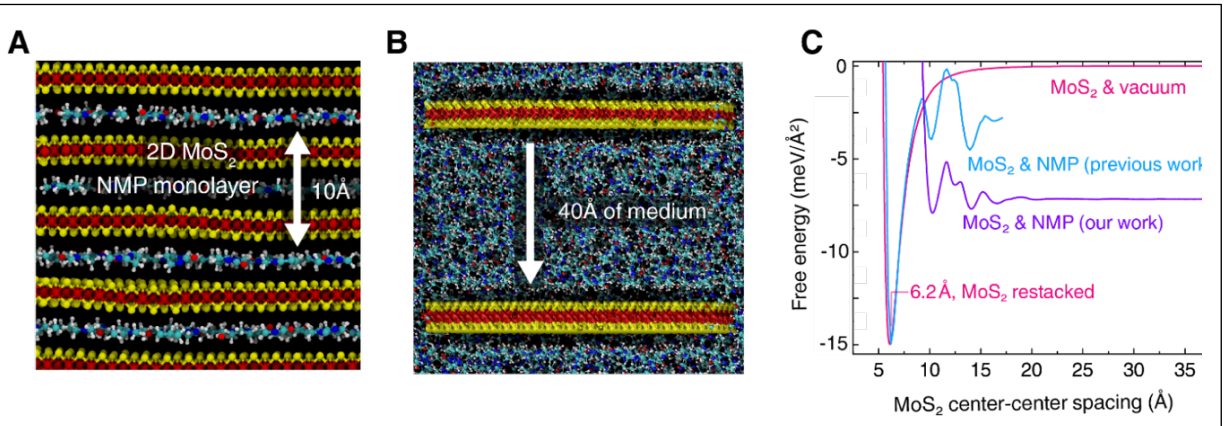


Figure 1: Calculating the superlattice potential energy surface. (A) Molecular dynamics simulation of a MoS_2-N-methyl-2-pyrollidone (NMP) superlattice, where monolayers of MoS_2 alternate with molecular monolayers. (B) Simulation geometry where two MoS_2 monolayers, initially separated by 40 Å of NMP, are pulled together in the normal direction. (C) Free energy surface of two MoS_2 monolayers at varying separations in vacuum (pink) or NMP (purple) calculated by us and in previous work (blue).

solvated MoS_2 monolayers are much less stable than fully desolvated, "bulk" MoS_2 (d = 6.2 Å). We observe a series of local minima in the potential energy surface (d = 10.3, 13.9, 16.4 Å), corresponding to one, two, and three molecular layers. There is also a local minimum at 12.2 Å, where the NMP stacks vertically rather than lies flat[30]. It was previously observed that similar molecules such as pyridine can also adopt a vertical stacking motif with a similar 12 Å d-

spacing[36]. The barriers separating these minima grow as the separation decreases, with the final barrier at d = 9.0 Å now being the largest. This result is consistent with experimental results, since the large barrier at d = 9.0 Å would explain the prevalence of superlattices with only a monolayer of solvent trapped within them.

We propose that the key for understanding the final stages of evaporative self-assembly lies in the local minima of the potential energy surface. These minima arise when the solvation shells from nearby MoS_2 sheets can interact. To understand how this occurs, we first describe the structure of the solvation shell around a single MoS_2 monolayer. The atomically flat MoS_2 surface provides a boundary for the adjacent solvent, holding the first layer of solvent at a uniform distance. The second layer of solvent can also be easily observed in simulations, although it is less well ordered. These layers can be observed by plotting the solvent density as a function of distance from the MoS_2 surface (Figure 2). Near the surface, the density oscillations are extremely large, and as distance from the surface increases, the oscillations decrease.

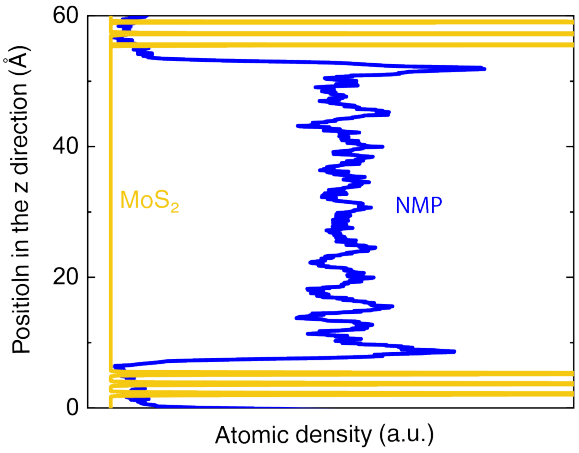


Figure 2: Density plot of MoS_2 solvated in NMP. The first layer of solvent around each MoS_2 is the most densely packed, while subsequent layers become less so.

The formation of molecular layers is compounded when two MoS_2 sheets are in close proximity. Each MoS_2 sheet forms a boundary so that density fluctuations extend from each surface. When an integer number of molecular layers can fit between sheets, the maxima in density fluctuations that extend from one surface are in registry with the maxima that extend from the

other surface, resulting in a local energy minimum. In contrast, for non-integer numbers of layers, molecular configurations that are less stable are now required to fill the available volume. Overall, the tendency for molecules to form layers near MoS_2 leads to certain MoS_2-MoS_2 separations being energetically favored.

Thus, we propose a general mechanism in which entropy driven ordering of MoS_2 sheets, in combination with the cooperative interactions of the solvation shells, leads to the self-assembly of superlattices. Importantly, because most molecules will form well-defined solvation shells, we suspect that similar potential energy surfaces will exist for many systems. This suggests that superlattice formation could generalize across a wide variety of 2D materials and molecules.

The primary objective of the PMF simulations was to calculate the free energy surface of two parallel MoS_2 monolayers as they approach each other within a solvent. These calculations (Figure 3) were inspired by the work from Pádua, Blankschtein, and coworkers that examined the exfoliation and reaggregation of MoS_2 in common solvents[30]. Our experimental and computational findings are qualitatively different from this earlier work, and we will discuss these differences later on.

In our simulations, we found that we could reproduce the earlier PMF calculations when weak spring constraints were used. However, we observed that this produced non-physical transition states in which both the MoS_2 and molecules exhibited unrealistic bond angles and lengths. Moreover, the potential energy

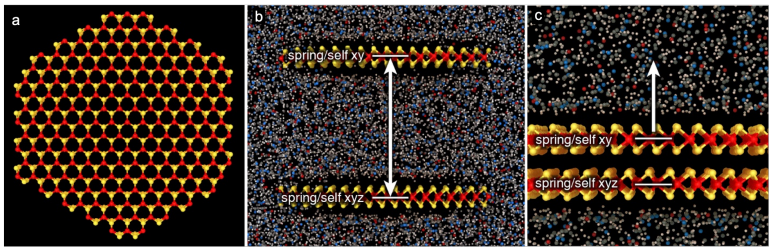


Figure 3: (A) Hexagonal MoS_2 sheet used for simulation. (B) Simulation geometry with two parallel sheets in an AB stacking sequence. The center-to-center distance is monitored during the simulation. (C) Simulation in which a bilayer is separated without allowing solvent to enter the interlayer space. This results in a separated bilayer with solvent on one side of each flake and vacuum on the other.

surfaces obtained from pulling the MoS_2 sheets together was markedly different from pushing them apart, indicating the simulations were non-ergodic. Because of the steepness of the free energy surface, we needed to increase the COLVARS force constant from 300 to 3000 kcal/mol/Å^2 to explore the potential energy surface for interlayer separations between 0.4 and 1.8 nm. When using smaller force constants, the MoS_2 flakes would not sample positions near the top of the barrier. An important consequence of this increased spring constant was that the final molecular layer would become trapped in the interlayer space. This trapping made it impossible to sample the transition state at 9 Å and thus we could not obtain the full potential energy surface. This interlayer separation corresponds to the transition between MoS_2 with and without a solvent monolayer. Because the sheets remained highly parallel, we observed that as soon as some solvent begins to be expelled from the monolayer, all solvent leaves. The complete loss of solvent causes the interlayer distance to decrease slightly. Then, because of this reduced distance, the solvent does not re-enter the interlayer space. This sudden transition causes incomplete sampling of the barrier at 9 Å. The result is that the data in this region are nonergodic and that the free energy surface in this region is discontinuous. More importantly, however, the trapping of a molecular monolayer was in excellent agreement with the superlattice formation. This agreement suggested that this updated simulation was now relevant to the experimental system.

3.1.1 Joining the free energy surfaces

Because our simulations resulted in a broken free energy surface between 8 and 9 Å, we developed an approach to determine the relative energy of the two surfaces so that they intersected at the correct position and energy. We initially envisioned a two-step approach for linking these two surfaces (Figure 4A). Although this approach allows us to connect broken surfaces, the specific pathway is challenging to carry out. We therefore used the approach from Figure 3, a, to

design two simpler steps that would be computationally tractable while yielding similar changes in free energy. This simplified approach is outlined in Figure 4, b and c.

In Step 1 (Figure 4A), a MoS_2 bilayer surrounded by solvent would be separated from 6.2 Å to 40 Å using a potential of mean force calculation. The simulation would prevent solvent from entering between the two MoS_2 sheets, yielding, at large separations, two MoS_2 monolayers that are surrounded by vacuum on one side and by solvent on the other.

We replaced this Step 1 with a simplified scheme (Figure 4B) that separates a MoS_2 bilayer but without solvent present. The long-range interaction of solvent through one MoS_2 layer to a second MoS_2 layer is expected to be negligible since the coulombic interaction is screened by the first MoS_2 layer and the Lennard-Jones interactions decay as r^6. This simplifying step allows us to use the previously calculated results

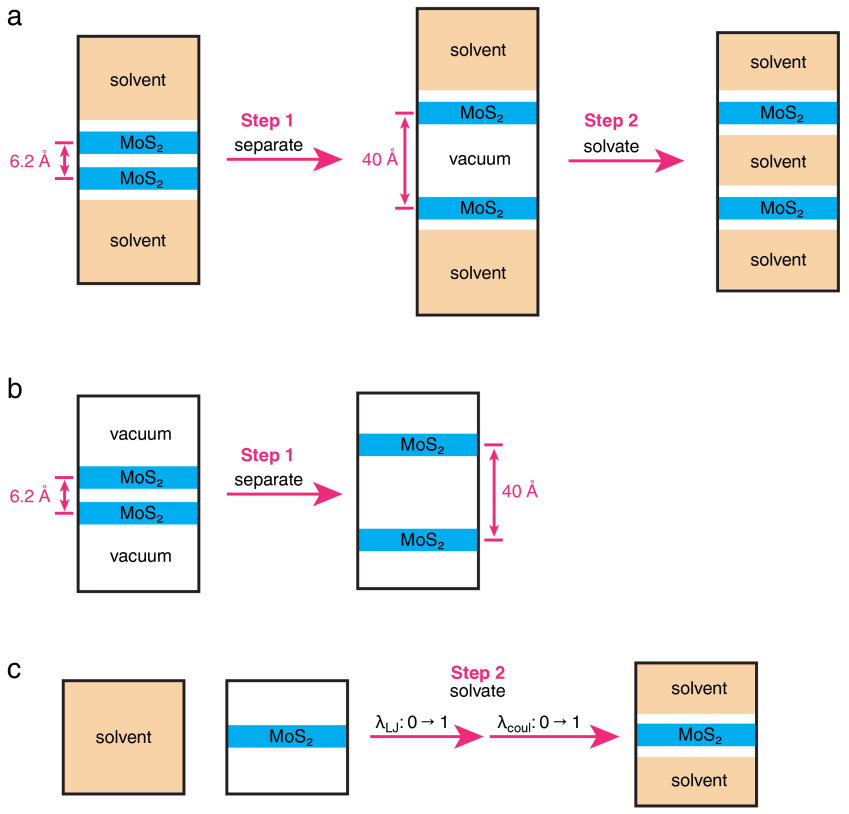


Figure 4: (A) Idealized two-step process for connecting the broken free energy surface. The goal of the calculation is to calculate the change in free energy for both steps. In step 1, a MoS_2 bilayer is separated and in step 2, the bilayer is solvated on both sides of each sheet. To make these two steps computationally tractable, this idealized two-step process is approximated by a new step 1 (B) in which a MoS_2 bilayer is separated in vacuum and by a new step 2 (C) in which a monolayer of MoS_2 is solvated on both sides.

for the separation of a MoS_2 bilayer.

The free energy surface obtained by the new Step 1 is identical to the broken free energy surface below a separation of 8 Å. Therefore, in Figure 1C, we use the free energy surface from the process of Figure 3B, which extends the surface to a separation of 40 Å.

In Step 2 of Figure 4A, we calculate the free energy to solvate one side of two MoS_2 monolayers. Because of the complexity of this calculation, we instead calculated the free energy to solvate both sides of one monolayer[35]. We further justify this approach by noting that the pairwise interactions that are formed during the half-solvation of two monolayers are nearly identical in number and magnitude to those formed during the full solvation of one monolayer.

Results for Step 1:

Step 1 (Figure 4B) yielded a continuous free energy surface that extended from an interlayer separation of 6.2 Å to 40 Å. This free energy surface was extended to smaller interlayer separations (~5 Å) by performing an additional compressive PMF simulation from 6.2 Å to 5 Å. The total change in energy from the minimum at 6.2 Å to 40 Å defines the surface energy of MoS_2. As reported previously, we find that the surface energy is 240 mJ/m^2, which is equivalent to 14.98 $meV/Å^2$. In this reported surface energy, the measured energy is divided by an area, where the area is the area of the MoS_2 where contact is being made (i.e., the area of the top of one MoS_2 monolayer and the area of the bottom of the other).

Results for Step 2:

Step 2 (Figure 4C) yielded solvation energies of -6.84 meV/Å^2 for DMPU and -6.34 meV/Å^2 for 15-crown-5. For clarity, we note that the MoS_2 area used for these calculations is based on the top and bottom surfaces of the MoS_2 monolayer – i.e., the total contact area that MoS_2 makes with the solvent. The specific results for the decoupling simulations of DMPU and 15-crown-5 are shown in Figure 5.

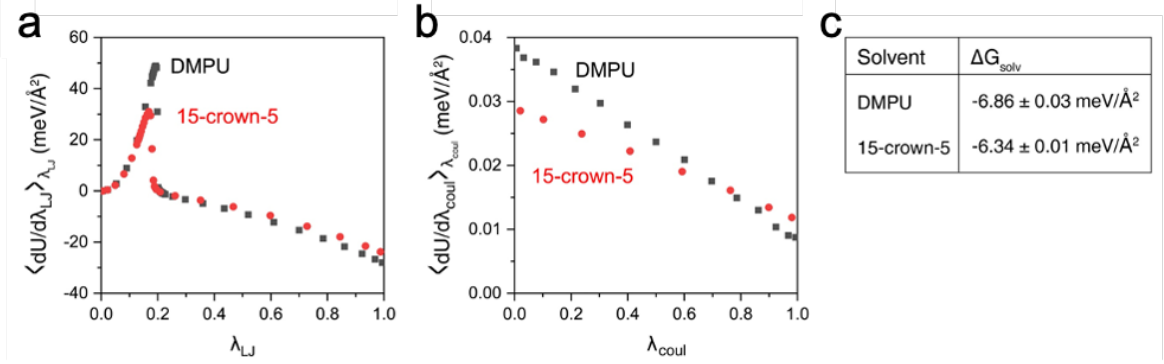


Figure 5: Decoupling approach for the calculation of solvation energy. First, the LJ interactions are turned on (A) and then the coulombic interactions are turned on (B). A Gauss-Legendre quadrature is used to integrate (A) and (B), yielding the solvation energy for MoS_2. Each of these calculations is performed three times to yield the mean and standard deviation (C).

The increased solvation energy of DMPU (-6.84 meV/Å^2) versus 15-crown-5 (-6.34 meV/Å^2) is consistent with our experimental observation that DMPU is a better solvent for MoS_2 than 15-crown-5. For comparison, we also note that the MoS_2 surface energy, as calculated from the MoS_2 forcefield[2], is 14.98 meV/Å^2 (equivalent to 240 mJ/m^2). For this surface energy, the area of MoS_2 is its total surface area (top and bottom surfaces), as is the case for solvation energy. Therefore, the surface energy and solvation energy can be compared on the same PMF plot using our two-step scheme to connect the PMF curves.

The result of this process is shown for the case of DMPU in Figure 6 and for both solvents in Figure 5B. The key outcome of this calculation is that the system (parallel MoS_2 sheets in DMPU) encounters free energy barriers of increasing magnitude as the distance between sheets decreases. The largest barrier occurs at ~9 Å, where the final monolayer of solvent is expelled (Figure 6). As shown by our experiments, this barrier is large enough to kinetically trap many superlattices with exactly one monolayer of solvent.

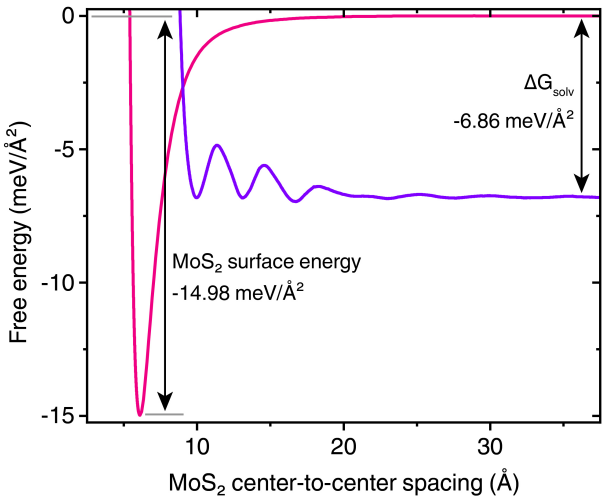


Figure 6: Free energy surface for two parallel MoS_2 sheets in DMPU as a function of the separation between the two sheets. The data is the same as in Figure 4B but contains additional annotations. The free energy surface for solvated MoS_2 is shown in purple. The free energy surface for the separation of a bilayer of MoS_2 in vacuum is shown in pink ("Step 1" of the two-step procedure). These two free energy surfaces are offset by an amount equal to the solvation energy of MoS_2 in DMPU, -6.86 meV/Å^2 ("Step 2" of the two-step procedure.)

Previous studies of the solvation shell of MoS_2 have yielded qualitatively different results[30]. Although earlier work surveyed several solvents (e.g., H_2O), only the solvent *N*-methyl pyrrolidone (NMP) had solubility characteristics similar to DMPU. In fact, NMP is similar in shape and size to DMPU, and therefore, we expected it to yield similar results for its free energy surface. However, earlier work[30] found that (1) the energy barrier at d = 9 Å (the barrier that separates the superlattice with a solvent monolayer from the bulk material) is smaller than the barrier at d = 12 Å (the barrier that separates the superlattice with solvent bilayer from that with the solvent monolayer), and (2) the free energy surface was fully continuous across all barriers.

Using DMPU, we were able to reproduce the earlier result only when we allowed the MoS_2 sheets to tilt away from a parallel orientation during the potential of mean force calculations. When the MoS_2 tilted more, the barriers became lower because the reported center-to-center spacing was no longer representative of the actual spacing for much of the MoS_2 sheet. In our simulations, allowing the MoS_2 to tilt caused the barrier heights to be systematically underestimated compared to the case where MoS_2 was held parallel.

Generation of the free energy surface:

Because the barrier heights were relatively large when we held the MoS_2 parallel, we also had to use a larger Colvars spring constant to sample the free energy surface. Then, because of this higher force constant, we had to sample the center-to-center separation every 0.025 Å rather than the 0.025 nm that was previously used[30]. From our simulations, the higher force constant, 10x higher sampling density, and corrections for nonergodicity between 8 and 9 Å were crucial factors in obtaining our free energy surfaces.

Experimentally, we observed that superlattices with solvent monolayers are the typical product of liquid crystalline self-assembly. This observation agrees with our finding that the removal of the solvent monolayer from the superlattice has a higher barrier than the transitions that occur at larger center-to-center separations. This observation also agrees with our model that the MoS_2 remains highly parallel during liquid crystalline assembly. Indeed, nonparallel orientations probably do not occur to an appreciable extent because the large size of MoS_2 sheets (100 nm to 1 micron) and limited flexibility of the MoS_2 monolayers should impose a natural geometric ("steric") limitation on tilting, especially when these large flakes are separated by just 1 to 2 nm. Because of this lack of tilting, the superlattices remain remarkably stable against the expulsion of solvent, despite the relatively high thermodynamic instability of the superlattice.

By averaging the density of each element in the z direction of a simulation over 10000 fs, we generated a plot of atomic density shown in Figure 2. As shown by the plot, the first layer from each MoS_2 monolayer is the most densely packed, and subsequent layers lose density as the distance from the monolayer increases.

In our experimental synthesis of the material, a volatile solvent (butanol) is also present. Our choice to exclude the butanol from these simulations is justified for several reasons:

- The potential energy surface of all molecules studied have the same general shape, with the first minimum at ca. 10 Å and the second at 14-15 Å. Whether butanol is present or not, the general shape of the surface is unlikely to change.
- Our experiments utilized a modest excess of the non-volatile molecule. The final films typically contained just 15-20 wt.% of the non-volatile organic molecule and 80-85 wt.% MoS_2, which is consistent with a phase-pure superlattice. However, the solutions used to self-assemble the superlattice had a 1:1 weight ratio of non-volatile organic molecule to MoS_2. Thus, during the final stages of self-assembly, the experiment likely contains little butanol.
- The experiments with 15-crown-5 yielded a bilayer superlattice with a d-spacing of 15.2 Å, close to the simulation's prediction of 15.0 Å. This agreement suggests that the calculated potential energy surface describes the self-assembly mechanism with reasonable accuracy to a distance of at least 15 Å. Thus, the calculated potential energy surface is relevant to the final stages of the self-assembly process.

3.2 Experimental assembly of a semiconducting superlattice

The results from the PMF calculations suggest a mechanism for superlattice assembly that does not depend on any specific chemical interactions. Therefore, we were motivated to explore the self-assembly of semiconducting superlattices rather than the metallic ones that have been exclusively studied to-date. To make our superlattices, we first needed to produce a high-purity suspension of MoS_2 monolayers. Our synthetic scheme began with generating a suspension of metallic monolayers (Figure 7B) via lithium intercalation into MoS_2 powder (Figure 7A) [4,24,26]. We followed this by refluxing the suspension to induce a phase change back to the 2H,

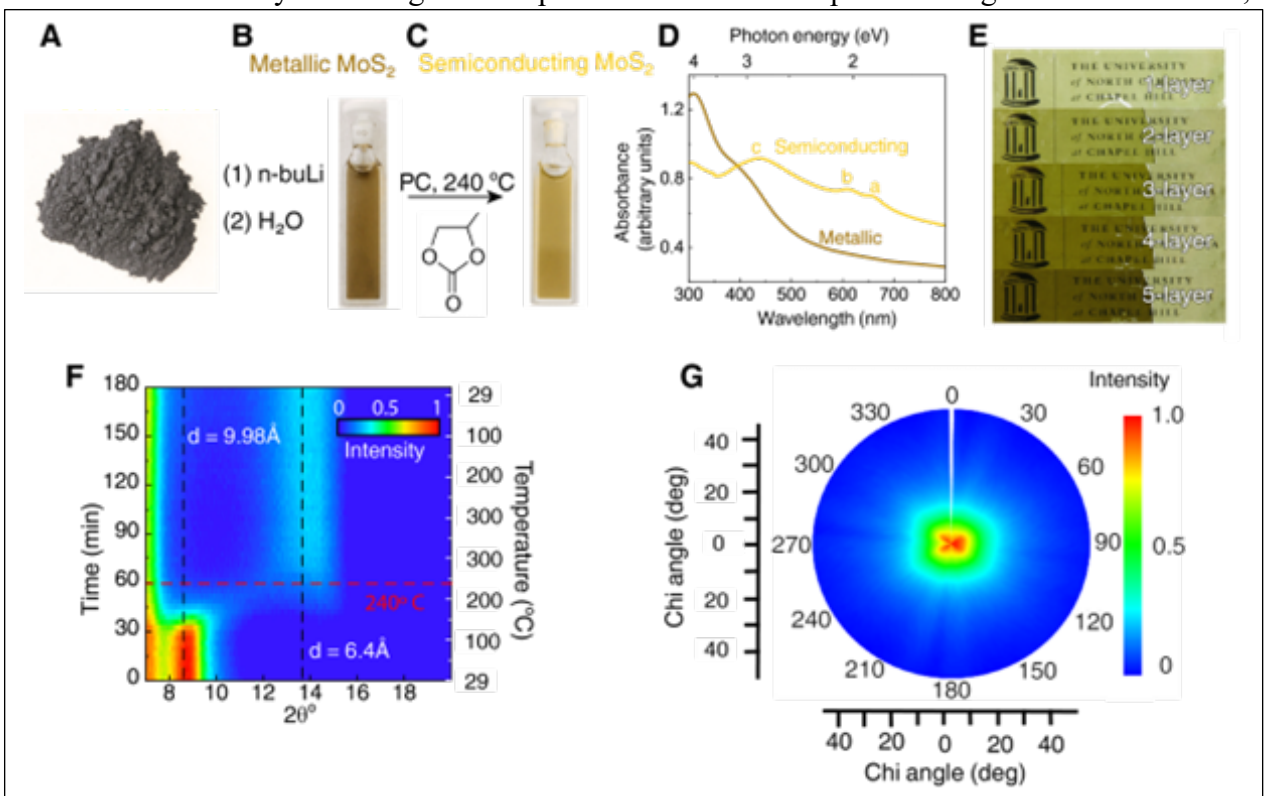


Figure 7. Structural analysis of MoS_2-molecule superlattices. (A) 2H MoS_2 powder was exfoliated with n-butyl lithium yielding (B) a dispersion of metallic MoS_2 monolayers. This was refluxed in propylene carbonate, yielding (C) a dispersion of semiconducting MoS_2 monolayers. (D) UV-vis spectra of these dispersions show the emergence of excitonic transitions after refluxing that are characteristic of semiconducting MoS_2. (E) Films of the monolayer MoS_2 were deposited on a microscope slide using Langmuir-Blodgett (LB) deposition from a water trough. Each "layer" corresponds to a single LB deposition, each of which yields a continuous, 20-40 nm thick superlattice. (F) Evolution of x-ray diffraction intensity for an MoS_2-DMPU superlattice with heating and cooling. (G) Pole figure XRD of the interlayer plane shows that the monolayers are highly ordered relative to the substrate. The logo in figure (E) is trademarked property of the University of North Carolina at Chapel Hill and was reproduced with permission from the Office of Trademarks and Licensing.

semiconducting form (Figure 7C)[37]. In contrast to earlier reports that suggested that surface functionalization of MoS_2 was needed to generate a stable, semiconducting solution[37,38], we identified several solvents in which the MoS_2 remained suspended during refluxing. In most experiments, we used propylene carbonate to convert the brown, metallic MoS_2 to a yellow dispersion by refluxing 2 to 4 hrs. at 240 °C. We found that the MoS_2 could be redispersed in organic solvents with brief sonication. Crucially, these suspensions achieved the requisite stability to assemble into superlattices without the addition of surfactants or ligands. We used all suspensions within five days of synthesis, as irreversible aggregation would occur on longer timescales.

The UV-visible absorbance spectrum of the refluxed MoS_2 solution showed the expected exciton resonances for semiconducting MoS_2 (Figure 7D)[39]. After annealing the 1T (metallic) MoS_2 in PC, the suspension was placed into a quartz cuvette and measurements were collected using a HeCd laser with an excitation wavelength of 442nm. The spectrum collected after annealing shows the emergence of both the A and B exciton peaks, indicating a successful transformation from the 1T metallic to 2H semiconducting phase (Figure 7D). UV-visible spectra of superlattices were collected from LB depositions onto a quartz substrate in the same instrument. These spectra were used to show that increasing the number of LB layers did not change the optical properties of the superlattice despite an apparent change in color (Figure 7E).

The semiconducting solution was also characterized by transmission electron microscopy (TEM) (Figure 8), which showed the flakes had similar thicknesses (primarily monolayer) and lateral dimensions (< 2 μm, with most flakes < 500 nm) as observed for solutions of metallic MoS_2 monolayers[26]. We collected TEM images of the annealed MoS_2 solution to look for morphological changes induced by the annealing process. The sample was prepared by

transferring the exfoliated, 2H MoS_2 into methanol (Sigma-Aldrich 99.9%) and drop casting onto a Lacey Carbon grid. Solvent choice was important in this process, as many "good" solvents (such as PC or DMPU) for the 2H MoS_2 had a vapor pressure too low for drop casting. The grid was dried under ambient conditions for 1 hour imaging. All images were taken at room temperature under high vacuum at an accelerating voltage of 80 kV; voltages of 200 kV caused almost instant sample damage. Images showed that the MoS_2 flakes were thin, but aggregation on the TEM grid made direct imaging of a single monolayer difficult (Figure 9). Flakes were small (<2 μm) and approximately the same size as previously reported[40] chemically exfoliated MoS_2, suggesting that the annealing procedure did not change the lateral dimensions of the monolayers. Additionally, isolated monolayers tended to degrade under the beam, making prolonged imaging difficult. Some flakes with smaller lateral sizes but that were more than one monolayer thick made it through the purification process and these are apparent on the TEM images as darker, sharper edged flakes (seen, for example, in the top right of Figure 8). The occasional presence of these flakes can sometimes be observed in the powder x-ray diffraction patterns as a small peak at 2θ =

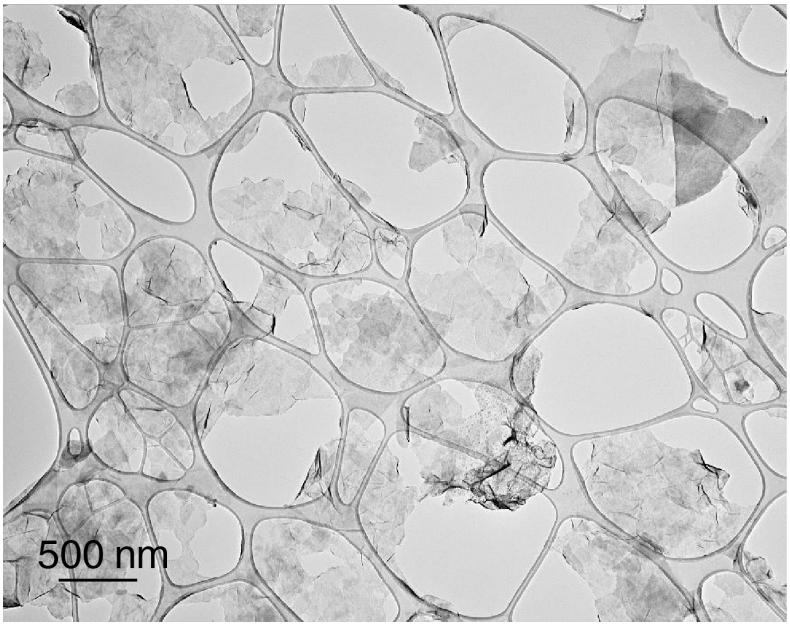


Figure 8: TEM image of exfoliated, 2H MoS_2 after annealing in PC. Flakes visually look thin, and aggregation on the grid most likely occurred due to low solubility in the solvent used for drop casting (MeOH) the sample. In the top right quadrant of the image, a darker, thicker flake is observed. We suggest that this is unexfoliated MoS_2 that was not removed during the purification process.

14.4º. Due to the presence of the (002) diffraction peak at 2θ =14.4º, we suggest that these are unexfoliated MoS_2 flakes rather than reaggregated MoS_2, which tends to appear at slightly lower diffraction angles (2θ =13.8º).

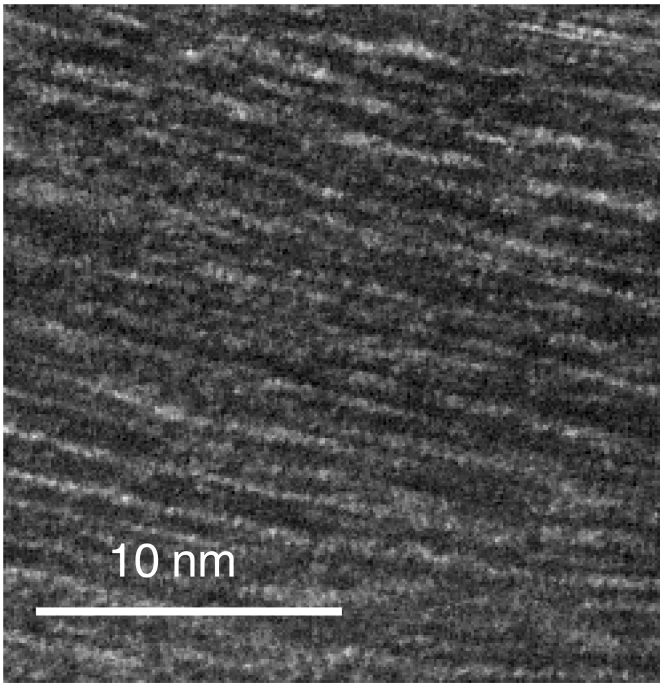


Figure 9: Cross sectional TEM image of a superlattice composed of MoS_2 and 3kg/mol poly(ethyleneglycol). The superlattice degraded quickly under the TEM beam resulting in the lower image quality.

To assemble our solution into a solid film, we adapted a previous method to use air-water interfacial assembly[26,41]. Because of semiconducting MoS_2's poor solubility in water, we transferred our semiconducting MoS_2 into n-butanol (5 mg/mL). To this suspension we added a small quantity of DMPU, as DMPU is both non-volatile and known to be a good solvent (i.e. interacts favorably) with MoS_2[42] (1 mg/mL). We assembled these suspensions at the air-water interface of a Langmuir-Blodgett trough where we could then transfer the resulting film onto a variety of substrates (glass, silicon, polymer). Interestingly, these films maintained the yellow color of the monolayer MoS_2 dispersions even upon assembly into the solid state (Figure 7E). Additionally, upon increasing thickness of the LB layer, no change in exciton position was observed (Figure 10).

To characterize these films, we used powder X-ray diffraction (PXRD, λ = 1.54 Å) to probe the interlayer structure. Films assembled from bulk MoS_2 were grey and had the expected layer-to-layer (002) diffraction at 2θ = 14.4º (d = 6.2 Å). In contrast, a yellow film of MoS_2 assembled

with DMPU showed a peak at 2θ = 8.9° (d = 9.9 Å, Figure 7F). This additional 3.7 Å is consistent with the PMF calculations, where the MoS_2 monolayers alternate with monolayers of DMPU. We observed that the d-spacing changed around ~240 ° C, which is the boiling point of DMPU (Figure 7F). We hypothesize that the removal of DMPU leads to the collapse of the superlattice and a reversion to restacked MoS_2. The high intensity at low angles (< 7°) is from air scattering of the X-ray beam. The decreased d-spacing revealed that heating above the boiling point led to the ejection of DMPU and the formation of a rotationally disordered, turbostratic MoS_2[43]. An important implication of this finding is that the DMPU was not covalently bound to the MoS_2, which is consistent with the trapping of a solvation shell. To better understand the physical structure of the MoS_2-molecule superlattices, we conducted a pole figure XRD analysis to probe the orientational order of the monolayers in the superlattice (Figure 7G). This analysis follows the intensity of the interlayer diffraction peak (2θ =8.9°) as the detector angle changes. The high intensity at chi angles below ~20° suggests that the monolayers are highly coplanar and oriented parallel to the substrate.

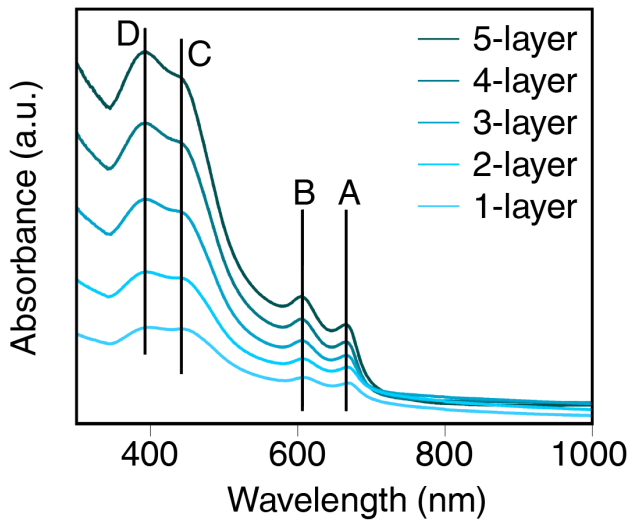


Figure 10: UV-visible spectrum of a MoS_2-DMPU superlattice as increasing numbers of LB layers are added. The A, B, C and D excitons do not change position as the superlattice is made thicker; the absorbance only increases indicating the superlattice is getting thicker.

Additionally, cross sectional TEM images were prepared and analyzed of the superlattices. For many of the images, we observed high coplanarity, consistent with the pole figure XRD, but d-spacings of just ~6Å, consistent with bulk-like MoS_2 (Figure 9). We attribute this smaller-than-

expected d-spacing to the loss of molecules from between the MoS_2 sheets, which could be due to knock-on beam damage, damage from the FIB milling process, evaporation of molecular fragments in the high vacuum of the TEM. During TEM imaging, we sometimes observed the expected superlattice d-spacing of 10 Å change to 6 Å. We attribute this to damage from the electron beam, which is facilitated by the mobility of the molecules and the small thickness of the cross section. In an attempt to minimize beam damage, we used a heavier molecule (PEG 3K). The resulting 6-Å film maintained the coplanar order from the superlattice (Figure 7G) but lost the expanded d-spacing characteristic of the superlattice (Figure 7F).

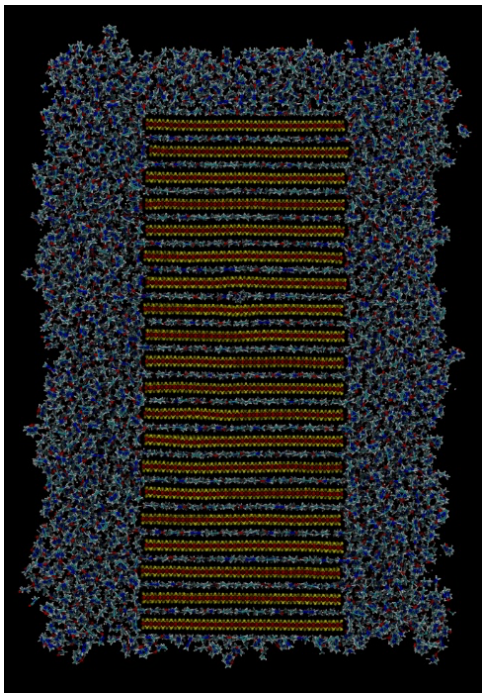


Figure 11: Cross-section of a 20-layer MoS_2-DMPU superlattice surrounded by DMPU solvent. The d-spacing from the middle 10 layers was averaged over time to determine the calculated d-spacing.

To further understand the experimental interlayer spacings (e.g., 10.0 Å in the MoS_2-DMPU superlattice), we performed molecular dynamics simulations of a superlattice with alternating MoS_2 and DMPU monolayers (Figure 11). The MoS_2 sheets were 9 by 9 nm and contained a stack of 20 MoS_2 layers and 19 DMPU layers. The entire stack was then surrounded in all directions by approximately 5 nm of DMPU solvent. The bottom MoS_2 layer was fixed with a spring constraint to prevent the superlattice from tumbling. No other constraints were applied. The simulation was annealed for 10 ns at 300 K, and statistics about the resulting structure were acquired from the final 1 ns of the simulation. These statistics were taken from the middle 10

MoS_2 layers to avoid edge effects. This simulation was repeated for four different initial interlayer spacings of 9.5, 10.0, 10.5, and 11.0 Å.

During annealing, we observed that molecules entered and left the interlayer space, suggesting that the pressure within the interlayer space could readily equilibrate with the 1.0 atm hydrostatic pressure. Even after short periods of annealing, all simulations resulted in the same interlayer d-spacing of 10.0 Å. This exactly matched our experimental observations, strongly suggesting that the model captured the essential physics of the system. Most importantly, the model consists only of nonbonded interactions between the molecules and MoS_2 rather than covalent or ionic interactions.

Additional structural analysis of the DMPU molecules revealed that they laid flat within the interlayer space. We quantified this observation by acquiring statistics about the orientation of DMPU molecules (Figure 12). To do this, we recorded the dipole moment of each DMPU molecule in the interlayer space since the dipole moment closely aligns with the "plane" of the molecule. We defined 0° as a molecule lying flat within the interlayer space. We found that the dipoles of DMPU largely point in an in-plane direction, with most dipoles within 20°. From this finding, we concluded that most DMPU molecules lie flat but that thermal fluctuations tilt molecules out of plane to a small extent.

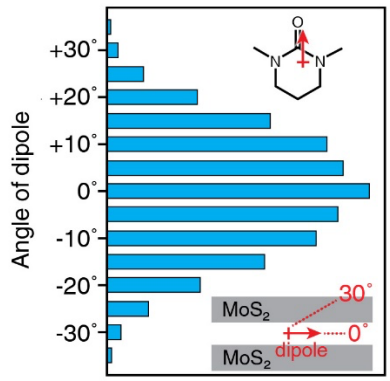


Figure 12: Angular distribution of DMPU dipoles within a MoS_2-DMPU superlattice. Zero degrees indicates that the dipole is in an in-plane direction. 90 degrees is perpendicular to the in-plane direction.

3.3 Generalizability of molecule-semiconductor superlattices

In order to further show the generalizability of the mechanism, we next attempted assembly of a diverse set of chemically and electronically interesting molecules into the MoS_2 interlayer space (Figure 13A). Example diffraction patterns are shown in figure 14 Consistent with previous work, we found that volatile molecules (boiling point < 200 ºC) would not insert into the superlattice. However, we were able to incorporate many different types of non-volatile molecules, including even polymers, into the superlattices. The experimentally measured d-spacings indicate that these molecules lay flat between the layers, and the variations in d-spacing among each superlattice reflects the varying steric constraints of each molecule when confined within the superlattice.

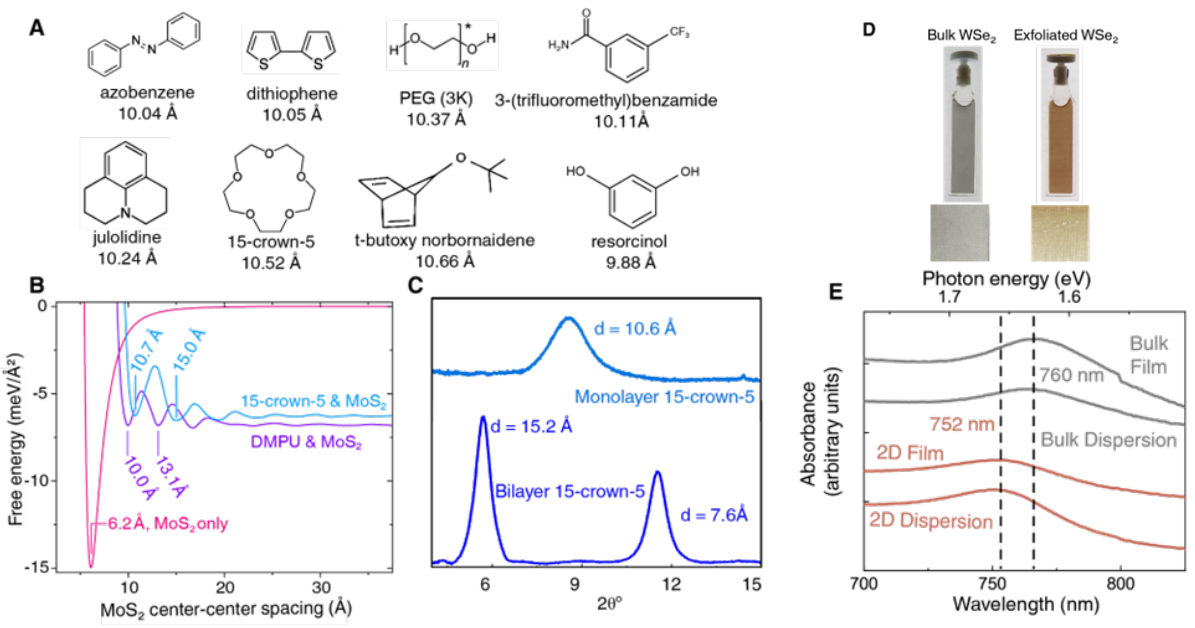


Figure 13: Generalizability of superlattice assembly. (A) Molecules self-assembled with MoS_2 into superlattices, showing experimentally measured d-spacings. (B) Free energy surface of a MoS_2 bilayer at varying intersheet separations in vacuum (pink), DMPU (purple), and 15-crown-5 (blue). (C) Diffraction patterns of superlattices assembled with a small (top) and large (bottom) amount of 15-crown-5. (D) WSe_2 films assembled with no molecules (left) are the same grey color as the bulk solutions, while those assembled in the presence of molecules (right) maintain the brown color indicative of quantum confinement. (E) UV-vis spectra of these dispersions and films show that the 2D dispersions and films absorbance maximum is blue shifted ~8 nm relative to the bulk films and dispersions.

In addition to the chemical generalizability, one of the most intriguing implications of the proposed mechanism is the existence of a potentially stable molecular bilayer superlattice. When we attempted to synthesize this structure with DMPU, however, we found that we could only trap a molecular monolayer. To explore the relative barrier heights between different molecules, we calculated two more potential energy surfaces with DMPU and 15-crown-5, a larger surface area molecule which we hypothesized would increase the barrier to remove a solvation layer. Looking at our PMF curves, we observe qualitatively similar behavior to the previous potential energy landscapes, where multiple local minima exist on both curves (Figure 13B). We also observe that, as predicted, the 15-crown-5 has larger barriers to remove a solvation layer than DMPU. For 15-crown-5, while the final barrier is still the largest, the bilayer to monolayer transition is also quite large, suggesting that the bilayer superlattice is potentially stable enough to synthesize. When we assembled the MoS_2 monolayers with both a small (1 mg/mL) and large (10 mg/mL) amount of 15-crown-5, we observed that the small amount yielded a superlattice with a d-spacing of 10.6 Å, while the large amount yielded a superlattice with a d-spacing of 15.2 Å (Figure 13C), consistent with the calculated monolayer and bilayer structures respectively. Notably, the high ordering of the bilayer is demonstrated by the presence of both (001) (d=15.2 Å) and (002) (d=7.6 Å) reflections.

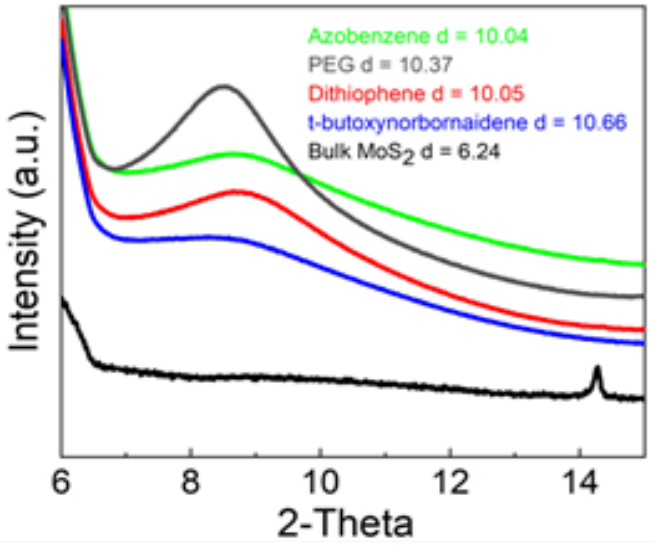


Figure 14: X-ray diffraction patterns for 1 LB layer superlattices composed of unexfoliated MoS_2 (top), and superlattices with either 15-crown-5 (middle) or DMPU (bottom). The increase in intensity at low angles is from air scattering of the X-ray beam.

Superlattices assembled in the presence of different molecules had different d-spacings, as observed by XRD (Figure 14). To obtain additional evidence for the incorporation of different molecules, we utilized XPS.

We assembled MoS_2 superlattices that contained 3-trifluoromethylbenzamide (Sigma-Aldrich, 99.8%). By XPS, we observed that fluorine makes up approximately 1% of the sample by atomic percent (Table 1, Figure 15). While a volumetric analysis of the superlattice suggests that the superlattice should contain ~10% fluorine by mass, the evaporation of 3-trifluoromethylbenzamide in high vacuum near the sample's surface makes quantitative interpretation difficult. Indeed, the molecule has a boiling point of 241°C, which would lead to the rapid depletion of the molecule from the superlattice's surface in high vacuum. This evaporation is consistent with the

Table 1: Quantification table of the XPS spectrum (Figure 15). The first column (BE = binding energy) indicates peak position, the second column (RSF = relative sensitivity factor) indicates the relative sensitivity of the technique to each peak, and the third and fourth columns indicate the atomic and mass concentration of each atom type respectively.

	BE [eV]	RSF	Atomic conc. [%]	Error [%]	Mass conc. [%]	Error [%]
S 2p	162.57	0.67	26.8	0.18	29.8	0.13
O 1s	532.27	0.78	10.9	0.19	6.0	0.11
N 1s	392.97	0.48	0.0		0.0	
Mo 3d	228.87	3.32	13.1	0.11	43.5	0.20
F 1s	688.87	1.00	1.2	0.07	0.8	0.05
C 1s	284.57	0.28	48.0	0.34	20.0	0.21

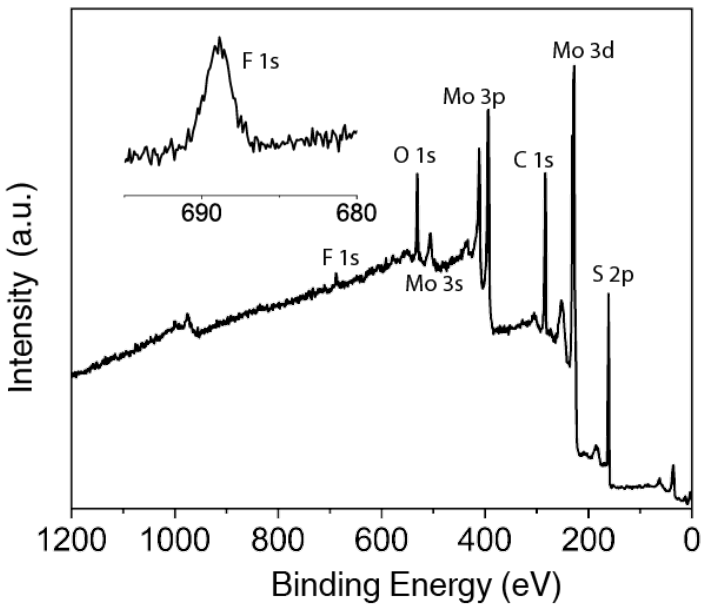


Figure 15: XPS spectrum of a MoS_2-3-(trifluoromethyl)benzamide superlattice. The XPS spectrum shows expected elements on the surface of the superlattice, and additionally it shows the F 1s peak indicative of 3-(trifluoromethyl)benzamide.

temperature-dependent PXRD (Figure 7F), which showed that the vapor pressure of a molecule is not significantly modified by its incorporation in a superlattice.

Milling the sample in the XPS led to a further drop of the signal from fluorine. This observation is consistent with our earlier observation that molecules are readily lost from the superlattice when prepared as a thin cross-section for TEM. In both cases of milling, the creation of new surfaces provides a route by which molecules can be lost.

We further generalized the self-assembly procedure to WSe_2 (Figure 13D). To generate solutions of exfoliated WSe_2, we used a standard liquid exfoliation in NMP[44] rather than the chemical exfoliation approach we used for MoS_2. These samples had a wider distribution of thicknesses (i.e. not all monolayers) than the MoS_2 and therefore the observation of superlattice reflections by diffraction was not possible. However, a visual comparison of films made from either 2D or bulk materials shows that the films made from 2D materials retain absorption characteristics that are indicative of quantum-confinement (Figure 13E), suggesting that films assembled from bulk materials were different than films assembled from exfoliated materials.

3.4 Quantum-confined but electrically conductive superlattices

Because our synthetic approach left the MoS_2 unfunctionalized, we began to explore whether its unique monolayer properties, such as a direct band gap and increased photoluminescence (PL)[39,40,45], were preserved within the superlattices. Previously, it was found that these properties were not preserved when MoS_2 monolayers were restacked without any molecular layer[15,46]. It was also observed that the photoluminescence of MoS_2 could be quenched when it was placed next to an organic layer with a small band gap because of fast charge transfer[47]. In our study, to minimize charge transfer between the MoS_2 and molecular layer, we used DMPU

due to its large HOMO-LUMO gap. By preventing PL quenching, we could then compare the PL of the superlattice to that of pristine MoS_2 monolayers.

To explore quantum confinement within the superlattice, we used variable-pressure PL measurements. Unlike the direct interpretation of PL energy, which depends on dielectric

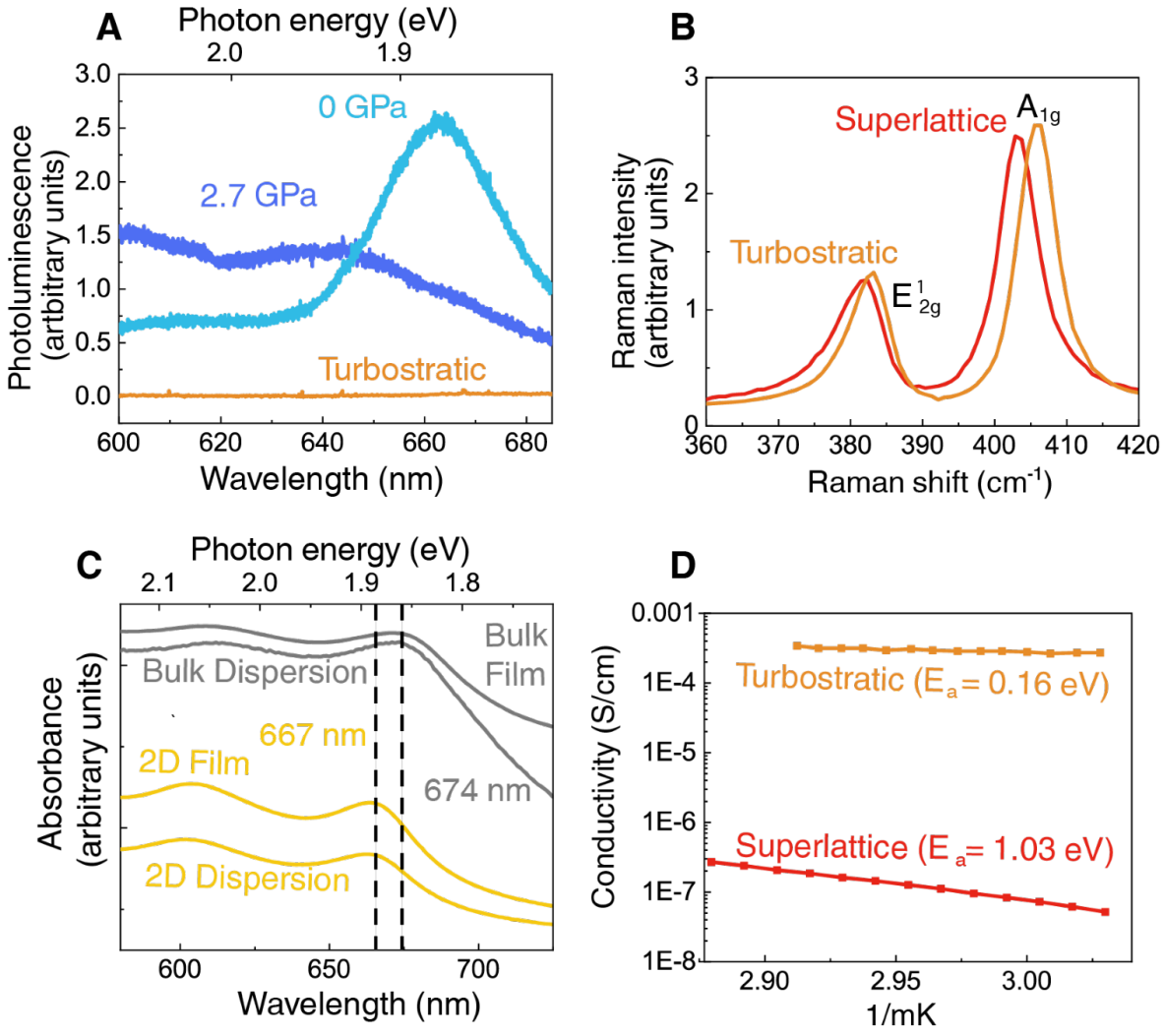


Figure 16. Quantum-confined properties of MoS_2-molecule superlattices. (A) The PL of the DMPU-MoS_2 superlattice blue shifts upon compression and the PL is absent after removing the molecular layer. The 0 and 2.7 GPa experiments were performed in a diamond anvil cell, while the turbostratic experiment was performed on a silicon wafer at 0 GPa (see SI for details). (B) Raman spectra of the superlattice and resulting turbostratic MoS_2. (C) UV-visible spectra show that the excitonic positions of the 2D films and dispersion match and are blue-shifted from the bulk films and dispersions. (D) Conductivity increases upon removal of the molecular layer and the activation energy changes from 1.03 eV to 0.16 eV upon annealing.

environment[48], varying pressure provides an easy-to-interpret measure of quantum confinement. Specifically, it was previously observed that, under increased pressure, the PL of monolayers blueshifts by 19 meV per GPa, while bilayer and thicker MoS_2 redshifts at pressures above 2.4 GPa[49]. Our measurements, performed at 2.7 GPa on a MoS_2-DMPU superlattice, showed a blueshift of 18 meV per GPa (Figure 16A). This indicated that the electronic structure of the MoS_2 within the superlattice was similar to that of pristine, quantum-confined monolayers. Importantly, when the molecular layer is removed by heating above the boiling point of the DMPU, no PL was observed (Figure 16A). This is consistent with the absence of photoluminescence from rotationally disordered (turbostratic) MoS_2 films[15,46,50]. These observations indicate that the molecular layer, which physically separates the MoS_2 monolayers, is essential for maintaining quantum confinement.

To further explore how the molecular layer influenced superlattice properties, we performed Raman spectroscopy (Figure 16B), which is sensitive to the environment of the MoS_2. As a control experiment, we heated the superlattice to remove the DMPU layers, yielding turbostratic MoS_2. Following this treatment, both peaks exhibited bulk-like frequencies[51] (Figure 16B, orange). In contrast, for a superlattice that contained DMPU, we observe that the out-of-plane A_{1g} vibration (402.7 cm^{-1}) exactly matches the expected value for monolayer MoS_2, while the in-plane E^1_{2g} vibration (381.8 cm^{-1}) nearly matches the value for bulk MoS_2[51] (Figure 16B, red). Our observation of both bulk- and monolayer-like vibrations within a single material highlights a gap in understanding that may be interesting for further study. Most importantly, however, these findings illustrate the unique environment provided by the molecular monolayer.

Because PL and Raman probe small regions, we acquired UV-vis transmission spectra over large areas (5 mm diameter). We observed that the excitonic peaks of the superlattice and 2D

dispersion had identical wavelengths, indicative of similar quantum confinement (Figure 16C). We therefore conclude that the Raman and PL findings are applicable to the entire film.

Because the conductive MoS_2 layers were separated by molecules with a wide HOMO-LUMO gap, it could be expected that the electrical conductivity of the superlattice was poor. To assess this prediction, we measured electrical conductivity vs. temperature with and without a DMPU monolayer (Figure 16D). The room-temperature conductivity in the MoS_2-DMPU superlattice was surprisingly high, 4×10^{-8} S/cm, similar to previous solution-processed MoS_2 films[52]. Removal of the molecules increased the conductivity more than 10,000-fold to 2×10^{-4} S/cm. We attribute this 4-order-of-magnitude increase to the 4 Å decrease in interlayer spacing (Figure 7C). This is consistent with previous observations that tunneling currents through simple organic molecules increase ~10-fold per Å[53]. The close match between the observed and expected changes indicates that the electrical conductivity of the superlattice is limited by tunneling, which further validates our structural model in which the entire film is comprised of alternating monolayers of MoS_2 and molecules (Figure 1A).

Interestingly, one of the highest reported electrical conductivities for solution-processed MoS_2 is 10^{-6} S/cm[52], two orders of magnitude lower than our molecule-free films. We attribute the higher conductivity of our films to the greater degree of co-planarity and lack of porosity. When flakes are not co-planar, tunneling is limited to the few points of contact between adjacent flakes. In contrast, co-planar MoS_2 has large planes of contact, which facilitates flake-to-flake tunneling at any location on the flake's surface.

The conductivity measurements also provide an opportunity to strengthen our understanding of the superlattice's electronic structure. In a semiconductor, the creation of charge

carriers requires excitation across the bandgap. Because a single excitation creates two carriers (one hole, one electron), the semiconductor's bandgap, E_g, is calculated as[54]:

$$E_g = 2\ E_a$$

where E_a is the slope obtained from Figure 16D. The E_a of 1.03 eV therefore yields a bandgap of the superlattice as 2.06 eV, matching previously reported values for monolayer MoS_2[55,56]. In contrast, the E_a for the molecule-free films was just 0.16 eV, which is common for bulk MoS_2[57], and indicates that carriers are activated from trap states.

Conclusions and Outlook

In this work, we introduce a mechanism that describes the self-assembly of 2D materials and molecules to form 3D superlattices. In addition to explaining previous observations for the assembly of 2D metals and molecules, the mechanism extends the design space to include 2D semiconductors and insulators because we show that the self-assembly does not depend on specific chemical functionality of either the 2D material or the molecules. A fascinating aspect of the mechanism is that it predicts many kinetically stable structures during the self-assembly process. Our ability to experimentally realize one such structure, a superlattice containing bilayers of 15-crown-5, supports the mechanism's validity and hints at the ways that the design space for superlattices is now expanded. A surprising outcome of the mechanism is that it explains the high kinetic stability of the superlattices despite their low thermodynamic stability. This high kinetic stability makes these materials easy to synthesize and affords long-term stability for possible applications. The mechanism also suggests that other stacking sequences are possible within superlattices, such as those based on trilayers of organic molecules or mixtures of two different molecules. This expanded design space is a straightforward consequence of the weak van der

Waals forces that drive the self-assembly process, allowing wide generalizability to many 2D materials, molecules, and polymers.

The fact that the superlattices are held together by simple van der Waals interactions also helps explain some of their exciting properties. Most importantly, the superlattices we report here achieve good electrical conductivity while also retaining the quantum-confined properties that are intrinsic to the MoS_2 monolayers from which they are built. This confined-yet-conductive combination has been a long-sought characteristic[58,59], because this allows the design of bulk materials with tailored optoelectronic properties that are derived directly from their component parts. For example, quantum dot solids are now utilized as the active component in consumer displays[60,61]. The ability to extend this concept to 2D materials offers a large design space with tailored building blocks, thus offering many opportunities for fundamental science and technological applications.

Adapted with permission from Peterson, D. A.; Farnsworth, T. W.; Woomer, A. H.; Fishman, Z. S.; Shapiro, S. H.; Radomsky, R. C.; Barron, E. A.; Thompson, J. R.; Warren, S. C. Generalized Assembly of Semiconductor–Molecule Superlattices. Chem. Mater. 2025, 37 (1), 119–128. DOI: 10.1021/acs.chemmater.4c02165. Copyright 2025 American Chemical Society.

REFERENCES

(1) Gamble, F. R.; Osiecki, J. H.; Cais, M.; Pisharody, R.; Disalvo, F. J.; Geballe, T. H. Intercalation Complexes of Lewis Bases and Layered Sulfides: A Large Class of New Superconductors. *Science* **1971**, *174* (4008), 493–497. DOI: 10.1126/science.174.4008.493.

(2) Moncton, D. E.; Axe, J. D.; DiSalvo, F. J. Study of Superlattice Formation In-Nband-Taby Neutron Scattering. *Phys. Rev. Lett.* **1975**, *34* (12), 734–737. DOI: 10.1103/PhysRevLett.34.734.

(3) Di Salvo, F. J.; Hull, G. W.; Schwartz, L. H.; Voorhoeve, J. M.; Waszczak, J. V. Metal Intercalation Compounds of TaS2: Preparation and Properties. *J. Chem. Phys.* **1973**, *59* (4), 1922–1929. DOI: 10.1063/1.1680277.

(4) Whittingham, M. S.; Gamble, F. R. The Lithium Intercalates of the Transition Metal Dichalcogenides. *Mater. Res. Bull.* **1975**, *10* (5), 363–371. DOI: 10.1016/0025-5408(75)90006-9.

(5) Whittingham, M. S. Electrical Energy Storage and Intercalation Chemistry. *Science* **1976**, *192* (4244), 1126–1127. DOI: 10.1126/science.192.4244.1126.

(6) Mizushima, K.; Jones, P. C.; Wiseman, P. J.; Goodenough, J. B. LixCoO2 (0< X< -1): A New Cathode Material for Batteries of High Energy Density. *Mater. Res. Bull.* **1980**, *15* (6), 783–789. DOI: 10.1016/0025-5408(80)90012-4.

(7) Jariwala, D.; Marks, T. J.; Hersam, M. C. Mixed-Dimensional van Der Waals Heterostructures. *Nat. Mater.* **2017**, *16* (2), 170–181. DOI: 10.1038/nmat4703.

(8) Ferrari, A. C.; Bonaccorso, F.; Fal'ko, V.; Novoselov, K. S.; Roche, S.; Bøggild, P.; Borini, S.; Koppens, F. H. L.; Palermo, V.; Pugno, N.; Garrido, J. A.; Sordan, R.; Bianco, A.; Ballerini, L.; Prato, M.; Lidorikis, E.; Kivioja, J.; Marinelli, C.; Ryhänen, T.; Morpurgo, A.; Coleman, J. N.; Nicolosi, V.; Colombo, L.; Fert, A.; Garcia-Hernandez, M.; Bachtold, A.; Schneider, G. F.; Guinea, F.; Dekker, C.; Barbone, M.; Sun, Z.; Galiotis, C.; Grigorenko, A. N.; Konstantatos, G.; Kis, A.; Katsnelson, M.; Vandersypen, L.; Loiseau, A.; Morandi, V.; Neumaier, D.; Treossi, E.; Pellegrini, V.; Polini, M.; Tredicucci, A.; Williams, G. M.; Hong, B. H.; Ahn, J.-H.; Kim, J. M.; Zirath, H.; van Wees, B. J.; van der Zant, H.; Occhipinti, L.; Di Matteo, A.; Kinloch, I. A.; Seyller, T.; Quesnel, E.; Feng, X.; Teo, K.; Rupesinghe, N.; Hakonen, P.; Neil, S. R. T.; Tannock, Q.; Löfwander, T.; Kinaret, J. Science and Technology Roadmap for Graphene, Related Two-Dimensional Crystals, and Hybrid Systems. *Nanoscale* **2015**, *7* (11), 4598–4810. DOI: 10.1039/c4nr01600a.

(9) Hart, J. L.; Hantanasirisakul, K.; Lang, A. C.; Anasori, B.; Pinto, D.; Pivak, Y.; van Omme, J. T.; May, S. J.; Gogotsi, Y.; Taheri, M. L. Control of MXenes' Electronic

Properties through Termination and Intercalation. *Nat. Commun.* **2019**, *10* (1), 522. DOI: 10.1038/s41467-018-08169-8.

(10) Kappera, R.; Voiry, D.; Yalcin, S. E.; Branch, B.; Gupta, G.; Mohite, A. D.; Chhowalla, M. Phase-Engineered Low-Resistance Contacts for Ultrathin MoS2 Transistors. *Nat. Mater.* **2014**, *13* (12), 1128–1134. DOI: 10.1038/nmat4080.

(11) Qian, Q.; Ren, H.; Zhou, J.; Wan, Z.; Zhou, J.; Yan, X.; Cai, J.; Wang, P.; Li, B.; Sofer, Z.; Li, B.; Duan, X.; Pan, X.; Huang, Y.; Duan, X. Chiral Molecular Intercalation Superlattices. *Nature* **2022**, *606* (7916), 902–908. DOI: 10.1038/s41586-022-04846-3.

(12) Dai, H.; Tang, M.; Huang, J.; Wang, Z. A Series of Molecule-Intercalated MoS2 as Anode Materials for Sodium Ion Batteries. *ACS Appl. Mater. Interfaces* **2021**, *13* (9), 10870–10877. DOI: 10.1021/acsami.0c21106.

(13) Han, X.; Yang, J.; Zhang, Y.-W.; Yu, Z. G. Molecular Engineering on a MoS2 Interlayer for High-Capacity and Rapid-Charging Aqueous Ion Batteries. *Nanoscale Adv.* **2023**, *5* (9), 2639–2645. DOI: 10.1039/d3na00068k.

(14) Zhong, Y.; Cheng, B.; Park, C.; Ray, A.; Brown, S.; Mujid, F.; Lee, J.-U.; Zhou, H.; Suh, J.; Lee, K.-H.; Mannix, A. J.; Kang, K.; Sibener, S. J.; Muller, D. A.; Park, J. Wafer-Scale Synthesis of Monolayer Two-Dimensional Porphyrin Polymers for Hybrid Superlattices. *Science* **2019**, *366* (6471), 1379–1384. DOI: 10.1126/science.aax9385.

(15) Mannix, A. J.; Ye, A.; Sung, S. H.; Ray, A.; Mujid, F.; Park, C.; Lee, M.; Kang, J.-H.; Shreiner, R.; High, A. A.; Muller, D. A.; Hovden, R.; Park, J. Robotic Four-Dimensional Pixel Assembly of van Der Waals Solids. *Nat. Nanotechnol.* **2022**, *17* (4), 361–366. DOI: 10.1038/s41565-021-01061-5.

(16) Stark, M. S.; Kuntz, K. L.; Martens, S. J.; Warren, S. C. Intercalation of Layered Materials from Bulk to 2D. *Adv. Mater.* **2019**, *31* (27), e1808213. DOI: 10.1002/adma.201808213.

(17) Lomax, J. F.; Diel, B. N.; Marks, T. J. New Information On 2H-TaS_2 Intercalation Chemistry With Organic Bases. *Molecular Crystals and Liquid Crystals* **1985**, *121* (1–4), 145–148. DOI: 10.1080/00268948508074850.

(18) Joy, P. A.; Vasudevan, S. The Intercalation Reaction of Pyridine with Manganese Thiophosphate, MnPS3. *J. Am. Chem. Soc.* **1992**, *114* (20), 7792–7801. DOI: 10.1021/ja00046a027.

(19) Johnson, J. W. Amine Intercalation in Tantalum Disulfide: The Effect of Small Amounts of Water. *Physica B+C* **1980**, *99* (1–4), 141–144. DOI: 10.1016/0378-4363(80)90223-5.

(20) Friend, R. H.; Yoffe, A. D. Electronic Properties of Intercalation Complexes of the Transition Metal Dichalcogenides. *Adv. Phys.* **1987**, *36* (1), 1–94. DOI: 10.1080/00018738700101951.

(21) Pereira, J. M.; Tezze, D.; Niehues, I.; Asensio, Y.; Yang, H.; Mester, L.; Chen, S.; Casanova, F.; Bittner, A. M.; Ormaza, M.; Schiller, F.; Martín-García, B.; Hillenbrand, R.; Hueso, L. E.; Gobbi, M. Percolating Superconductivity in Air-stable Organic-ion Intercalated Mos_2. *Adv. Funct. Mater.* **2022**, *32* (52). DOI: 10.1002/adfm.202208761.

(22) Pereira, J. M.; Tezze, D.; Martín-García, B.; Casanova, F.; Ormaza, M.; Hueso, L. E.; Gobbi, M. Enhanced Superconductivity in 2H-TaS2 Devices through in Situ Molecular Intercalation. *ACS Appl. Mater. Interfaces* **2024**, *16* (31), 41626–41632. DOI: 10.1021/acsami.4c04997.

(23) Woollam, J. A.; Somoano, R. B. Physics and Chemistry of MoS2 Intercalation Compounds. *Materials Science and Engineering* **1977**, *31*, 289–295. DOI: 10.1016/0025-5416(77)90048-9.

(24) Py, M. A.; Haering, R. R. Structural Destabilization Induced by Lithium Intercalation in MoS_2 and Related Compounds. *Can. J. Phys.* **1983**, *61* (1), 76–84. DOI: 10.1139/p83-013.

(25) Liu, B.; Xu, W.; Long, X.; Cao, J. Atomic Mechanism of Lithium Intercalation Induced Phase Transition in Layered MoS2. *Phys. Chem. Chem. Phys.* **2022**, *24* (31), 18777–18782. DOI: 10.1039/d2cp02210a.

(26) Divigalpitiya, W. M.; Frindt, R. F.; Morrison, S. R. Inclusion Systems of Organic Molecules in Restacked Single-Layer Molybdenum Disulfide. *Science* **1989**, *246* (4928), 369–371. DOI: 10.1126/science.246.4928.369.

(27) Joensen, P.; Frindt, R. F.; Morrison, S. R. Single-Layer MoS2. *Mater. Res. Bull.* **1986**, *21* (4), 457–461. DOI: 10.1016/0025-5408(86)90011-5.

(28) Tsai, H.-L.; Heising, J.; Schindler, J. L.; Kannewurf, C. R.; Kanatzidis, M. G. Exfoliated−restacked Phase of Ws_2. *Chem. Mater.* **1997**, *9* (4), 879–882. DOI: 10.1021/cm960579t.

(29) Kuo, D.-Y.; Cossairt, B. M. Direct Intercalation of MoS2 and WS2 Thin Films by Vacuum Filtration. *Mater. Horiz.* **2022**, *9* (1), 360–367. DOI: 10.1039/d1mh01193f.

(30) Sresht, V.; Govind Rajan, A.; Bordes, E.; Strano, M. S.; Pádua, A. A. H.; Blankschtein, D. Quantitative Modeling of MoS_2 –Solvent Interfaces: Predicting Contact Angles and Exfoliation Performance Using Molecular Dynamics. *J. Phys. Chem. C* **2017**, *121* (16), 9022–9031. DOI: 10.1021/acs.jpcc.7b00484.

(31) Frenkel, D. Order through Entropy. *Nat. Mater.* **2015**, *14* (1), 9–12. DOI: 10.1038/nmat4178.

(32) Aboutalebi, S. H.; Gudarzi, M. M.; Zheng, Q. B.; Kim, J.-K. Spontaneous Formation of Liquid Crystals in Ultralarge Graphene Oxide Dispersions. *Adv. Funct. Mater* **2011**, *21* (15), 2978–2988. DOI: 10.1002/adfm.201100448.

(33) Jalili, R.; Aminorroaya-Yamini, S.; Benedetti, T. M.; Aboutalebi, S. H.; Chao, Y.; Wallace, G. G.; Officer, D. L. Processable 2D Materials beyond Graphene: MoS2 Liquid Crystals and Fibres. *Nanoscale* **2016**, *8* (38), 16862–16867. DOI: 10.1039/c6nr03681c.

(34) Puech, N.; Blanc, C.; Grelet, E.; Zamora-Ledezma, C.; Maugey, M.; Zakri, C.; Anglaret, E.; Poulin, P. Highly Ordered Carbon Nanotube Nematic Liquid Crystals. *J. Phys. Chem. C* **2011**, *115* (8), 3272–3278. DOI: 10.1021/jp1102077.

(35) Khanna, V.; Monroe, J. I.; Doherty, M. F.; Peters, B. Performing Solvation Free Energy Calculations in LAMMPS Using the Decoupling Approach. *J. Comput. Aided Mol. Des.* **2020**, *34* (6), 641–646. DOI: 10.1007/s10822-020-00303-3.

(36) El-Meligi, A. A. Investigation of MnPS3 Intercalates with Pyridinium Ion. *Mater. Chem. Phys* **2004**, *84* (2–3), 331–340. DOI: 10.1016/j.matchemphys.2003.11.019.

(37) Sim, D. M.; Han, H. J.; Yim, S.; Choi, M.-J.; Jeon, J.; Jung, Y. S. Long-Term Stable 2H-MoS2 Dispersion: Critical Role of Solvent for Simultaneous Phase Restoration and Surface Functionalization of Liquid-Exfoliated MoS2. *ACS Omega* **2017**, *2* (8), 4678–4687. DOI: 10.1021/acsomega.7b00841.

(38) Chou, S. S.; Huang, Y.-K.; Kim, J.; Kaehr, B.; Foley, B. M.; Lu, P.; Dykstra, C.; Hopkins, P. E.; Brinker, C. J.; Huang, J.; Dravid, V. P. Controlling the Metal to Semiconductor Transition of MoS2 and WS2 in Solution. *J. Am. Chem. Soc.* **2015**, *137* (5), 1742–1745. DOI: 10.1021/ja5107145.

(39) Splendiani, A.; Sun, L.; Zhang, Y.; Li, T.; Kim, J.; Chim, C.-Y.; Galli, G.; Wang, F. Emerging Photoluminescence in Monolayer MoS2. *Nano Lett.* **2010**, *10* (4), 1271–1275. DOI: 10.1021/nl903868w.

(40) Eda, G.; Yamaguchi, H.; Voiry, D.; Fujita, T.; Chen, M.; Chhowalla, M. Photoluminescence from Chemically Exfoliated MoS2. *Nano Lett.* **2011**, *11* (12), 5111–5116. DOI: 10.1021/nl201874w.

(41) Joensen, P.; Crozier, E. D.; Alberding, N.; Frindt, R. F. A Study of Single-Layer and Restacked MoS_2 by X-Ray Diffraction and X-Ray Absorption Spectroscopy. *J. Phys. C: Solid State Phys.* **1987**, *20* (26), 4043–4053. DOI: 10.1088/0022-3719/20/26/009.

(42) Coleman, J. N.; Lotya, M.; O'Neill, A.; Bergin, S. D.; King, P. J.; Khan, U.; Young, K.; Gaucher, A.; De, S.; Smith, R. J.; Shvets, I. V.; Arora, S. K.; Stanton, G.; Kim, H.-Y.;

Lee, K.; Kim, G. T.; Duesberg, G. S.; Hallam, T.; Boland, J. J.; Wang, J. J.; Donegan, J. F.; Grunlan, J. C.; Moriarty, G.; Shmeliov, A.; Nicholls, R. J.; Perkins, J. M.; Grieveson, E. M.; Theuwissen, K.; McComb, D. W.; Nellist, P. D.; Nicolosi, V. Two-Dimensional Nanosheets Produced by Liquid Exfoliation of Layered Materials. *Science* **2011**, *331* (6017), 568–571. DOI: 10.1126/science.1194975.

(43) Moser, J.; Lévy, F. Random Stacking in MoS2−x Sputtered Thin Films. *Thin Solid Films* **1994**, *240* (1–2), 56–59. DOI: 10.1016/0040-6090(94)90693-9.

(44) Nicolosi, V.; Chhowalla, M.; Kanatzidis, M. G.; Strano, M. S.; Coleman, J. N. Liquid Exfoliation of Layered Materials. *Science* **2013**, *340* (6139), 1226419–1226419. DOI: 10.1126/science.1226419.

(45) Mak, K. F.; Lee, C.; Hone, J.; Shan, J.; Heinz, T. F. Atomically Thin MoS_2: A New Direct-Gap Semiconductor. *Phys. Rev. Lett.* **2010**, *105* (13), 136805. DOI: 10.1103/PhysRevLett.105.136805.

(46) Liu, K.; Zhang, L.; Cao, T.; Jin, C.; Qiu, D.; Zhou, Q.; Zettl, A.; Yang, P.; Louie, S. G.; Wang, F. Evolution of Interlayer Coupling in Twisted Molybdenum Disulfide Bilayers. *Nat. Commun.* **2014**, *5*, 4966. DOI: 10.1038/ncomms5966.

(47) Balch, H. B.; Evans, A. M.; Dasari, R. R.; Li, H.; Li, R.; Thomas, S.; Wang, D.; Bisbey, R. P.; Slicker, K.; Castano, I.; Xun, S.; Jiang, L.; Zhu, C.; Gianneschi, N.; Ralph, D. C.; Brédas, J.-L.; Marder, S. R.; Dichtel, W. R.; Wang, F. Electronically Coupled 2D Polymer/Mos2 Heterostructures. *J. Am. Chem. Soc.* **2020**, *142* (50), 21131–21139. DOI: 10.1021/jacs.0c10151.

(48) Lin, Y.; Ling, X.; Yu, L.; Huang, S.; Hsu, A. L.; Lee, Y.-H.; Kong, J.; Dresselhaus, M. S.; Palacios, T. Dielectric Screening of Excitons and Trions in Single-Layer MoS2. *Nano Lett.* **2014**, *14* (10), 5569–5576. DOI: 10.1021/nl501988y.

(49) Dou, X.; Ding, K.; Jiang, D.; Sun, B. Tuning and Identification of Interband Transitions in Monolayer and Bilayer Molybdenum Disulfide Using Hydrostatic Pressure. *ACS Nano* **2014**, *8* (7), 7458–7464. DOI: 10.1021/nn502717d.

(50) Huang, S.; Ling, X.; Liang, L.; Kong, J.; Terrones, H.; Meunier, V.; Dresselhaus, M. S. Probing the Interlayer Coupling of Twisted Bilayer MoS2 Using Photoluminescence Spectroscopy. *Nano Lett.* **2014**, *14* (10), 5500–5508. DOI: 10.1021/nl5014597.

(51) Li, H.; Zhang, Q.; Yap, C. C. R.; Tay, B. K.; Edwin, T. H. T.; Olivier, A.; Baillargeat, D. From Bulk to Monolayer Mos2: Evolution of Raman Scattering. *Adv. Funct. Mater* **2012**, *22* (7), 1385–1390. DOI: 10.1002/adfm.201102111.

(52) Kelly, A. G.; Hallam, T.; Backes, C.; Harvey, A.; Esmaeily, A. S.; Godwin, I.; Coelho, J.; Nicolosi, V.; Lauth, J.; Kulkarni, A.; Kinge, S.; Siebbeles, L. D. A.; Duesberg, G. S.;

Coleman, J. N. All-Printed Thin-Film Transistors from Networks of Liquid-Exfoliated Nanosheets. *Science* **2017**, *356* (6333), 69–73. DOI: 10.1126/science.aal4062.

(53) Zabet-Khosousi, A.; Dhirani, A.-A. Charge Transport in Nanoparticle Assemblies. *Chem. Rev.* **2008**, *108* (10), 4072–4124. DOI: 10.1021/cr0680134.

(54) Sze, S. M.; Ng, K. K. *Physics of Semiconductor Devices*; John Wiley & Sons, Inc.: Hoboken, NJ, USA, 2006. DOI: 10.1002/0470068329.

(55) Komsa, H.-P.; Krasheninnikov, A. V. Effects of Confinement and Environment on the Electronic Structure and Exciton Binding Energy of MoSfrom First Principles. *Phys. Rev. B* **2012**, *86* (24), 241201. DOI: 10.1103/PhysRevB.86.241201.

(56) Ryou, J.; Kim, Y.-S.; Kc, S.; Cho, K. Monolayer Mos2 Bandgap Modulation by Dielectric Environments and Tunable Bandgap Transistors. *Sci. Rep.* **2016**, *6*, 29184. DOI: 10.1038/srep29184.

(57) El-Mahalawy, S. H.; Evans, B. L. Temperature Dependence of the Electrical Conductivity and Hall Coefficient in 2H-MoS2, MoSe2, WSe2, and MoTe2. *Phys. Status Solidi B* **1977**, *79* (2), 713–722. DOI: 10.1002/pssb.2220790238.

(58) Baumgardner, W. J.; Whitham, K.; Hanrath, T. Confined-but-Connected Quantum Solids via Controlled Ligand Displacement. *Nano Lett.* **2013**, *13* (7), 3225–3231. DOI: 10.1021/nl401298s.

(59) Whitham, K.; Yang, J.; Savitzky, B. H.; Kourkoutis, L. F.; Wise, F.; Hanrath, T. Charge Transport and Localization in Atomically Coherent Quantum Dot Solids. *Nat. Mater.* **2016**, *15* (5), 557–563. DOI: 10.1038/nmat4576.

(60) Kim, J.; Roh, J.; Park, M.; Lee, C. Recent Advances and Challenges of Colloidal Quantum Dot Light-emitting Diodes for Display Applications. *Adv. Mater.* **2023**. DOI: 10.1002/adma.202212220.

(61) Shu, Y.; Lin, X.; Qin, H.; Hu, Z.; Jin, Y.; Peng, X. Quantum Dots for Display Applications. *Angew. Chem.* **2020**, *132* (50), 22496–22507. DOI: 10.1002/ange.202004857.

CHAPTER FOUR – CHARACTERISTICS AND PROPERTIES OF 2 DIMENSIONALLY CONFINED LIQUIDS

Introduction

Liquids are one of the three classical states of matter and are characterized as being highly disordered relative to their comparable solid state. In a solid crystal, atoms are highly organized into a lattice with long range repetitions of the same patterns of atoms. In a liquid, the same atoms arrange more randomly and do not have the long range order characteristic of a crystal. This gives rise to the unique properties of the liquid phase, where molecules are able to flow and change the bulk shape to fit a container. The ability to flow on the macro scale is a direct result of the low ordering on the atomic scale and the subsequent much greater diffusion potential of a liquid phase compared to a solid phase. In a liquid, atoms are not stuck in specific crystallographic sites and therefore have the ability to diffuse to fill space in the most efficient way. However, when liquids are confined and in contact with a solid surface, often many new behaviors are observed as a result of different thermodynamic driving forces compared to the bulk. For example, many confined liquids exhibit new phases that are influenced by the surface they are in contact with[1] that leads to changes in properties such as enthalpies of adsorption[2] and surface tension of the liquids[3]. In some extreme cases, such as water confined in carbon nanotubes, flow rates have been experimentally observed that are up to 5 orders of magnitude faster in the confined phase[4,5].

In order to understand these flow properties, the diffusion cannot be thought of as a typical, random walk driven process. Diffusion modeled as a random walk process produces an equation as follows:

$$MSD = 2nDt$$

Where MSD is the mean square displacement of a given atom, n is the dimensionality of the system, D is the diffusion coefficient, and t is the time over which the MSD is measured. In this most basic model of diffusion, lowering the dimensionality, i.e. going from 3D bulk to 2D or 1D confinement, will result in less diffusion as there are fewer degrees of freedom for the random walk to occur in. However, in the case of water in carbon nanotubes, we see that the opposite holds true; confining the water to 1 dimension actually increases diffusion by orders of magnitude[4,6,7].

Many different computational and experimental studies have been performed to fully understand the case of water diffusion in carbon nanotubes. The majority of these studies show that the hydrophobic carbon nanotubes provide a non-interacting surface for the water to flow through[8,9], which allows for the water to restructure and form fast diffusing regions close to the wall[10,11]. However, this leads to complicated behavior where the diffusivity greatly depends on the diameter of the nanotube, and indeed, studies have found that distinct structures exist for different levels of confinement. In extremely confined (<1 nm diameter) nanotubes, water forms a single file chain and diffuses 4-5 orders of magnitude faster than bulk[8]. In larger nanotubes (>1 nm), the water forms into distinct phases, an outer phase ordered by the wall and an inner phase resembling the single file chain[12,13]. Each of these phases diffuses separately, but the net result is still diffusion greater than bulk. Eventually, as the diameter of the nanotube becomes large enough (4+ nm), the diffusivity of the confined water approaches bulk values[14]. Importantly, all of these diffusion behaviors are driven by two observations, the lack of water interaction with the carbon nanotube walls, and the subsequent formation of complex hydrogen bonding networks.

4.1 Understanding 2D confined diffusion

These observations are critically important to understanding confined diffusion in this system, as it suggests that the root cause of interesting diffusion behaviors are either wall-molecule or molecule-molecule chemical interactions. In bulk systems, the wall-molecule interactions are far less important, but as systems become more confined, those wall-molecule interactions begin to dominate the diffusion behavior of the system. However, these interactions are only well studied for water in carbon nanotube systems, and are far less studied for other molecular and 2D systems. Therefore, by looking at wall-molecule and molecule-molecule interactions, we hope to generalize our understanding of confined systems to be able to predict diffusion properties in the superlattice system presented in Chapter 3 of this dissertation.

4.1.1 Solid-liquid phase transitions in confined systems

Because it is difficult to deconvolute the contributions of wall-molecule and molecule-molecule interactions, there are few studies that directly quantify these values. However, a proxy that can used for these interactions is the melting point of the confined liquid, as a solid-liquid phase transition (i.e. a melting event) is essentially a transition where the molecule-molecule interactions change from an ordered type of interaction (solid), to a much less ordered type (liquid). Additionally, melting point can also serve as a proxy for diffusivity, as solids have a much lower diffusivity than liquids. Typically, melting point studies of confined liquids have similar findings, where the melting point of the confined liquid is depressed to a lower temperature. These studies find that confinement disrupts the formation of ordered solids, which means that the liquid cannot freeze[1]. The exceptions to this rule are when the wall-molecule interactions are extremely large and when there are complex mixtures[15,16]. In both of these cases, either the strong interactions

with the walls or between components of the mixture induce greater ordering, and can therefore increase the melting point of the confined liquid.

However, the idea of melting or freezing in 2D is not as simple as in 3D. In 3D, a bulk solid is characterized by long range order, whereas a bulk liquid is characterized by no long range order[17,18]. In 2D, these ideas of long range order still hold true for solids, but the idea of a liquid phase is much more complicated as both orientational and translational order must be considered, and these two types of order are not necessarily linked. When a liquid is confined in a plane, there is an intermediate phase between a crystal and an isotropic liquid; an anisotropic liquid-crystal called a hexatic phase[19,20]. In a hexatic phase, similar to an isotropic liquid, there is no/little short range translational order. Unlike an isotropic liquid however, there is some long range orientational order where quite often, molecules form patterns with 6 fold symmetry (e.g. hexagons). In these systems, the process of melting is described by KTHNY theory, which states that 2D melting of a solid phase requires two phase transitions. First, a solid crystal transitions into a hexatic liquid, and then second, the hexatic liquid transitions to an isotropic liquid[19,20].

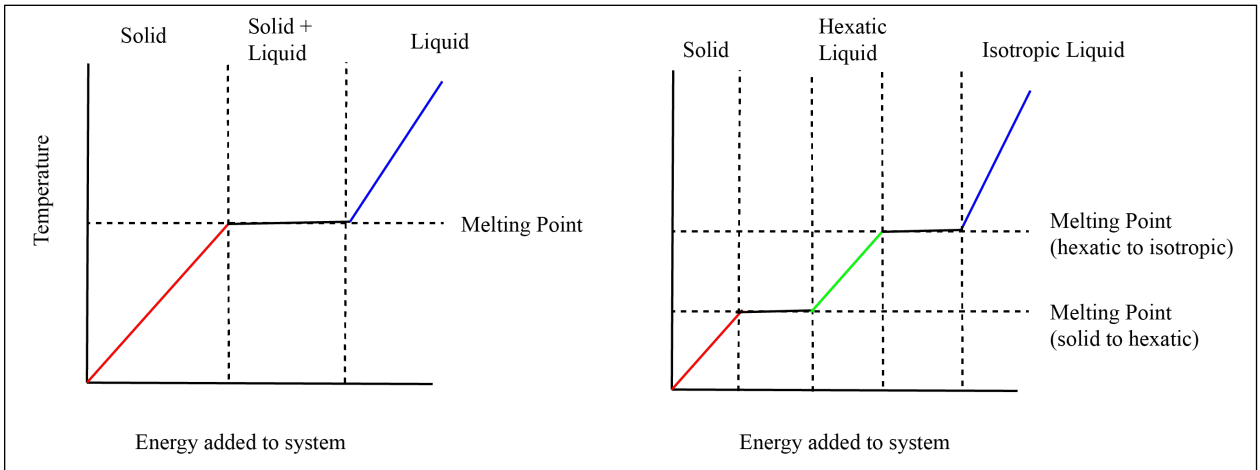


Figure 1: Energy diagrams of melting in a bulk (left) and 2D confined (right) systems. Plateaus in temperature for both the bulk and confined systems are indicative of phase changes, as energy is being used to melt the system rather than increase the average temperature. Interestingly, confined solids (right) have two distinct phase transitions whereas bulk solids (left) have only one.

Typically, 2D solids maximize packing density by packing in a hexagonal pattern. The first phase transition begins with the breakdown of long range translational order (e.g. the formation of dislocations by shearing a crystal plane). These dislocations can then pair together and cause the formation of a disclination, which is a breakdown in the orientational ordering of the crystal. For example, in a typical hexatic phase, each molecule has 6 nearest neighbors, but after a dislocation pair degrades into a disclination, a pair of molecules will have 5 and 7 neighbors instead. As this process occurs throughout the crystal, eventually both orientational and translational order will disappear and only an isotropic liquid will be left.

Because of the existence of a hexatic phase, the definition of a liquid phase in two dimensions is not as straightforward as in the bulk. This also complicates the analysis of such systems, as the properties of the confined system will not directly mirror those of the bulk system. However, there are still many properties that can be measured, such as diffusion coefficients, enthalpies of solvation, and order parameters, all of which can help us to understand these systems.

4.2 Understanding the confinement in the superlattice system

As previously noted in the example of water in carbon nanotubes, carbon nanotubes are hydrophobic and therefore weakly interacting with water. In systems where the carbon nanotubes are functionalized to make them more hydrophilic, the diffusion of the confined water greatly decreases, even becoming lower than bulk water[21]. These systems are much less interesting from a materials design perspective, as the main lesson that can be learned is that strong interactions lead to slow mass transport, and therefore weakly interacting systems are more desirable. In these weakly interacting systems, it is critical to understand the root cause of deviations from bulk behavior, but there are not very many examples of weakly interacting solid systems with a

combination of a confined and stationary phase. In the case of water in carbon nanotubes, the interesting diffusion properties are brought about by confinement effects on the structure of the water inside the nanotubes. However, water is an extremely polar molecule and is not necessarily a good model system for understanding how other chemically interesting molecules will behave when confined. Additionally, the 1D geometry of a carbon nanotube is quite different than the 2D geometry of our TMDC superlattice system, so making comparisons between the two systems is not necessarily straightforward. Therefore, it is the goal of this work to develop general understandings of how confined molecules behave and generate predictive power over the properties of novel confined molecule-material systems.

4.2.1 Two case studies demonstrating different types of confined diffusion

The 2D material-molecule superlattice described in Chapter 3 of this dissertation is a unique type of confined system for two main reasons. Firstly, the structure is held together purely by van der Waals interactions, so much like in the water-carbon nanotube system, the interactions between the molecular phase and the 2D material phase are weak. Secondly, the geometry of our system is planar, which means that the confinement effects we can look at are going to be quite different from those associated with 1D systems. Combined with the fact that we can insert almost any molecule experimentally, this superlattice system offers a relevant opportunity to theoretically understand how confinement in two dimensions to a hexatic phase changes the properties of molecules. The

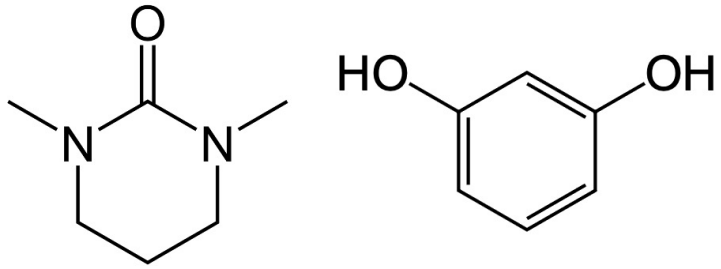


Figure 2: Molecular structure of DMPU and resorcinol. We have reported the experimental fabrication of superlattices with both molecules[22], which lead us to choose them for further computational study.

following section will contain two case studies of confined molecules, looking at the molecules DMPU and resorcinol (Figure 2).

Our initial calculations of the superlattice structure (Chapter 3) suggest that the molecular phase sits parallel to the 2D material in the superlattice, with only small deviations in dipole angle (typically < 20°). This geometry is a direct result of the planar confinement, and furthers our hypothesis that the molecular phase is only weakly interacting with the 2D material layer. Because of this similarity between our system and the water confined in carbon nanotubes, we began our computational exploration of the superlattice system by measuring the confined diffusion coefficients of DMPU, one of the first superlattice systems we had experimentally assembled. In order to study this system, we performed MD simulations on systems of roughly 2,000 molecules either confined between two, 10 nm MoS_2 sheets or in the bulk. For these confined simulations, we used LAMMPS to measure the MSD of the DMPU molecules confined in the middle 70 Å of the MoS_2 layers, so as to avoid measuring molecules that diffused outside of the confinement of the MoS_2. Additionally, we allowed the interlayer to equilibrate with a well of bulk molecules in order to ensure the proper packing density (See Chapter 2 for more details). The MSD was then used to calculate a diffusion coefficient and plotted vs the inverse of temperature.

By looking at the Arrhenius plot of temperature vs diffusion coefficient, we see that the 2D confined DMPU has quite different qualitative behavior than the bulk DMPU (Figure 3). The first feature of note is the melting point, which we see decreases from 250 K to 150 K. This observation is well reported in the literature[23–25], and is most likely a result of the confinement stopping the ideal bulk crystal structure from forming. Because of this observation, we would suspect that the diffusion of the 2D phase should be much greater than the 3D phase within this temperature regime. Indeed, we find that there is up to a 2 order of magnitude increase in confined diffusion

with the largest difference at 240 K. This makes sense as 240 K is the warmest temperature we surveyed where the bulk phase should be solid and the 2D phase should be liquid.

More interesting than that however, is the regime where both the bulk phase and the confined phase are liquids (T > 250 K). In this region, the bulk diffusion coefficient is increasing at a much greater rate than the confined diffusion coefficient. We attribute this observation to the fact that bulk DMPU has more degrees of freedom than in the confined system. In the bulk, molecules can move in the x, y, and z directions, whereas in confinement, the molecules can only move in the x and y directions. This means that the addition of more thermal energy adds more possibilities for motion in the bulk system than in the confined system, and therefore the diffusion coefficient will increase more upon adding the same amount of energy. However, up until 330 K, the confined phase still has a greater diffusion coefficient than the bulk phase. This indicates that the greater diffusion of the confined phase is not purely due to difference between solid and liquid diffusion, but due to other factors, such as a change in the structure of the confined DMPU phase.

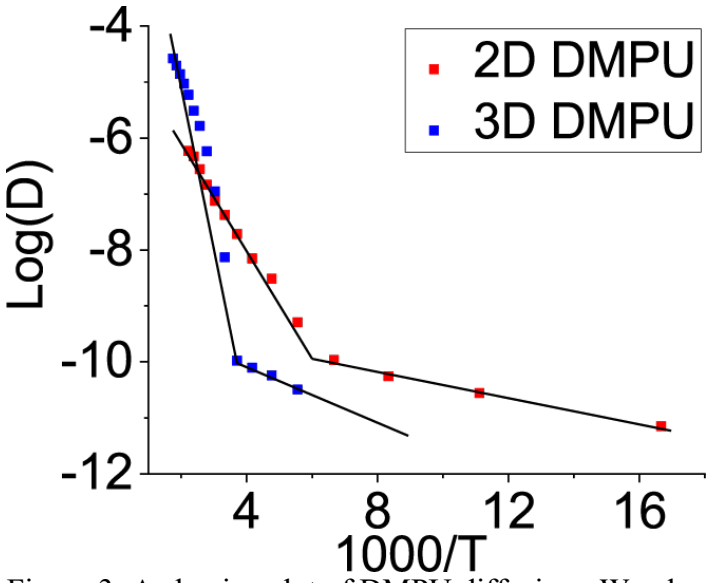


Figure 3: Arrhenius plot of DMPU diffusion. We observe that the 3D bulk and 2D confined phases exhbit markedly different behavior, and there is a large temperature region where the confined phase diffuses faster than the bulk phase.

The final points of interest on these plots are the y-intercepts of the two trendlines. The y-intercepts of the lines represent the theoretical upper limits of diffusion at infinite temperature.

What we can qualitatively observe from the plot is that the bulk DMPU phase will have a much larger y-intercept than the confined DMPU, suggesting that it is more difficult to initiate a diffusion event in the confined system than the bulk system. Most likely this is due to the fewer degrees of freedom available in 2D compared to 3D. When thinking about what will initiate an individual diffusion event, there has to be enough space for a molecule to translate into a different site, and the fewer degrees of freedom in 2D relative to the bulk makes it less likely for the confined system to initiate that translation. Finally, it is also worth noting that the closer the high temperature points get to the melting point, the less linear the slope becomes. This is most likely due to the partial freezing of the system, and is an artifact of the simulations.

In that first simulation, we observe one type of confined behavior where the confined phase diffuses significantly faster than the bulk phase across certain temperature regimes. There are many reasons why we might observe this behavior, but one possibility hinted at by the observed melting point depression is that confined DMPU loses stabilizing interactions relative to the bulk phase. Under confinement, ideal stabilizing interactions may not be available which therefore causes the confined diffusion to be significantly greater than the bulk. In order to test this hypothesis we decided to next model a molecule that should be able to have strong IMFs under confinement. When thinking about an ideal molecule, we wanted a flat molecule that would have peripheral groups that could strongly interact without needing a 3D geometry. This led us to resorcinol, a molecule which is held planar by an aromatic ring and is capable of forming a hydrogen bonding network in 2D. However, resorcinol is also an interesting analogue to water, as the primary intermolecular interactions will be hydrogen bonding, and if this system is analogous to the carbon nanotube system, then we might expect to see greater confined diffusion.

Interestingly, when we measure the diffusion coefficients of resorcinol, we find quite different qualitative behavior than in DMPU (Figure 4). Looking at the Arrhenius plots of confined vs bulk diffusion for resorcinol, we find that across most temperatures, confined resorcinol diffuses about 2 orders of magnitude slower than bulk resorcinol. The bulk and confined diffusion coefficients converge at around the freezing point of the molecules. We suspect this is due to both solid phases having relatively little motion, and both phases can mostly be thought of as crystalline.

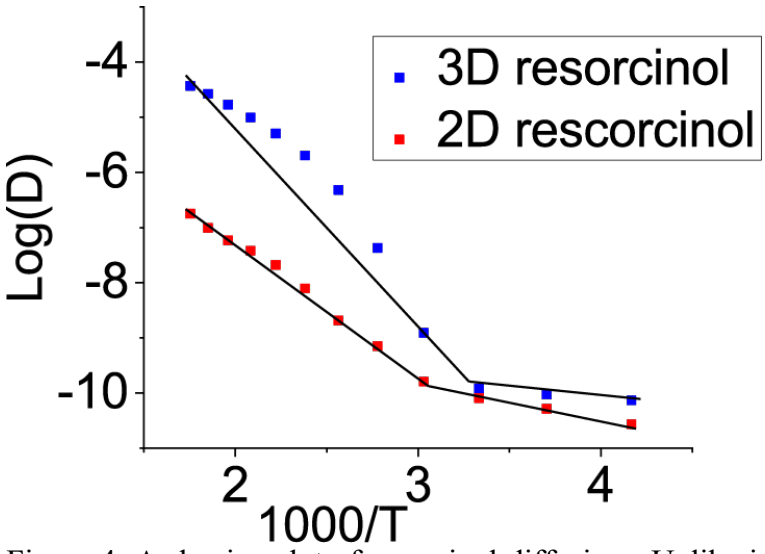


Figure 4: Arrhenius plot of resorcinol diffusion. Unlike in the case of DMPU, across all temperature, the confined phase diffuses slower than the bulk phase.

When looking at the melting points of the bulk and confined phase, we see that they are roughly the same, both occurring around the 360 K temperature point. This is in sharp contrast to DMPU, which exhibits a 100 K depression in melting point. This lack of melting point depression suggests that the confined resorcinol phase is able to crystalize well despite the confinement, which supports our idea that the resorcinol can form a stable 2D phase. Because the interactions between the resorcinol and MoS_2 are not strong, it is most likely intermolecular interactions between resorcinol molecules that are stabilizing the confined solid. Conceptually, this would indicate the formation of a 2D hydrogen bonding network, or a phase with equivalently strong interactions.

4.2.2 Solvation energies of DMPU and resorcinol

In order to quantify these interactions, we decided to use self-solvation energy (ΔG_{vap}), which is the energy to remove a single molecule from a bulk solution. This self-solvation energy calculation is based on a recently reported alchemical decoupling method[26] for removing a molecule into the gas phase. This calculation leverages a free energy perturbation calculation to remove a molecule from the simulation in a piecewise way via a scaling parameter (λ). The calculation works on the assumption that the energy of the system can be described by this set of equations:

(1) $U(\lambda) = U_{bg} + U_1(\lambda) + U_0(\lambda)$,when

(2) $\lambda = 0$, $U = U_{bg} + U_0$, and when

(3) $\lambda = 1$, $U = U_{bg} + U_1$

Where the total energy of the system is the sum of a background term U_{bg} that is unaffected by the λ parameter, a $U_1(\lambda)$ term describing the interactions of the atoms to be perturbed before applying the scaling parameter, and a $U_0(\lambda)$ term describing the interactions after perturbation. When the λ parameter is at either extreme, fully scaling interactions (equation 2) or fully turning them off (equation 3), the energy of the system will be equal only to the $U_{bg} + U_{1 \text{ or } 0}$ depending on the value of λ. Conceptually, the λ parameter is a scaling of the forcefields, where the forcefields are simply multiplied by a factor of $(1 - \lambda)$. Scaling λ to 0 can be thought of as leaving the system unperturbed, so all molecules are interacting as their force fields would dictate. Scaling λ to 1 has the opposite effect, where molecules will be interacting as though their forcefield were multiplied by a factor of 0, or essentially the molecule is not interacting. The idea behind the simulations is that when the molecular interactions are fully turned off, then it is equivalent to removing a molecule into the gas phase. The difference in energy between that system and the system where

the molecular interactions are fully turned on is therefore the same as the energy to evaporate a molecule into the gas phase from the liquid phase, which is simply the solvation energy.

We assembled a simulation box consisting of two 10 nm x 10 nm MoS_2 monolayers separated by 10 Å, packed with between 150 and 250 molecules each (See Chapter 2 for more details). We then used the decoupling approach to turn off the interactions of one of the confined molecules, and using this method, we calculated the self-solvation energies for both DMPU and resorcinol (Table 1). For the case of DMPU, we found that the 2D solvation energy was an order of magnitude lower than the bulk (3D) solvation energy. We observed the opposite effect with resorcinol, where the 2D and bulk solvation energies were roughly the same, even being slightly higher in the confined phase. These observations offer an explanation for the two different types of diffusion behavior shown in figures 3 and 4, where molecules like DMPU that diffuse faster across some temperatures in 2D have weaker intermolecular forces under confinement while molecules like resorcinol that diffuse slower in confinement have stronger intermolecular forces.

Table 1: Solvation energies of DMPU and resorcinol

	DMPU	Resorcinol
3D ΔG_{vap} (kcal/mol)	-9.48	-13.22
2D ΔG_{vap} (kcal/mol)	-0.99	-13.98

For DMPU, the 2D phase diffuses faster across certain temperature regimes as the 2D liquid loses the primary intermolecular force that stabilizes the bulk liquid. Looking at neutron scattering studies on the structure of the closely related liquid NMP, we see that the local order of bulk NMP is controlled predominantly by dipole-dipole interactions[27]. In these interactions, NMP molecules form stacks where C=O double bonds align antiparallel and molecules sit ~4-6 Å apart. Additionally, this study found that edge-edge hydrogen bonding interactions of NMP only minimally contributed to the local liquid structure. Because DMPU is a symmetrical version of

NMP with an additional -NCH_3 group, we believe that these effects should also exist in the DMPU liquid, and could potential even be greater due to the two N-C=O bonds of DMPU (Figures 2, 5). However, when these liquids are confined, these stacking sequences are not possible, as the free interlayer space is only 4 Å tall. The only intermolecular interactions available for the confined molecules are therefore the weak edge-edge interactions. This is reflected in the order of magnitude decrease in solvation energy, which subsequently leads to a much greater confined diffusion coefficient.

In resorcinol however, we observe that the bulk and 2D solvation energies are roughly similar, with the bulk solvation energy being only ~5% greater than the confined energy. We hypothesize that this is due to the ability of the resorcinol molecule to have strong edge-edge interactions that can persist in the 2D plane. Resorcinol has two primary crystalline phases as a bulk solid, the less dense α phase and the more dense ß phase[28]. Upon compression, the α phase turns into the ß phase, and we note that the hydrogen bonding in the α phase involves out of plane

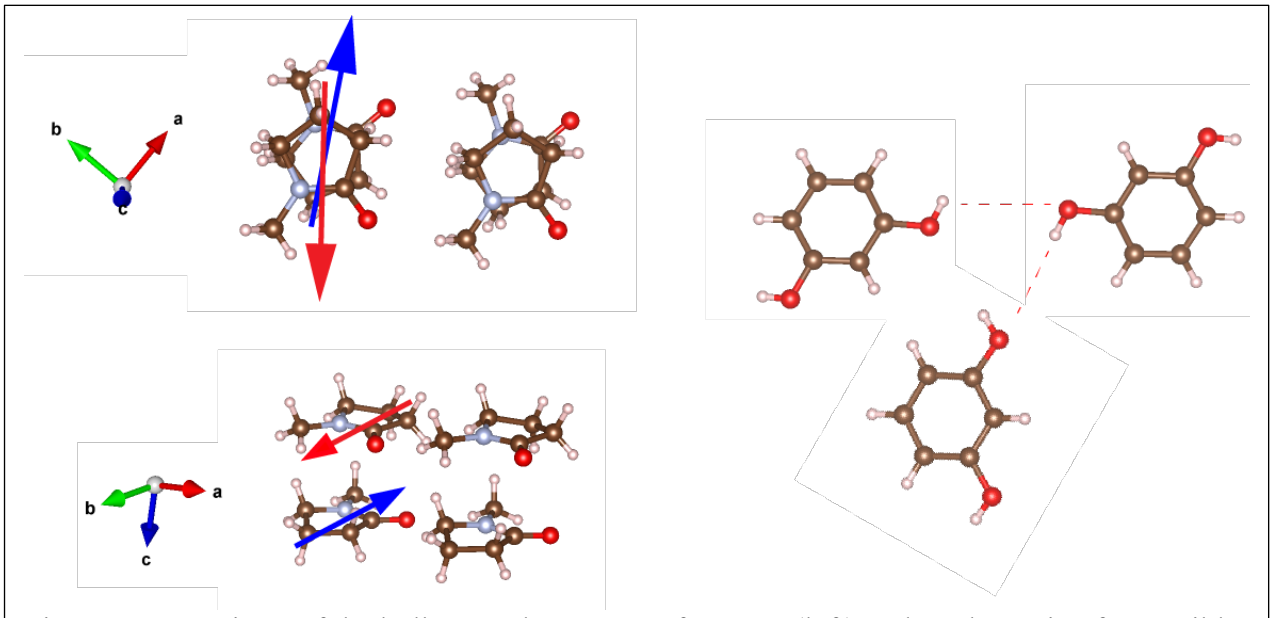


Figure 5: Two views of the bulk crystal structure of DMPU (left) and a schematic of a possible hydrogen bonding network for confined resorcinol (right). In 3D frozen DMPU, the dipoles align antiparallel in a uniquely 3D interaction. Resorcinol however can have hydrogen bonding interactions in either 2D or 3D as shown on the right.

hydrogen bonding, while the ß phase is primarily stacks of linearly hydrogen bound resorcinol[28]. Based on the similarity of the confined and bulk solvation energy values, it is likely that the confinement induces the formation of a ß-like crystalline phase with an in-plane hydrogen bonding network (Figure 5). These in plane interactions are quite strong, and result in the confined phase having slightly higher intermolecular forces than the bulk phase, which results in both the slower confined diffusion and similarity in melting points between the bulk and confined phases. Indeed when we look at the molecular dynamics, we see that qualitatively this network exists in the hexatic liquid (Appendix 2).

Taken together, the case studies of DMPU and resorcinol suggest that the properties of confined liquids can vary greatly depending on how confinement effects the resulting structure of the liquid. For some molecules where the bulk liquid structure is predominantly controlled by out of plane interactions (NMP, DMPU), the loss of these interactions will greatly destabilize the confined phase and could result in properties such as increased confined diffusion. For other molecules which are able to have strong interactions in a 2D plane due to highly interacting edge groups, we observe that the 2D liquid phase is slightly more stable than the bulk phase which will result in slower confined diffusion.

4.3 Shape effects on confined liquids

In addition to the specific examples of DMPU and resorcinol to understand how intermolecular forces effect confined diffusion, I have also conducted a study to understand how shape effects broadly impact diffusion. We hypothesized that when confined into two dimensions, shape effects would play a much larger role in determining properties than in bulk systems due to the presence of the intermediate hexatic phase between the 2D liquid and 2D solid. This phase

relies on having a high degree of both orientational and translational order to form, and therefore the suppression of this phase by suppressing 6-fold order is a potential avenue to enhance 2D diffusivity by promoting an isotropic liquid phase and disrupting the more ordered phases.

To test this hypothesis, we tested both the 2D and 3D diffusion of a variety of benzene derivatives functionalized with increasingly bulky groups. We found that if the substituent were an ethyl, methyl, or hydrogen group, then the 3D diffusion tended to be greater than the 2D diffusion across all temperature ranges. With carbon chains bulkier than an ethyl group, there were certain temperature regimes where the confined diffusion was faster than the bulk diffusion (Appendix 2). This was especially true at lower temperatures, where the bulky side group disrupted the formation of a hexatic phase from forming (i.e. depressed the melting point). This observation is in agreement with literature results which suggest that shapes that cannot tile nicely tend to form less ordered confined phases, and in some cases, won't form a hexatic phase at all during the melting process[29].

Conclusions and Outlook

In this work, we demonstrate that two distinct types of confined behavior exist for 2 dimensionally confined liquids. The first type of behavior involves an increase in diffusion upon confinement. Unlike previous work which suggests that this is only the case due to a decrease in the melting point of the confined liquid, we find that there is a significant temperature regime (~100 K) where both the confined and bulk phase are liquid and the confined phase still has greater diffusion. Additionally, because our system has only weak interactions between the molecular phase and the boundary phase (MoS_2), the observation of greater diffusion must be attributed to a specific feature of the molecular phase. By using solvation energy calculations, we find that the

energy to remove a molecule from the confined phase is an order of magnitude lower than the energy to remove a molecule from the bulk phase. We justify this observation by noting how the primary interactions in the bulk crystal are out of plane, dipole-dipole interactions that cannot exist when the molecule is confined. The loss of these interactions is therefore the most likely driver of the increased diffusion in the confined phase. Conversely, in the other type of confined behavior, we find that across all temperature regimes the bulk phase diffuses more than the confined phase. When we perform solvation energy calculations on these phases, we find that the confined phase has slightly stronger interactions than the bulk phase. By looking at the crystal structure of the bulk solvents, we find that it is possible to still have strong interactions when confined into a 2D plane. Due to edge-edge interactions such as hydrogen bonding between peripheral groups, the 2D phase is actually forced into a slightly more stable configuration than the bulk liquid which leads to reduced diffusion across all temperatures.

While this work focuses on the case studies of DMPU and resorcinol, it shows that understanding confined liquid properties is more complicated than previous models suggest. Our work suggests that the most important factors that inform the properties of the confined phase is the ability of the molecule to have strong edge-edge interactions, which is not an idea that has been previously reported in studies of confined liquids. In particular, using solvation energy as a proxy for these interactions may offer opportunities for predicting unusual behavior. These methods represent the first steps in generally developing a model for understanding the properties of confined phases in a variety of systems. By expanding upon these initial studies, it may even be possible to develop predictive power for a variety of confined geometries and types of molecules.

REFERENCES

(1) Gubbins, K. E.; Long, Y.; Śliwinska-Bartkowiak, M. Thermodynamics of Confined Nano-Phases. *J. Chem. Thermodyn.* **2014**, *74*, 169–183. DOI: 10.1016/j.jct.2014.01.024.

(2) Torres-Knoop, A.; Poursaeidesfahani, A.; Vlugt, T. J. H.; Dubbeldam, D. Behavior of the Enthalpy of Adsorption in Nanoporous Materials Close to Saturation Conditions. *J. Chem. Theory Comput.* **2017**, *13* (7), 3326–3339. DOI: 10.1021/acs.jctc.6b01193.

(3) Singh, S. K.; Sinha, A.; Deo, G.; Singh, J. K. Vapor−liquid Phase Coexistence, Critical Properties, and Surface Tension of Confined Alkanes. *J. Phys. Chem. C* **2009**, *113* (17), 7170–7180. DOI: 10.1021/jp8073915.

(4) Holt, J. K.; Park, H. G.; Wang, Y.; Stadermann, M.; Artyukhin, A. B.; Grigoropoulos, C. P.; Noy, A.; Bakajin, O. Fast Mass Transport through Sub-2-Nanometer Carbon Nanotubes. *Science* **2006**, *312* (5776), 1034–1037. DOI: 10.1126/science.1126298.

(5) Majumder, M.; Chopra, N.; Andrews, R.; Hinds, B. J. Enhanced Flow in Carbon Nanotubes. *Nature* **2005**, *438* (7064), 44–44. DOI: 10.1038/438044a.

(6) Qin, X.; Yuan, Q.; Zhao, Y.; Xie, S.; Liu, Z. Measurement of the Rate of Water Translocation through Carbon Nanotubes. *Nano Lett.* **2011**, *11* (5), 2173–2177. DOI: 10.1021/nl200843g.

(7) Chatzichristos, A.; Hassan, J. Current Understanding of Water Properties inside Carbon Nanotubes. *Nanomaterials (Basel)* **2022**, *12* (1). DOI: 10.3390/nano12010174.

(8) Hummer, G.; Rasaiah, J. C.; Noworyta, J. P. Water Conduction through the Hydrophobic Channel of a Carbon Nanotube. *Nature* **2001**, *414* (6860), 188–190. DOI: 10.1038/35102535.

(9) Melillo, M.; Zhu, F.; Snyder, M. A.; Mittal, J. Water Transport through Nanotubes with Varying Interaction Strength between Tube Wall and Water. *J. Phys. Chem. Lett.* **2011**, *2* (23), 2978–2983. DOI: 10.1021/jz2012319.

(10) Srivastava, A.; Hassan, J.; Homouz, D. Effect of Size and Temperature on Water Dynamics inside Carbon Nano-Tubes Studied by Molecular Dynamics Simulation. *Molecules* **2021**, *26* (20). DOI: 10.3390/molecules26206175.

(11) Hassan, J.; Diamantopoulos, G.; Gkoura, L.; Karagianni, M.; Alhassan, S.; Kumar, S. V.; Katsiotis, M. S.; Karagiannis, T.; Fardis, M.; Panopoulos, N.; Kim, H. J.; Beazi-Katsioti, M.; Papavassiliou, G. Ultrafast Stratified Diffusion of Water Inside Carbon Nanotubes; Direct Experimental Evidence with 2D$D-T_2$ NMR Spectroscopy. *J. Phys. Chem. C* **2018**, *122* (19), 10600–10606. DOI: 10.1021/acs.jpcc.8b01377.

(12) Koga, K.; Gao, G. T.; Tanaka, H.; Zeng, X. C. Formation of Ordered Ice Nanotubes inside Carbon Nanotubes. *Nature* **2001**, *412* (6849), 802–805. DOI: 10.1038/35090532.

(13) Joseph, S.; Aluru, N. R. Why Are Carbon Nanotubes Fast Transporters of Water? *Nano Lett.* **2008**, *8* (2), 452–458. DOI: 10.1021/nl072385q.

(14) Farimani, A. B.; Aluru, N. R. Spatial Diffusion of Water in Carbon Nanotubes: From Fickian to Ballistic Motion. *J. Phys. Chem. B* **2011**, *115* (42), 12145–12149. DOI: 10.1021/jp205877b.

(15) Ueda, T.; Omichi, H.; Chen, Y.; Kobayashi, H.; Kubota, O.; Miyakubo, K.; Eguchi, T. Two-Dimensional Melting and Phase Change of Binary Mixtures of CCl_4 and $CHCl_3$ Confined in ACF Nanospace Studied Using Solid-State^1 H NMR. *Bull Chem Soc Jpn* **2010**, *83* (11), 1323–1332. DOI: 10.1246/bcsj.20100169.

(16) Klein, J.; Kumacheva, E. Confinement-Induced Phase Transitions in Simple Liquids. *Science* **1995**, *269* (5225), 816–819. DOI: 10.1126/science.269.5225.816.

(17) Kosterlitz, J. M.; Thouless, D. J. Ordering, Metastability and Phase Transitions in Two-Dimensional Systems. In *Basic notions of condensed matter physics*; Anderson, P. W., Ed.; CRC Press, 2018; pp 493–515. DOI: 10.4324/9780429494116-24.

(18) Kosterlitz, J. M.; Thouless, D. J. Long Range Order and Metastability in Two Dimensional Solids and Superfluids. (Application of Dislocation Theory). *J. Phys. C: Solid State Phys.* **1972**, *5* (11), L124–L126. DOI: 10.1088/0022-3719/5/11/002.

(19) Nelson, D. R.; Halperin, B. I. Dislocation-Mediated Melting in Two Dimensions. *Phys. Rev. B* **1979**, *19* (5), 2457–2484. DOI: 10.1103/PhysRevB.19.2457.

(20) Halperin, B. I.; Nelson, D. R. Theory of Two-Dimensional Melting. *Phys. Rev. Lett* **1978**, *41* (2), 121–124. DOI: 10.1103/PhysRevLett.41.121.

(21) Majumder, M.; Corry, B. Anomalous Decline of Water Transport in Covalently Modified Carbon Nanotube Membranes. *Chem. Commun.* **2011**, *47* (27), 7683–7685. DOI: 10.1039/c1cc11134e.

(22) Peterson, D. A.; Farnsworth, T. W.; Woomer, A. H.; Fishman, Z. S.; Shapiro, S. H.; Radomsky, R. C.; Barron, E. A.; Thompson, J. R.; Warren, S. C. Generalized Assembly of Semiconductor–Molecule Superlattices. *Chem. Mater.* **2025**, *37* (1), 119–128. DOI: 10.1021/acs.chemmater.4c02165.

(23) Alba-Simionesco, C.; Coasne, B.; Dosseh, G.; Dudziak, G.; Gubbins, K. E.; Radhakrishnan, R.; Sliwinska-Bartkowiak, M. Effects of Confinement on Freezing and Melting. *J. Phys. Condens. Matter* **2006**, *18* (6), R15-68. DOI: 10.1088/0953-8984/18/6/R01.

(24) Sliwinska-Bartkowiak, M.; Jazdzewska, M.; Huang, L. L.; Gubbins, K. E. Melting Behavior of Water in Cylindrical Pores: Carbon Nanotubes and Silica Glasses. *Phys. Chem. Chem. Phys.* **2008**, *10* (32), 4909–4919. DOI: 10.1039/b808246d.

(25) Jackson, C. L.; McKenna, G. B. The Melting Behavior of Organic Materials Confined in Porous Solids. *J. Chem. Phys.* **1990**, *93* (12), 9002–9011. DOI: 10.1063/1.459240.

(26) Khanna, V.; Monroe, J. I.; Doherty, M. F.; Peters, B. Performing Solvation Free Energy Calculations in LAMMPS Using the Decoupling Approach. *J. Comput. Aided Mol. Des.* **2020**, *34* (6), 641–646. DOI: 10.1007/s10822-020-00303-3.

(27) Basma, N. S.; Headen, T. F.; Shaffer, M. S. P.; Skipper, N. T.; Howard, C. A. Local Structure and Polar Order in Liquid N-Methyl-2-Pyrrolidone (NMP). *J. Phys. Chem. B* **2018**, *122* (38), 8963–8971. DOI: 10.1021/acs.jpcb.8b08020.

(28) Cook, C.; McKinley, J. L.; Beran, G. J. O. Modeling the α- and β-Resorcinol Phase Boundary via Combination of Density Functional Theory and Density Functional Tight-Binding. *J. Chem. Phys.* **2021**, *154* (13), 134109. DOI: 10.1063/5.0044385.

(29) Anderson, J. A.; Antonaglia, J.; Millan, J. A.; Engel, M.; Glotzer, S. C. Shape and Symmetry Determine Two-Dimensional Melting Transitions of Hard Regular Polygons. *Phys. Rev. X* **2017**, *7* (2), 021001. DOI: 10.1103/PhysRevX.7.021001.

CHAPTER FIVE – SUPERLATTICE USES AS ION STORAGE DEVICES AND MEMBRANES

Introduction

In devices such as novel battery and membrane materials, slow mass transport is often a critical problem that limits widespread adoption of new advances. This problem is particularly exacerbated in layered materials, as the confinement of the layered structure typically impedes intercalation[1]. However, our work on flow in confined systems suggests that there are certain types of systems where confined diffusion can actually be greater than bulk diffusion, particularly with weakly interacting liquids. These weakly interacting systems offer unique opportunities to develop new devices such as membranes or capacitors, as the enhanced flow unique to the superlattice structure can potentially be used to bring in ionic species in conditions where bulk materials might be unreactive. In this work, we present a case study using our superlattice material to intercalate both SO_4 and PO_4 ions. We demonstrate the ability to intercalate these ions under aqueous conditions where the bulk material is unreactive. The intercalation of PO_4 is also especially noteworthy, as typically many similar systems cannot intercalate PO_4. Additionally, we demonstrate that the intercalation conditions are mild enough that we are able to intercalate the superlattice before the onset of oxygen evolution, demonstrating a novel method for incorporating anions into MoS_2.

5.1 Aqueous batteries

As we attempt to diversify our energy portfolio from fossil fuels, renewable energy sources such as solar and wind are making up an increasingly large part of the world's energy infrastructure. However, unlike nonrenewable energy sources, solar and wind cannot be produced on demand, and therefore suffer consistency problems which greatly limit the ability to transition to a renewable based system. In order to develop sustainable energy infrastructure, better methods of grid scale energy storage are needed. While current battery technologies work well for small devices, components are both too expensive and not stable enough to develop grid scale batteries based on current technologies.

Batteries with aqueous electrolytes, however, offer a potential solution to both the expensive nature of lithium and cobalt and the stability issues that these elements suffer from. Working with water based electrolytes however does present a different set of challenges, as water is extremely reactive under electrochemical conditions. In addition to electrochemical splitting leading to hydrogen and oxygen evolution reactions, water also tends to oxidize many typical types of electrodes making them unsuitable for direct adaptation to an aqueous battery[2,3]. In order to develop these aqueous battery systems, work needs to be done to both produce electrodes that are electrochemically stable in water and understand the sorts of ion systems that will work for an aqueous battery.

Aqueous battery systems offer many advantages over the ubiquitous lithium battery systems. In addition to the high costs associated with lithium and cobalt, aqueous batteries are also far less hazardous than typical systems. Typical batteries contain an organic electrolyte, which tends to be flammable and can fail catastrophically causing fires, explosions, and potential exposures to dangerous solvents[3]. Aqueous batteries remedy this by replacing the electrolyte with a mixture of water and an ion system, which in addition to being nonvolatile, is also much less

likely to contain toxic components. In addition to the safety components, aqueous batteries also offer distinct functional advantages, such as high ionic conductivity. Compared to organic electrolytes, aqueous electrolytes offer ionic conductivities orders of magnitude higher[4], which allows for the development of fast charging/discharging battery systems that are reliable at lower temperatures[5,6].

However, aqueous battery systems also come with a distinct set of disadvantages, namely related to the use of water as an electrolyte component. The primary disadvantage of using water is that the electrochemical stability window is quite low, as both oxidation and reduction can cause splitting into oxygen and hydrogen gas respectively. The electrochemical stability window of water is the primary problem with aqueous batteries, as the low stability greatly limits the types of ions and electrodes that can be used. For example, graphite, which is a ubiquitous anode in standard lithium ion batteries, does not work well for aqueous batteries. Graphite in water is typically only able to be intercalated under extreme conditions, such as in concentrated sulfuric or hydrochloric acid[7–9]. The few studies that do intercalate graphite at neutral pH's demonstrate oxidative damage to the electrodes which greatly limits their cyclability[10]. Many common cathode materials, such as lithium cobalt oxide, also require extensive modification in order to be used in aqueous systems as water is much more corrosive than typical organic electrolytes[11].

This lack of suitable electrode materials has been identified as one of the main research interests in developing aqueous battery materials[2]. Of the materials currently being studied, layered materials are a promising candidate for aqueous electrodes, as their high theoretical capacity and relative stability make them an ideal structure type. Materials such as MoS_2 and V_2O_5 have been used as cathodes in zinc ion batteries where they have found moderate success, although they are often plagued by slow intercalation kinetics[12,13]. However, none of these candidate

materials have taken over research efforts, so developing an understanding of aqueous intercalation conditions could lead to the production of next generation electrode materials.

While they may seem dissimilar, inspiration for how to improve mass transport in electrodes can actually be taken from filtration membranes. In filtration membranes composed of 2D materials, it is found that increasing the interlaying spacing can greatly increase mass transport. These studies found that ordered films of bulk 2D materials are impermeable to many liquids and gases[14,15]. The basal planes of the 2D materials can form leak proof seals[14], but interestingly, even the interlayer is also impermeable as the d-spacing is not wide enough to accommodate a guest species. Even weakly interacting gases with a small kinetic radius, such as helium, are unable to pass through the interlayer space. However, in 2D materials that have been surface functionalized such as graphene oxide, it is found that ordered films composed of these materials are permeable to most liquids and gases[16,17]. These studies note that the functionalized materials have increased interlayer spacing and that this is the critical factor in determining if the 2D material is permeable. This fact has been leveraged to generate films where the permeability can be turned on or off by controlling the interlayer separation. Additionally, there are studies that suggest electrochemical intercalation is enhanced in interlayer expanded 2D material films. In a recent publication, metallic MoS_2 with an expanded interlayer was intercalated with zinc ions in an aqueous environment at relatively low (<1.3 V) potentials where bulk MoS_2 could not be intercalated[18]. This study suggests that expanded interlayer materials might be more electrochemically active, although they offer no explanation as to why the interlayer spacing is increased in their material. I suspect it is a result of their hydrothermal synthesis method, where the resulting 1T MoS_2 is surface functionalized and the functional groups separate the interlayer to ~10 Å.

These studies suggest that our molecule-2D material superlattice structure could be an interesting candidate material for developing devices with fast mass transport. Typically in bulk 2D materials, the largest energy barrier to insert a molecule or ion is the separation of the 2D material layers. When layered materials intercalate, they do so in stages, where ions progressively insert until the upper limits of intercalation are reached[19]. In the case of our superlattice system, the material already matches the structure of a stage 1, or fully intercalated, material where layers of 2D materials alternate with layers of the guest species. Because the interlayer is already expanded, the largest energy barrier of separating the 2D layers has already been overcome, so the intercalation of a different species will only need to overcome the much smaller barrier of switching one intercalant for another. Our material also has the distinct advantage of a mobile species in the interlayer, where typically the interlayer expansion is due to a bridging ion or surface functional groups.

5.2 Electrochemical intercalation of the superlattice

To begin testing the dynamic potential of our superlattice material, we began by qualitatively checking the permeability of membranes made of bulk and expanded interlayer materials. We assembled films on filter paper by vacuum filtration, and we used these films to seal an aluminum vial containing a liquid. In these experiments, we looked at mass loss over time of vials sealed with both bulk MoS_2 films and molecule containing MoS_2 films. We found that water evaporates from an open container held at 30°C at a rate of ~50 mg/hour, through restacked MoS_2 films at a rate of ~5 mg/hour, and through oleic acid containing films at a rate of ~12 mg/hour. We chose to use oleic acid to expand the interlayer as it has a low vapor pressure and will not evaporate out of the film, although there are many choices for molecules that could be

inserted. The fact that the open container lost much more mass than either of the films suggests that our material is not the most conductive to molecules. However, the oleic acid containing film losing at mass at slightly more than twice the rate of the restacked film suggests that expanding the interlayer does, at least qualitatively, improve the dynamic properties of the material. Because these results are so qualitative, it's difficult to draw any solid conclusions from the data, although it does suggest that our molecule expanded films might have similar dynamic properties to other interlayer expanded materials.

To more rigorously test if expanding the interlayer changes the properties of the material, we wanted to electrochemically intercalate ions into our films. Similar to the works that intercalated zinc into interlayer expanded MoS_2, we began by generating interlayer expanded films of MoS_2 containing NMP. These films were doctor bladed onto aluminum foil to make our working and counter electrodes, and used in a Teflon electrochemical cell. We chose to look at a variety of electrolytes, but began with studying the SO_4^{2-} anion as sulfuric acid is used in commercial lead batteries, although typically in much harsher conditions (i.e. pH < 1). As a control experiment, we also doctor bladed electrodes of bulk MoS_2. All electrochemical measurements were taken on a 3 electrode setup in reference to 1.6M Ag/AgCl. First we determined the electrochemical stability window of our system, and we found that in 3M Na_2SO_4, the system is relatively stable between -0.2 and 1.5 V. Outside of this window, hydrogen or oxygen evolution respectively causes electrode delamination. These values are quite similar to the literature values for the onset of water splitting, and held for all the aqueous electrolytes used in these experiments.

After determining the electrochemical stability window of our system, we performed oxidative linear sweep voltammetry (LSV) to attempt the intercalation of SO_4^{2-} ions into the superlattice (Figure 1). For the bulk material, we found that these linear sweeps had no features

before the onset of water splitting, whereas for the superlattice material, we found two features. For the bulk material, the first feature was the onset of oxygen evolution which begins around 1.1 V and is marked by an increase in the current as a function of the potential. However, the superlattice system had two additional features before the onset of oxygen evolution, which occur at 0.9 V and 1.2 V. Based on previous work with the intercalation of graphene, these peaks occur roughly in same place as intercalation peaks for graphitic materials, suggesting that in this system they could also be intercalation features. The lack of these features in electrodes made from the bulk material suggests that neither process is a surface event, such as electrode corrosion or ion

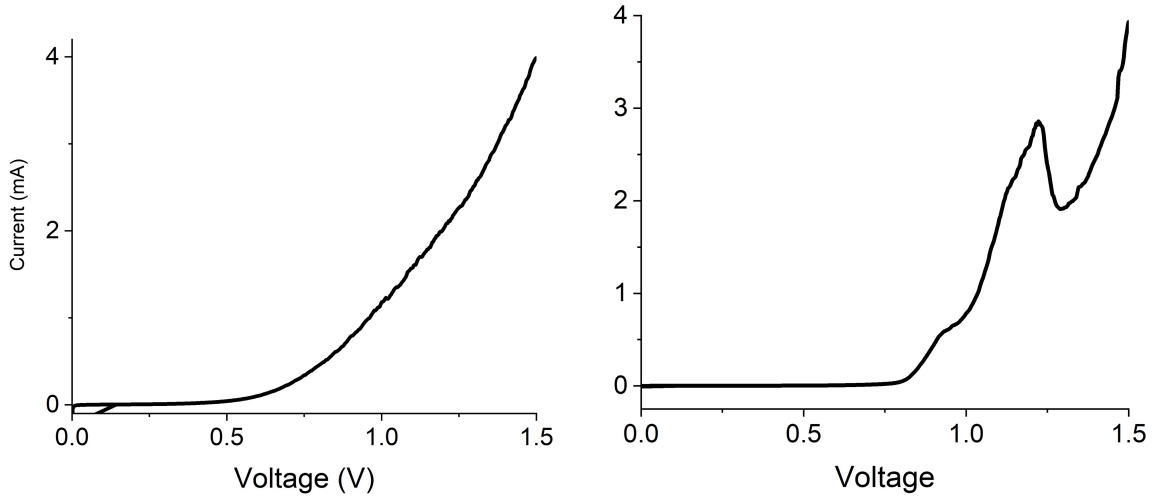


Figure 1: LSV of bulk (left) and superlattice (right) material in 3M $NaHSO_4$. Current increases as a function of potential in the bulk system due to the oxidation of water. The superlattice system has two additional features at 0.9 and 1.2 V.

adsorption. Our working hypothesis for the presence of these peaks is intercalation that can only occur in the expanded interlayer material due to the much weaker interlayer interactions between the molecular phase and 2D material.

To test this hypothesis, we next checked the ability of the superlattice system to intercalate other anions such as PO_4^{3-}. Typically, when graphite electrodes are cycled in sulfate and phosphate buffers, it has been shown that sulfate intercalates whereas phosphate does not[20]. However, in our

system, the interlayer is already greatly expanded so the energy to intercalate all ionic species should be significantly lower and allow us to potentially intercalate phosphate despite the inability to do so in previous systems. Indeed, when we perform linear sweeps in a 3M phosphate buffer we find that the features are qualitatively similar to the sulfate system (Figure 2), although the ratio of current density between the first and second features is different.

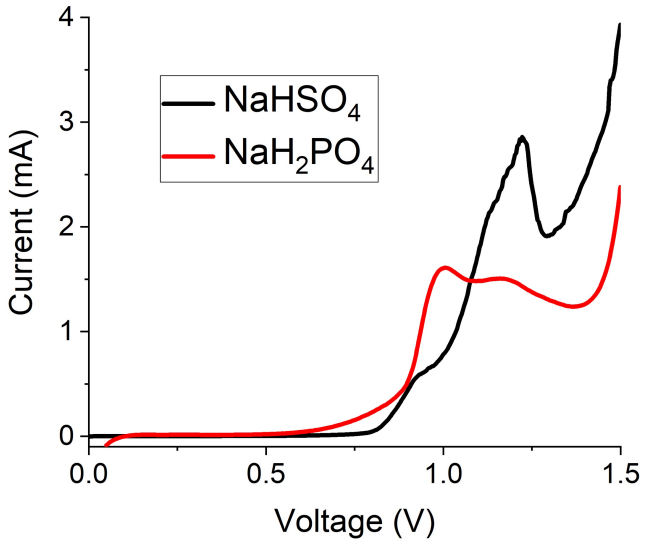


Figure 2: Voltammograms of superlattice electrodes in 3M $NaHSO_4$ (black) and NaH_2PO_4 (red). Qualitatively, both the phosphate and sulfate system have peaks at similar potentials, although the ratios between the peaks are quite different.

To more deeply understand the chemical nature of these features, we next performed chronopotentiometry (CP) (Figure 3). In a CP experiment, the change in voltage is measured as a constant current, in our system 0.100 mA, is applied to the system. The CP of the superlattice system showed 3 voltage plateaus at 0.60, 0.91, and 1.18. The first plateau at 0.6 V corresponds to oxygen adsorption to the electrode, and the third plateau at 1.4 V corresponds to water oxidation. Looking at the feature at 0.91 V, the potential increases during the process suggesting that is some sort of non-steady state process occurring, such as oxidation coupled with a rearrangement in the electrode. Interestingly, this feature has a much greater current density in the phosphate system, suggesting that a greater rearrangement is necessary in order to begin the intercalation of phosphate anions. Unlike the first feature, the second feature at 1.2 V is shown by the CP to be a steady state process such as intercalation. Taken with the fact that the first feature is a non-steady state process,

we suggest that the intercalation of the ions into the superlattice is a two-step process, where first the oxidation of the superlattice causes a rearrangement of the structure, and second, the ions intercalate into the rearranged structure. From the CP, we can also calculate a capacity for each of the processes using the equation:

$$\text{Capacity} = I * t / \text{mass of } MoS_2$$

Using that equation, we find that the capacity of the first plateau is 70 mAh/g, and the capacity of the second plateau is 158 mAh/g. This second capacity is fairly similar to the high end of reported gravimetric capacities for the intercalation of zinc ions (~232 mAh/g for zinc) into MoS_2[21]. If both of these events are part of a 2 step intercalation process, then the total capacity of the system would be 228 mAh/g, which is quite similar to the gravimetric capacity for zinc intercalation.

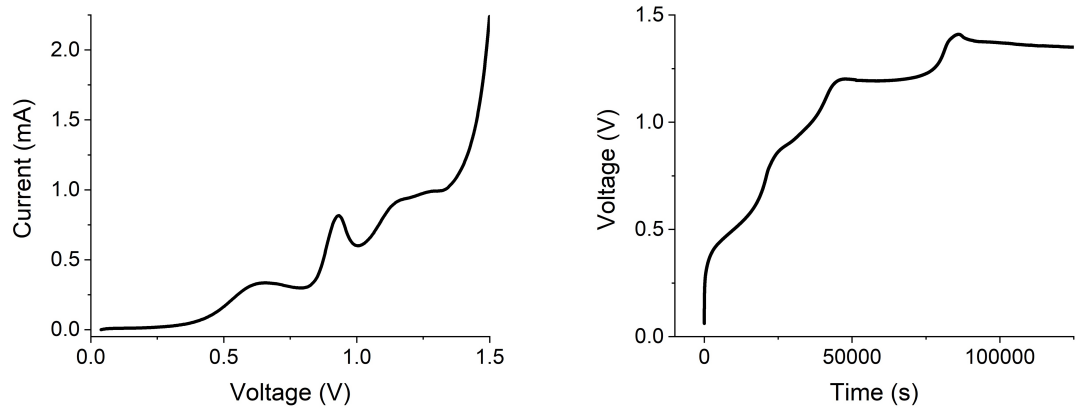


Figure 3: LSV (left) and chronopotentiometry (right) of the superlattice material in 1M $Na(NH_4)_2PO4$. The linear sweep shows three peaks at voltages 0.65, 0.93, and 1.22. The chronopotentiometry shows three corresponding features at 0.60, 0.91, and 1.18. The final plateau corresponds to water oxidation.

In order to check that the anion was present in the material after cycling, we performed XPS on the sample after charging (Appendix 3). We found that superlattice samples that had been charged in the sulfate electrolyte contained an additional sulfur peak that corresponds to an oxidized sulfur group, and samples charged in a phosphate electrolyte contained phosphorous. The

presence of these peaks in superlattice films and the absence in bulk films suggests that there is incorporation of the anions into the superlattice. Because the anions are divalent, there is also a chance that cations will cointercalate with the anions in order to preserve charge neutrality. To test this hypothesis, we varied the cation of the phosphate electrolyte and found that this changed the position of the first feature by between 50 to 100 mV, which suggests that only the first feature is dependent on the chemistry of the cation (Figure 4). Taken with the CP which suggests that the first feature is a non-steady state process and the second feature is a steady state process, we can propose a mechanism where the initial rearrangement (first feature) is driven by the cointercalation of the cation and anion. Then, as the rearrangement proceeds, intercalation of additional anions can occur (second feature) which is much less impacted by the chemistry of the cation.

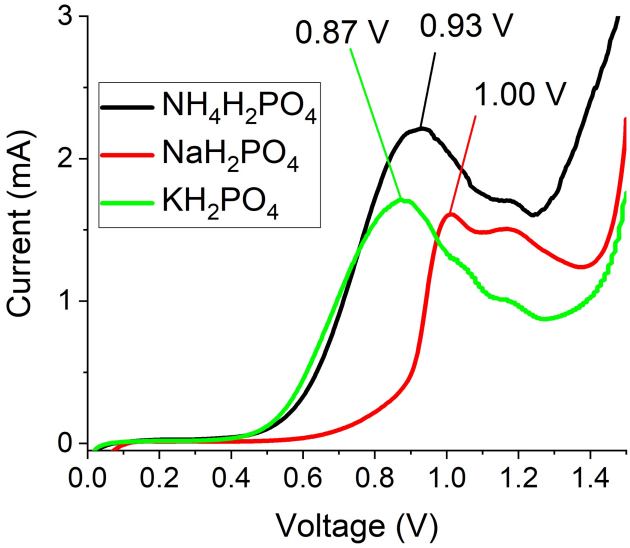


Figure 4: Overlaid voltammograms of 3 phosphate systems. The first feature changes potential based on the cation attached to the PO_4 group, while the second feature does not move from 1.18 V.

Because intercalation reactions are typically reversible, we next performed cyclic voltammetry of the system between .25 and 1.4 V to look for deintercalation processes (Figure 5). Interestingly, the CV showed that neither process was reversible at a variety of sweep rates. Because changing the sweep rate does not change the reversibility of the voltammogram, this suggests to us that the nature of the irreversibility stems from an irreversible change to the superlattice structure as a direct result of the intercalation process. Most likely, this change is due

to the non-steady state process observed at 0.9 V. If that process is indeed a rearrangement of the structure of the electrode which makes subsequent intercalation possible, then it may be impossible to deintercalate the material over this voltage range.

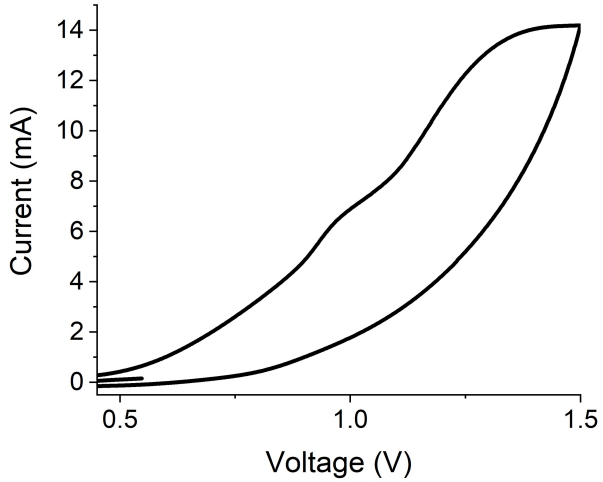


Figure 5: Cyclic voltammogram of the superlattice material in 1M NaH_2PO_4 at a scan rate of 10 mV/s. The lack of peaks on the reductive sweep suggests that the processes observed in the oxidative sweep are irreversible.

We also conducted a final set of experiments to look at the effects of pH on the two intercalation features. By adding either NaOH or H_3PO_4 to the electrolyte, we used NaH_2PO_4 to buffer the electrolyte at high (8) and low (2) pH. These pH values were chosen as they correspond to the first and second pKa values for phosphoric acid. We found that in basic solutions, there was no intercalation of the system. This makes sense as divalent ions are typically much more difficult to intercalate than monovalent ions, such as Zn^{2+} compared to Li^{+}. Conversely, we found that in acidic solutions, the two electrochemical peaks shifted slightly relative to the neutral pH system, but were still both present. In the neutral

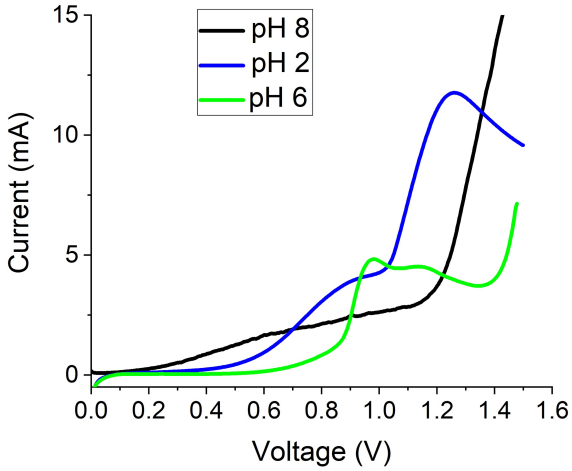


Figure 6: Voltammograms across various pHs for electrodes cycled in a phosphate electrolyte. At pH 10, there are no intercalation peaks. Relative to the pH 6 system, the pH 2 system features are shifted slightly.

system, the peaks appear at 0.95 and 1.15 V, whereas in the acidic system they appear at 0.85 and 1.26 V. This change in potential suggests that both steps of the intercalation mechanism are impacted by the pH of the electrolyte.

Conclusions and Outlook

By exploiting the uniquely weak interactions of the molecular phase in out 2D material-molecule superlattices, we realize intercalation of a variety of cations and anions under mild, aqueous conditions. We first explored the intercalation of a sulfate ion system via LSV and found that intercalation was not possible into bulk MoS_2 at neutral pH before the onset of water splitting. However, when we performed LSV on the superlattice system, we observe the appearance of two additional features before water splitting. In this system, the first feature at 0.9 V had a much lower current density than the second feature at 1.2 V. To further explore the capabilities of this system to intercalate ions, we next examined the phosphate ion system which typically does not intercalate under the same conditions as sulfate. Interestingly, upon performing a linear sweep of a superlattice system in a phosphate electrolyte, we found that there were two features in similar positions to those in the phosphate system.

To explore the types of processes responsible for these electrochemical features, we next performed CP on the phosphate ion system. Due to the long time scale of the CP experiments, we were unable to keep the electrolyte air free, so we also observe oxygen adsorption to the electrode at 0.6 V. We observe that for the first feature after the oxygen adsorption, the potential increases over time, indicating that it is not a steady state process. We attribute this to a structural change in the lattice which is necessary before the second electrochemical process can begin. For this second process, the CP reveals that this feature is a steady state process, which we believe to be

the intercalation of the anions into the lattice. We also find that varying the cation changes only the position of the non-steady state feature by ~100 mV, which shows that this first step is the only one involving intercalation of the ion. Cyclic voltammetry reveals that neither step of the intercalation process is reversible, further supporting the idea that the electrode is irreversibly rearranging in some way. Additionally, we show that the intercalation is pH dependent and can only occur in acidic and neutral systems, suggesting that only monovalent ions can intercalate at low potentials.

By showing intercalation into our expanded interlayer system, this work shows the increased dynamic potential of the superlattice material over bulk systems. While this work is a first step in generating devices from our material, understanding the exact mechanisms and structures that occur upon intercalation will be necessary in developing devices that can reversibly intercalate ions. Additionally, because we are able to activate previously electrochemically inert systems by interlayer expansion, many new types of materials can be explored by utilizing this strategy, which can lead to the development of new and exciting devices.

REFERENCES

(1) Griffith, K. J.; Wiaderek, K. M.; Cibin, G.; Marbella, L. E.; Grey, C. P. Niobium Tungsten Oxides for High-Rate Lithium-Ion Energy Storage. *Nature* **2018**, *559* (7715), 556–563. DOI: 10.1038/s41586-018-0347-0.

(2) Liang, Y.; Yao, Y. Designing Modern Aqueous Batteries. *Nat. Rev. Mater.* **2022**. DOI: 10.1038/s41578-022-00511-3.

(3) Ahn, H.; Kim, D.; Lee, M.; Nam, K. W. Challenges and Possibilities for Aqueous Battery Systems. *Commun. Mater.* **2023**, *4* (1), 37. DOI: 10.1038/s43246-023-00367-2.

(4) Li, W.; Dahn, J. R.; Wainwright, D. S. Rechargeable Lithium Batteries with Aqueous Electrolytes. *Science* **1994**, *264* (5162), 1115–1118. DOI: 10.1126/science.264.5162.1115.

(5) Tron, A.; Jeong, S.; Park, Y. D.; Mun, J. Aqueous Lithium-Ion Battery of Nano-$LiFePO_4$ with Antifreezing Agent of Ethyleneglycol for Low-Temperature Operation. *ACS Sustain. Chem. Eng.* **2019**, *7* (17), 14531–14538. DOI: 10.1021/acssuschemeng.9b02042.

(6) Liu, J.; Yang, C.; Chi, X.; Wen, B.; Wang, W.; Liu, Y. Water/Sulfolane Hybrid Electrolyte Achieves Ultralow-temperature Operation for High-voltage Aqueous Lithium-ion Batteries. *Adv. Funct. Mater.* **2022**, *32* (1). DOI: 10.1002/adfm.202106811.

(7) Shioyama, H.; Fujii, R. Electrochemical Reactions of Stage 1 Sulfuric Acid—Graphite Intercalation Compound. *Carbon N Y* **1987**, *25* (6), 771–774. DOI: 10.1016/0008-6223(87)90149-7.

(8) Beck, F.; Krohn, H.; Kaiser, W. Galvanostatic Cycling of Graphite Intercalation Electrodes with Anions in Aqueous Acids. *J. Appl. Electrochem.* **1982**, *12* (5), 505–515. DOI: 10.1007/BF00614976.

(9) Scharff, P.; Xu, Z. Y.; Stumpp, E.; Barteczko, K. Reversibility of the Intercalation of Nitric Acid into Graphite. *Carbon N Y* **1991**, *29* (1), 31–37. DOI: 10.1016/0008-6223(91)90091-V.

(10) Alcorn, F. M.; Kuntz, K. L.; Druffel, D. L.; Warren, S. C. Aqueous Intercalation of Graphite at a Near-Neutral PH. *ACS Appl. Energy Mater.* **2018**, *1* (9), 5062–5067. DOI: 10.1021/acsaem.8b01101.

(11) Ramanujapuram, A.; Gordon, D.; Nitta, N.; Magasinski, A.; Ward, B.; Huang, C.; Yushin, G. Degradation and Stabilization of Lithium Cobalt Oxide in Aqueous Electrolytes. *Meet. Abstr.* **2016**, *MA2016-02* (1), 136–136. DOI: 10.1149/MA2016-02/1/136.

(12) Alfaruqi, M. H.; Gim, J.; Kim, S.; Song, J.; Pham, D. T.; Jo, J.; Xiu, Z.; Mathew, V.; Kim, J. A Layered δ-MnO 2 Nanoflake Cathode with High Zinc-Storage Capacities for Eco-Friendly Battery Applications. *Electrochem. commun.* **2015**, *60*, 121–125. DOI: 10.1016/j.elecom.2015.08.019.

(13) Kundu, D.; Adams, B. D.; Duffort, V.; Vajargah, S. H.; Nazar, L. F. A High-Capacity and Long-Life Aqueous Rechargeable Zinc Battery Using a Metal Oxide Intercalation Cathode. *Nat. Energy* **2016**, *1*, 16119. DOI: 10.1038/nenergy.2016.119.

(14) Nair, R. R.; Wu, H. A.; Jayaram, P. N.; Grigorieva, I. V.; Geim, A. K. Unimpeded Permeation of Water through Helium-Leak-Tight Graphene-Based Membranes. *Science* **2012**, *335* (6067), 442–444. DOI: 10.1126/science.1211694.

(15) Su, Y.; Kravets, V. G.; Wong, S. L.; Waters, J.; Geim, A. K.; Nair, R. R. Impermeable Barrier Films and Protective Coatings Based on Reduced Graphene Oxide. *Nat. Commun.* **2014**, *5*, 4843. DOI: 10.1038/ncomms5843.

(16) Hu, M.; Mi, B. Enabling Graphene Oxide Nanosheets as Water Separation Membranes. *Environ. Sci. Technol.* **2013**, *47* (8), 3715–3723. DOI: 10.1021/es400571g.

(17) Ali, A.; Rehman, F.; Ali Khan, M.; Memon, F. H.; Soomro, F.; Iqbal, M.; Yang, J.; Thebo, K. H. Functionalized Graphene Oxide-Based Lamellar Membranes with Tunable Nanochannels for Ionic and Molecular Separation. *ACS Omega* **2022**, *7* (36), 32410–32417. DOI: 10.1021/acsomega.2c03907.

(18) Cai, C.; Tao, Z.; Zhu, Y.; Tan, Y.; Wang, A.; Zhou, H.; Yang, Y. A Nano Interlayer Spacing and Rich Defect 1T-MoS2 as Cathode for Superior Performance Aqueous Zinc-Ion Batteries. *Nanoscale Adv.* **2021**, *3* (13), 3780–3787. DOI: 10.1039/d1na00166c.

(19) Stark, M. S.; Kuntz, K. L.; Martens, S. J.; Warren, S. C. Intercalation of Layered Materials from Bulk to 2D. *Adv. Mater.* **2019**, *31* (27), e1808213. DOI: 10.1002/adma.201808213.

(20) Boruah, B. D.; Wen, B.; De Volder, M. Molybdenum Disulfide-Zinc Oxide Photocathodes for Photo-Rechargeable Zinc-Ion Batteries. *ACS Nano* **2021**. DOI: 10.1021/acsnano.1c06372.

(21) Alsmeyer, D. C.; McCreery, R. L. In Situ Raman Monitoring of Electrochemical Graphite Intercalation and Lattice Damage in Mild Aqueous Acids. *Anal. Chem.* **1992**, *64* (14), 1528–1533. DOI: 10.1021/ac00038a006.

APPENDIX 1: SUPPORTING INFORMATION FOR CHAPTER 2

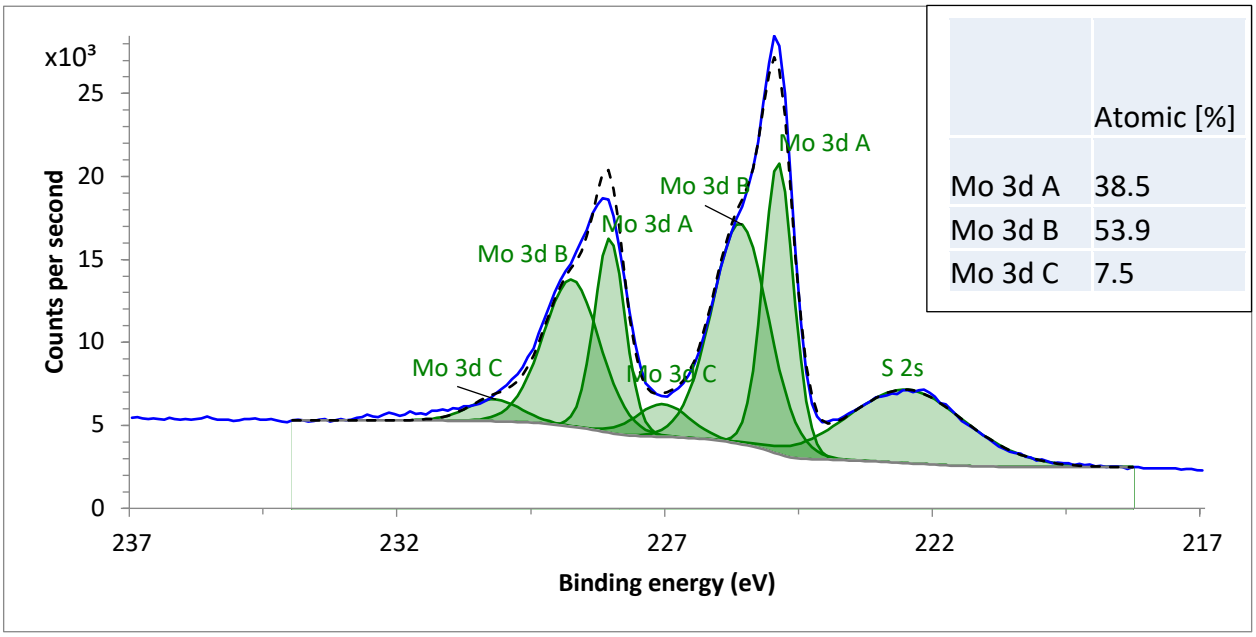


Fig A1-1: XPS analysis of a thin film constructed from unannealed monolayers. Mo 3d A corresponds to the 1T phase, Mo 3d B corresponds to the 2H phase, and Mo 3d C corresponds to MoO_3. We observe that ~40% of the material is metallic after the exfoliation, in good agreement with literature values.

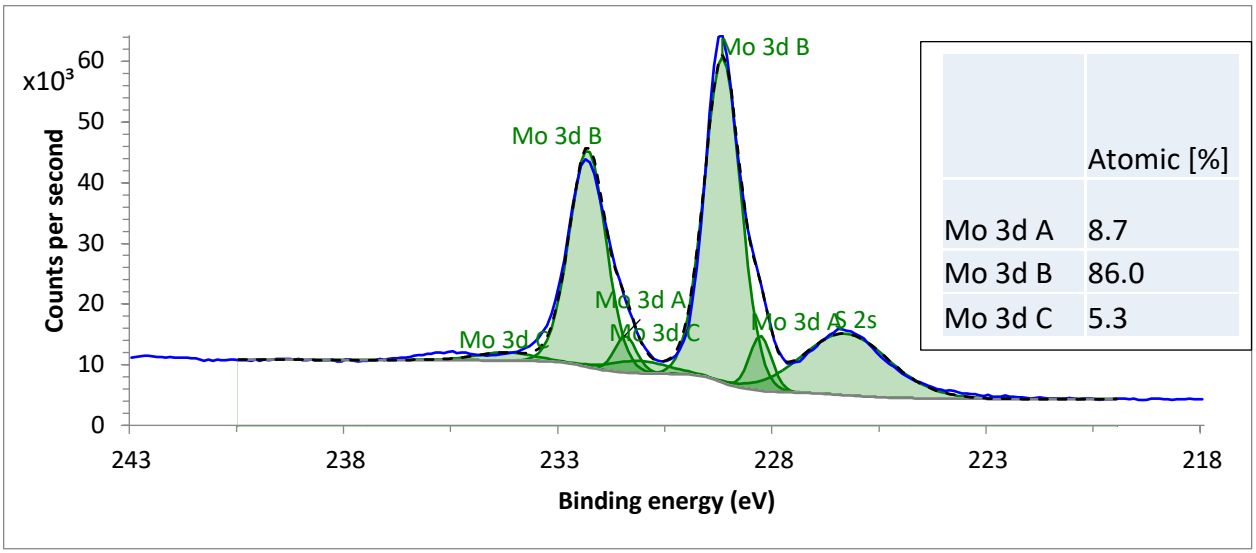


Fig A1-2: XPS analysis of a thin film constructed from annealed monolayers. Mo 3d A corresponds to the 1T phase, Mo 3d B corresponds to the 2H phase, and Mo 3d C corresponds to MoO_3. After annealing we observe ~86% of the material is the semiconducting phase.

APPENDIX 2: SUPPORTING INFORMATION FOR CHAPTER 4

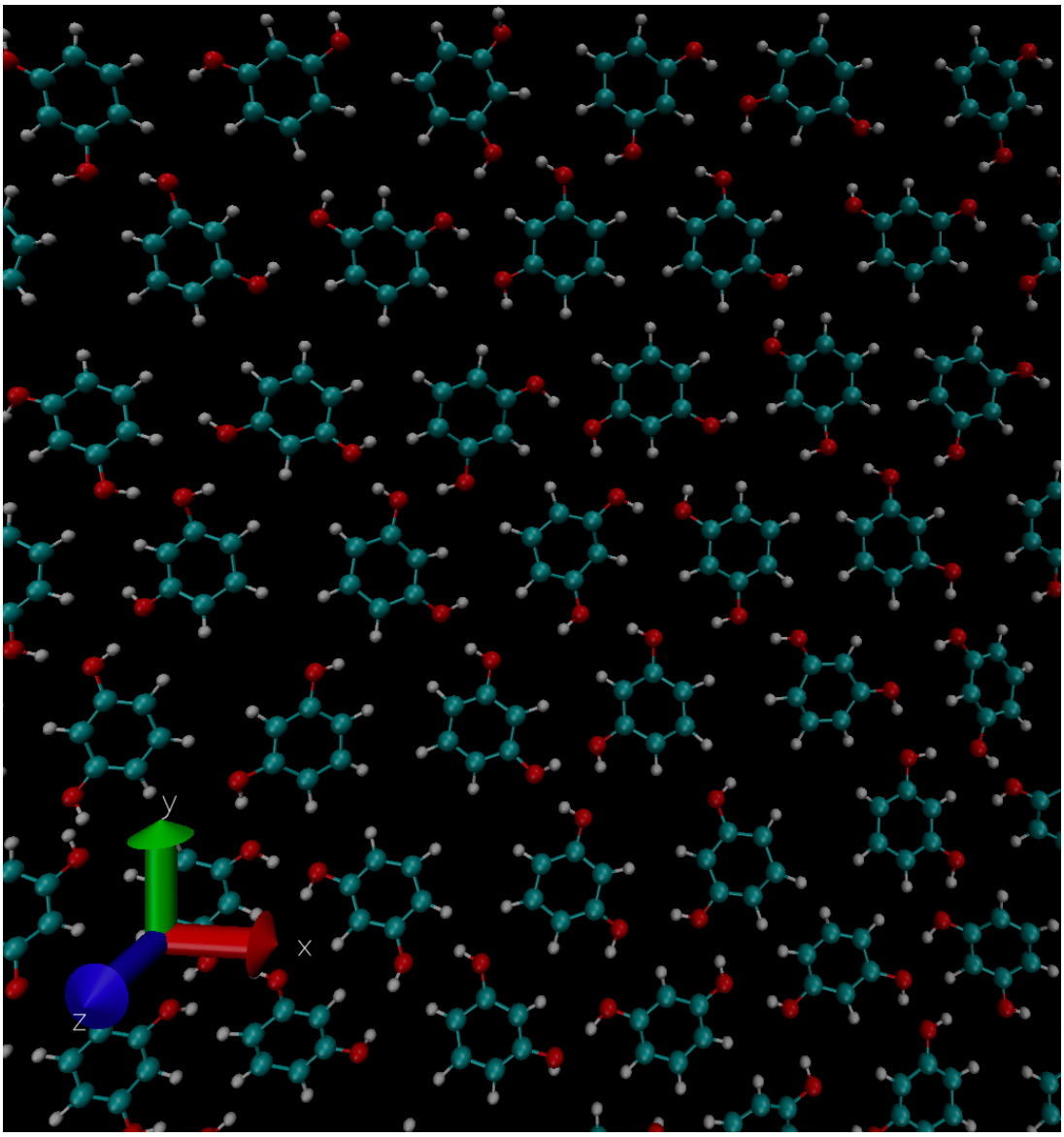
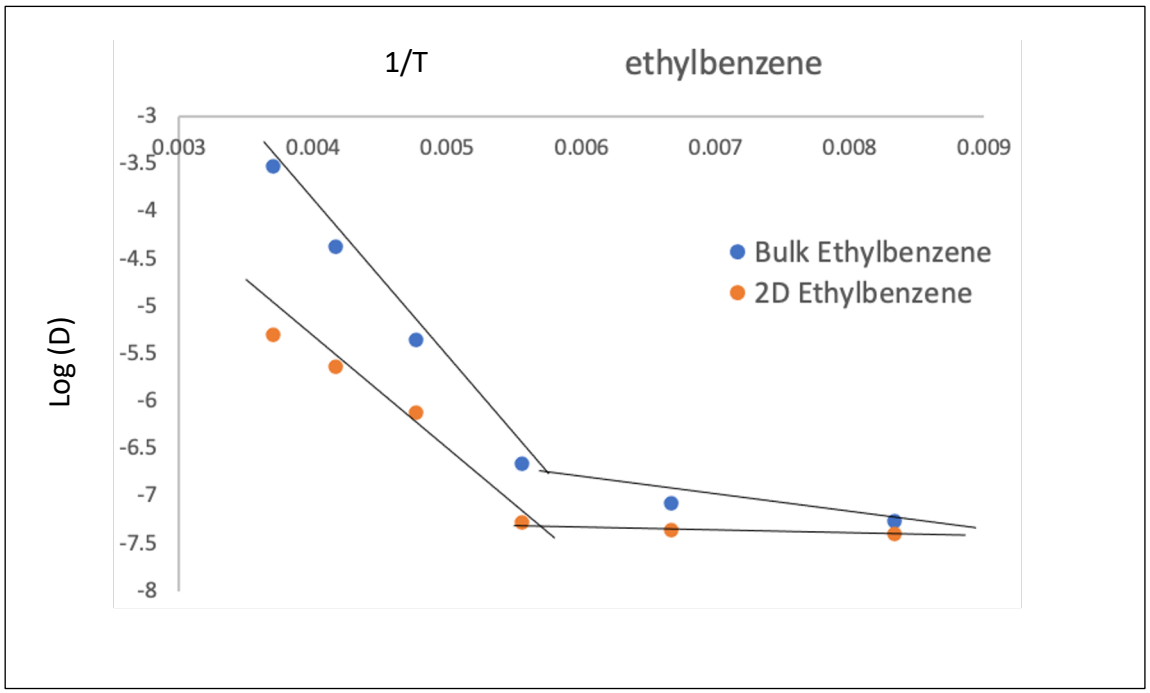
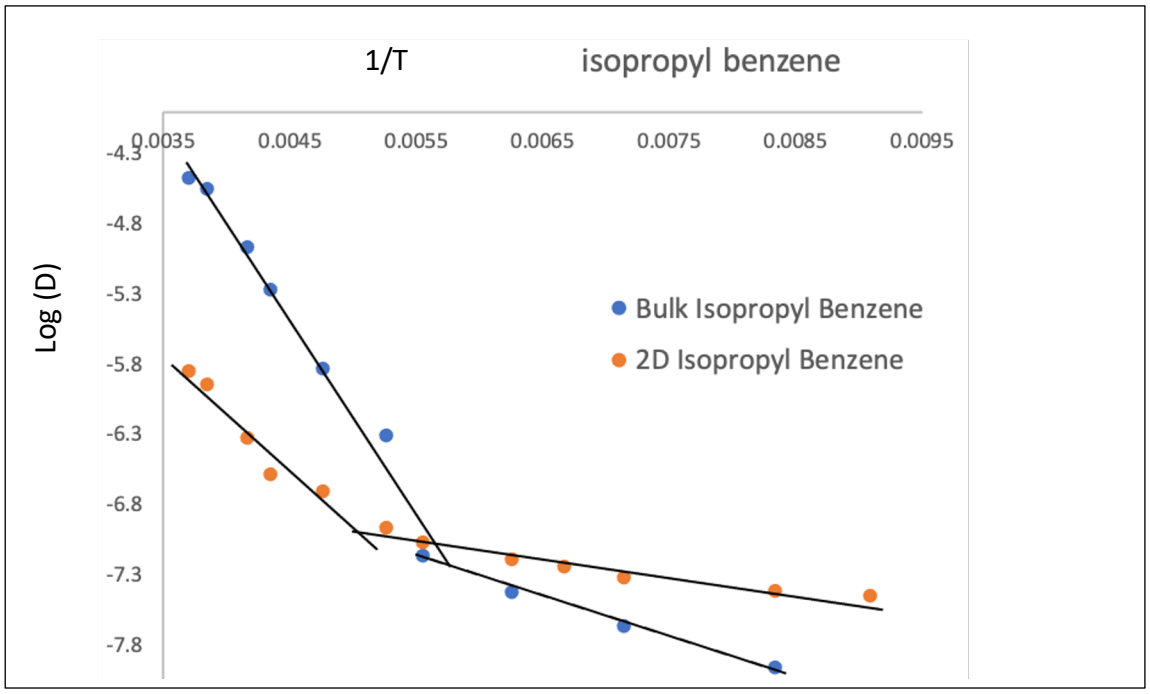


Fig A2-1: Representative screenshot of the confined resorcinol layer in a rescorcinol-MoS_2 superlattice. The MoS_2 has been removed for clarity. In the screenshot, the ability of the -OH groups to hydrogen bond is clearly shown. Additionally, each resorcinol molecule has 6 nearest neighbors indicative of a hexatic liquid phase.





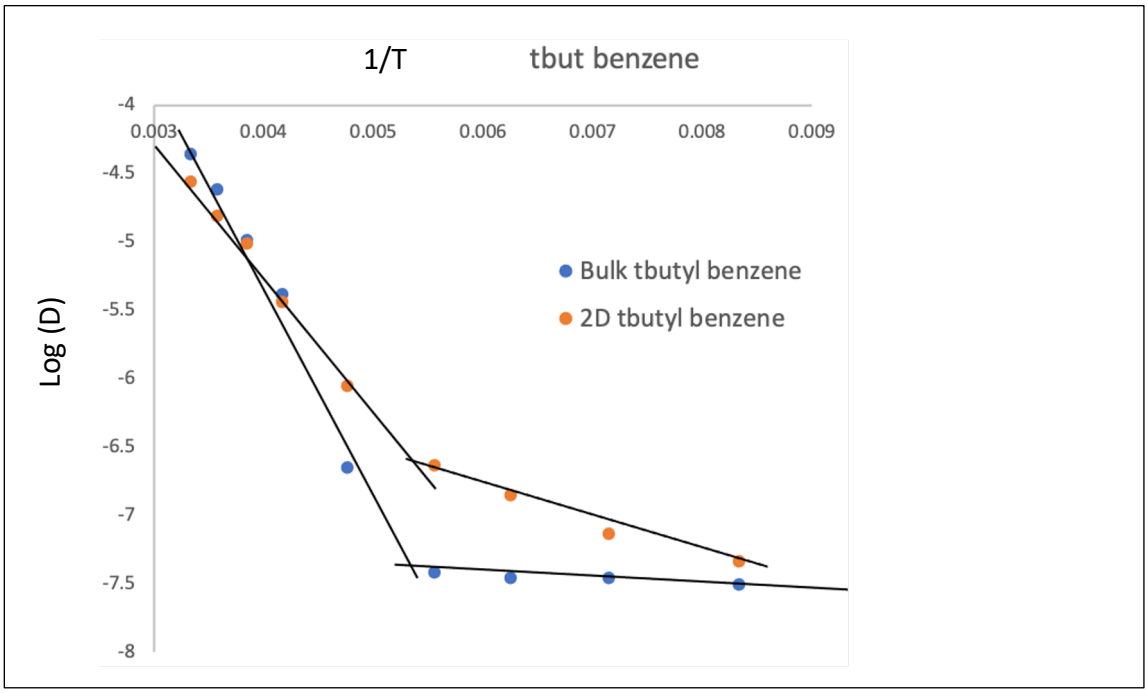


Fig A2-2: Bulk and confined diffusion plots for benzene with an alkyl -R group. As the R group is changed from an ethyl (top), isopropyl (middle) or t-butyl chain (bottom), the confined diffusion begins to become faster relative to the bulk diffusion.

APPENDIX 3: SUPPORTING INFORMATION FOR CHAPTER 5

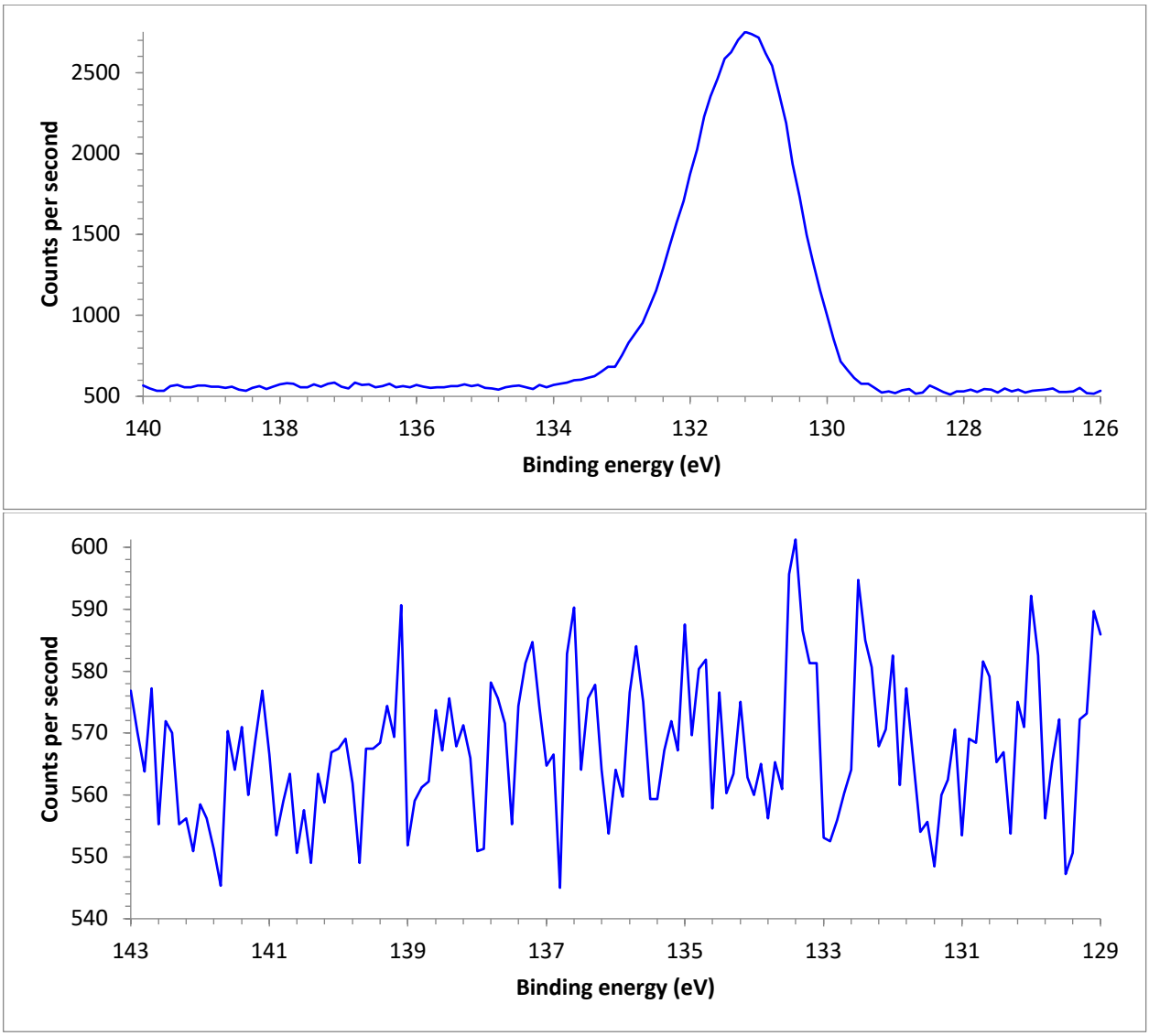


Fig A3-1: Phosphorus 2p XPS spectra for superlattice charged in 3M $NH_4H_2PO_4$ (top) and as prepared material (bottom). The clear growth of a phosphorus peak indicates the superlattice is uptaking phosphorous during the charging process.

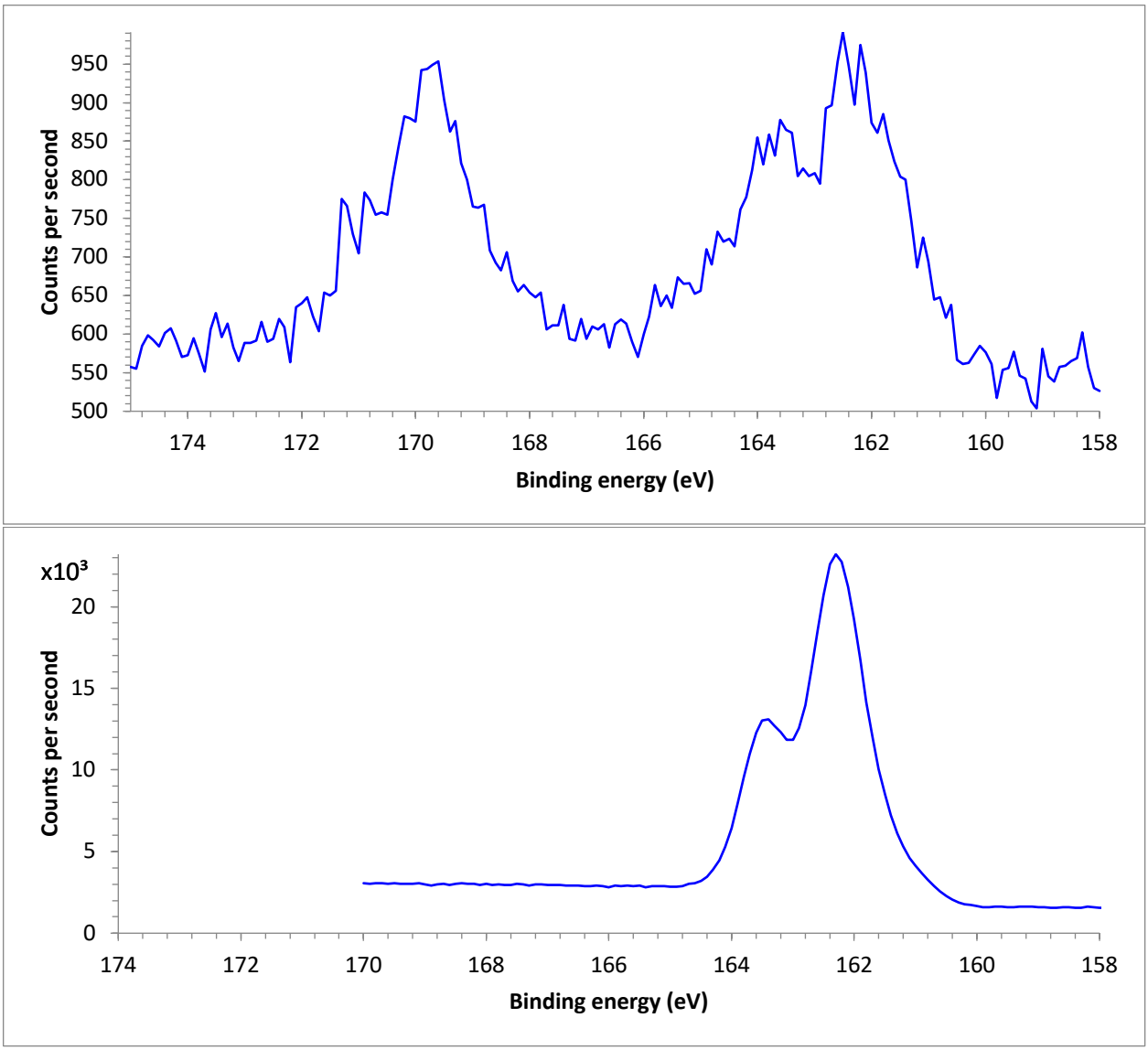


Fig A3-2: Sulfur 2p XPS spectra for superlattice charged in 3M NH_4HSO_4 (top) and as prepared material (bottom). The two peaks at 162 and 164 are Mo bound S, whereas the peak in the top spectrum at 170 is indicative of O bound S such as from a sulfate.